CHARACTERIZATION OF ANISOTROPIC GUIDED WAVE PROPAGATION AND SCATTERING FOR ROBUST IN SITU ULTRASONIC IMAGING OF DAMAGE

A Dissertation
Presented to
The Academic Faculty

by

Westin Bruce Williams

In Partial Fulfillment
of the Requirements for the Degree
Doctor of Philosophy in the
School of Electrical and Computer Engineering

Georgia Institute of Technology
May 2019

CHARACTERIZATION OF ANISOTROPIC GUIDED WAVE PROPAGATION AND SCATTERING FOR ROBUST IN SITU ULTRASONIC IMAGING OF DAMAGE

Approved by:

Dr. Jennifer E. Michaels, Advisor
School of Electrical and Computer Engineering
Georgia Institute of Technology

Dr. Bonnie H. Ferri
School of Electrical and Computer Engineering
Georgia Institute of Technology

Dr. Thomas E. Michaels, Co-Advisor
School of Electrical and Computer Engineering
Georgia Institute of Technology

Dr. Waymond R. Scott
School of Electrical and Computer Engineering
Georgia Institute of Technology

Dr. Massimo Ruzzene
School of Aerospace Engineering
Georgia Institute of Technology

Dr. Ying Zhang
School of Electrical and Computer
Georgia Institute of Technology

Date Approved: December 6, 2018

To my family,

Wayne, Dena, and Devan,

without whom this thesis would have never been written.

ACKNOWLEDGEMENTS

I would first like to dedicate this thesis to the late Dr. Thomas E. Michaels. His guidance and ability to bestow knowledge on me was truly inspirational and his charismatic spirit will never be forgotten. He took a chance on me in an academic field I was unfamiliar with, and for that, I will always be grateful.

Secondly, this thesis would have never come to fruition if it wasn't for the continued support and effort from my advisor, Dr. Jennifer E. Michaels. I cannot put into words the gratitude I have for the work and time she spent with me in helping me achieve my single greatest accomplishment of my academic career.

Thirdly, I would like to thank each one of my committee members, Dr. Ying Zhang, Dr. Waymond Scott, Dr. Bonni Ferri, and Dr. Massimo Ruzzene for their time and efforts.

A thank you to all my colleagues, Dr. Xin Chen, Dr. Alexander Dawson, Dr. Yu Weng, Joe Kummer, and Carson Maki. Every one of our discussions whether technical or personal made my time at the QUEST lab a much more enjoyable experience. To Dr. Yu Weng, your friendship has made me a better person for opening my eyes to different parts of life and challenging my own personal creativity, thank you.

I cannot thank all these people who have contributed to my life without recognizing the ones who have contributed to it the most. To my parents, Wayne Williams and Dena Williams, as well as my brother, Devan Williams, thank you for loving me and supporting me in life no matter what it was. I would not be here, writing this, if it wasn't for you. I

also owe a thank you to all my other family and friends, especially the Reis family who have touched my life in unforgettable ways.

Lastly but not least, I want to thank my beautiful girlfriend, Kelly Stewart, for loving me and putting up with all the late nights it took to make this thesis a reality.

The presented research was sponsored by the National Aeronautics and Space Administration (NASA) under Grant No. NNX12AL13A to Georgia Tech, and by Advanced Systems & Technologies as part of a NASA SBIR Phase II Award. The program manager was Dr. Cara Leckey, whom I would also like to thank.

TABLE OF CONTENTS

LIST OF TABLES

LIST OF FIGURES

SUMMARY

The objective of this research is to improve the performance of *in situ* imaging techniques in anisotropic composite materials for structural health monitoring (SHM). Using guided ultrasonic waves with *in situ* spatially distributed arrays of point-like transducers, a large structure can be interrogated since such waves propagate with reduced spreading loss as compared to bulk waves. Being able to assess damage through an active SHM approach can reduce risk and extend the operational life of the structure. Common defects such as delaminations arise in composite aerospace structures from abrupt impacts that can be undetectable through visual inspection. Prior work has shown that these defects can be successfully detected and located using *in situ* imaging methods, but not as well as defects in isotropic metallic components. Presented here are methods to improve *in situ* imaging of damage in anisotropic materials that are based upon acquiring *a priori* knowledge of wave propagation and scattering characteristics.

This thesis has five major aspects. The first is experimental estimation of anisotropic velocity and attenuation via wavefield imaging. The second is using these estimates to extract scattering characteristics of artificial and impact damage by applying wavefield baseline subtraction combined with a circular scattering model. Third, a method for estimating a complete 2-D scattering matrix of a defect from a limited number of columns is developed. Fourth, a variety of damage types is characterized for two separate composite panel specimens with differing levels of material quality and anisotropy. And lastly, the scattering estimates are applied to *in situ* imaging of damage and the efficacy of this approach is evaluated by comparing imaging results to those obtained using other scattering assumptions. Overall, imaging performance improved after applying scattering estimates for the damage types examined but the incorporation of anisotropic group

velocities into the imaging method had minimal positive effects. The simplified geometry model that was developed was also utilized for imaging, and the results showed some improvement in the reduction of image noise.

The primary novelty of this work is the methodology developed to estimate 2-D scattering matrices for anisotropic composite panels. It is shown that incorporating these scattering estimates into MV imaging of damage improves performance by enhancing detection and reducing image noise. Additional work was also performed for characterizing anisotropic wave propagation using a Radon panel to evaluate signals in the time-domain. This allowed for characterization of a wave packet of interest instead of a single wave frequency and the results from this characterization process are utilized in estimating damage scattering in the same anisotropic composites. Application of these methodologies was demonstrated through experimental data acquired for both artificial and real impact damage.

INTRODUCTION

This chapter provides a brief description of non-destructive evaluation and structural health monitoring. These topics have been researched extensively as they pertain to isotropic media; however, there is still much to be understood about guided wave interactions in anisotropic composite media. Practical demand for quick and robust identification of damage in composites is motivating current research efforts. Lamb waves, a type of guided wave, are sensitive to damage over long distances and can be used for *in situ* imaging methods. Prior work for isotropic materials has shown that using *a priori* scattering information can improve imaging results. The research goals here are aimed at reliably quantifying scattering from damage in composites using wavefield imaging. By obtaining high resolution scattering information that be can be directly incorporated into sparse array imaging via a 2-D scattering matrix, it is hypothesized that improved detection and localization of damage can be achieved.

1.1 Background

Maintaining the integrity of a composite structure through routine damage inspection is critical for aerospace safety. Nondestructive evaluation (NDE) refers to such damage inspection methods that examine an object or structure without affecting its future usefulness or integrity [1]. Most inspections are schedule-based but a more logical approach is to monitor a structure and inspect it after a change in its condition is detected. One effective method for condition-based monitoring is to use a form of *in situ* NDE known as structural health monitoring (SHM). SHM is used to make quicker assessments of a structure's health through data acquisition, processing, and interpretation [2]. While

various NDE techniques such as visual inspection, ultrasonics, eddy currents, radiography and others are currently applied to composites, ultrasonics is most widely used because of safety, cost, and effectiveness. Ultrasonic guided waves generated from *in situ* sparse arrays are desired for SHM because of their ability to traverse large distances and interact with various defects. The interaction with these waves typically in the form of scattering can be used to help locate damage along with possible damage characterization through wave mode changes and directionality of scattering. While sparse array imaging has had extensive development for isotropic media, typical imaging algorithms can be unreliable when applied to anisotropic materials. This is due to increased complexity of wave propagation in the material. The research reported in this thesis focuses on improving imaging of defects through characterization of guided wave propagation and defect scattering behavior within composites.

1.2 Motivation and Research Goals

Composite-based components are being used more today in aerospace structures than ever before. Because composites have high strength-to-weight ratios, they are ideal for high load bearing applications when weight needs to be minimized. However, they are susceptible to damage from abrupt impacts that can cause internal layer separations known as delaminations as well as fiber breakage and cracking. These defects are difficult to detect when little evidence of the damage is visible on the surface, which is a common problem. Such damage can weaken the structure's integrity and thus must be discovered before a catastrophic failure occurs.

In addition to regular visual inspections, composite structures are typically managed on a time-based schedule whereby the structure is removed from service and the components are inspected individually for damage or replaced regardless of condition to

meet an expected part life-cycle [3]. Because of the obvious drawback in cost and time, a potentially more advantageous approach is guided wave structural health monitoring using a sparse array of spatially distributed transducers. *In situ* transducers are attached to or embedded in the structure for autonomous monitoring, which helps detect damage promptly and allows components to be replaced only when needed [4].

Initially the network of *in situ* transducers is used to record "snapshots" or baselines of the structure, which is assumed to be in good health. These baselines can then be used for comparison of future states to help identify the existence of newly formed damage. However, composites have an anisotropic material structure that complicates wave propagation and adversely affects imaging techniques used for SHM. This drawback of composites has been a point of study as the aerospace industry progresses towards a "smarter" form of damage state detection.

1.3 Contributions

The focus of this work is the development of a robust methodology for experimentally characterizing scattering from measured wavefield data in anisotropic composite materials. The results of such work may be used to better understand Lamb wave interactions with artificial and impact damage, improve imaging results for SHM, and provide a means for validating model-based scattering characterization. The first contribution of this work is a method for estimating material wave propagation properties of wave packets from acquired wavefield data with no prior knowledge of material properties. The results are obtained using the Radon transform in the time domain and can be applied to further improve scatterer characterization.

The second contribution of this work provides a detailed process for experimentally estimating high resolution scattering patterns from various damage types in anisotropic

materials, namely composites. Filtering in the Fourier domain is applied to 3-D wavefield data to suppress noise and other obscuring waves. A geometric scattering model based upon specular reflection from the edges of damage is developed to obtain scattered wave arrival times, which are used in estimating scattering patterns.

The third contribution of this research is an estimation method for obtaining full scattering matrices from scattering patterns estimated from a small number of incident directions.

The fourth contribution of this thesis is applying the scattering estimation methodology to both artificial and real impact damage for two composite panels with different fiber layups.

The fifth contribution of this thesis examines imaging performance from sparse array data after incorporating the panel-specific wave propagation characterization and damage geometry specular reflection modeling along with estimated scattering matrices for a specific damage case.

1.4 Thesis Organization

The remainder of the thesis is organized as follows. Chapter 2 provides an overview of fundamentals for NDE and SHM that serve as a foundation for the thesis. The literature survey discusses Lamb wave propagation mechanics in anisotropic composite materials and prior research focused on damage localization and characterization methods based on wavefield, sparse array and ultrasonic measurements. The objective and scope of the research presented in this thesis is placed in the context of this previous work.

Chapter 3 introduces the methodology for experimentally estimating anisotropic wave propagation parameters using wavefield measurements. The methodology uses a modified

Radon panel to estimate both phase and group velocity as a function of propagation direction. A model for estimating wave amplitude attenuation without prior knowledge of material property information is also described. The estimation results are then used later in both scattering characterization and sparse array imaging.

Chapter 4 describes a complete methodology for characterizing scattering of guided waves from artificial and impact damage in a composite plate from various incident wave directions using experimentally acquired full wavefield data. The methodology consists of preprocessing full wavefield datasets through baseline subtraction using a global space-time alignment method, filtering the obtained residual wavefield in the Fourier domain to isolate scattering observed from the damage, and calculating scattering arrival times using a scattering model based on an assumed damage geometry to obtain scattered amplitudes. The final 2-D scattering matrix is obtained using a Fourier fitting model combined with an interpolation procedure to fully populate the matrix.

Chapter 5 describes the results of applying multiple ultrasonic inspection methods for characterizing impact damage in two composite panel specimens. Initial sizing of delaminations is performed via through-transmission inspection while additional characterization of damage geometry and depth is achieved using pulse-echo measurements. An in-depth analysis of the results is performed with an emphasis on material quality of the specimens and its effect on the induced delaminations.

Chapter 6 presents the integration of work performed in Chapters 3-5 into sparse array imaging for better damage detection and localization. Anisotropic group velocity along with geometrical scattering compensation is incorporated into the minimum variance

imaging algorithm while the results from using the estimated scattering matrices are compared to those obtained using other scattering assumptions.

Chapter 7 concludes this thesis and provides recommendations for future research directions.

2 LITERATURE REVIEW

The purpose of the literature review, presented here, is to discuss prior research related to guided Lamb wave SHM methods and how they can be utilized in conjunction with composite materials. Section 2.1 begins with a review of fundamentals of ultrasonic wave propagation in anisotropic media. Section 2.2 describes data acquisition techniques utilized throughout the presented work. Section 2.3 reviews scattering of Lamb waves from defects, and section 2.4 describes previous research on characterizing wave propagation in composite materials. Section 2.5 discusses SHM fundamentals along with practical applications for composite materials while Section 2.6 provides context for the research presented in this thesis along with the research objectives.

2.1 Ultrasonic Wave Fundamentals

Ultrasonic elastic waves in solid anisotropic media can be classified as two different wave types based on their propagation mechanics: bulk waves and guided waves. Both wave types are used in ultrasonic NDE to interact with damage in a part or structure to extract meaningful information about the condition of the structure. The fundamentals of these waves must be well-understood since they serve as the foundation of all ultrasonic NDE techniques.

2.1.1 Bulk Waves in Anisotropic Media

Bulk wave propagation exists in infinite anisotropic media or when the medium dimensions are large relative to the wavelength of the propagating wave. The governing

equation for wave motion in a homogenous, anisotropic plate in reference to a cartesian coordinate system is given by,

$$\rho \ddot{u}_k = \frac{\partial \sigma_{kl}}{\partial x_l}, \tag{1}$$

and the constitutive relation,

$$\sigma_{kl} = c_{klmn} \varepsilon_{mn}, \qquad k,l,m,n = 1,2,3, \tag{2}$$

where σ_{kl}, ε_{mn}, and u_k are the components of stress, strain, and displacement, respectively, ρ is material density and, c_{klmn} are the elastic constants. For indicial notation, a sum over repeated indices is implied, i.e.,

$$\sigma_{kl} = \sum_{m=1}^{3} \sum_{n=1}^{3} c_{klmn} \varepsilon_{mn} \,. \tag{3}$$

A solution to Equation (1) is a plane wave with no attenuation in the form,

$$u_k = A \alpha_k e^{j(k_l x_l - \omega t)} \,. \tag{4}$$

Here, A refers to the displacement amplitude, $j = \sqrt{-1}$, ω is the wave frequency and α_k is the particle displacement vector. The path of propagation is described by a three-dimensional vector known as the wavenumber,

$$\vec{k} = k_1 \hat{e}_1 + k_2 \hat{e}_2 + k_3 \hat{e}_3 \,, \tag{5}$$

where k_1, k_2, and k_3 represent the wavenumber for the x_1, x_2, and x_3 directions, respectively. The wavenumber is related to the wave frequency ω and phase velocity c_p through the magnitude of the wavenumber,

$$\left| \vec{k} \right| = \frac{\omega}{c_p} \,. \tag{6}$$

For isotropic media there are two mode types that comprise bulk waves: longitudinal and transverse waves. Longitudinal waves are defined by particle motion that is parallel to the wave propagation direction. Because of the particle motion relative to wave propagation direction, periodic compression and tension is produced and longitudinal waves are thus referred to as pressure waves. For transverse waves, particle motion is perpendicular to the wave propagation direction, producing an associated shear stress. For this reason, transverse waves are commonly referred to as shear waves. Each wave can be distinguished by the relation between the particle displacement vector $\hat{\alpha}$ and direction of propagation $\hat{k}$. For pure longitudinal waves,

$$\hat{\alpha} \cdot \hat{k} = 1, \tag{7}$$

and for transverse waves,

$$\hat{\alpha} \cdot \hat{k} = 0. \tag{8}$$

Bulk anisotropic media support pure longitudinal and shear waves along directions of symmetry. For off-axis propagation, the displacement vector is not purely transverse or longitudinal but is oblique to the direction of the propagation. These waves are often referred to as quasi-longitudinal when,

$$\hat{\alpha} \cdot \hat{k} \approx 1, \tag{9}$$

or quasi-shear when,

$$\hat{\alpha} \cdot \hat{k} \approx 0, \tag{10}$$

although these terms may differ in the literature [5]-[7].

2.1.2 Lamb Waves in Anisotropic Media

When a medium contains boundaries, longitudinal and shear waves form interactions with these boundaries to produce guided waves. These guided waves propagate within a medium along the boundaries, which in turn "guide" the wave and obey the same equation of motion for bulk waves while meeting the appropriate boundary conditions. Guided waves are categorized into four main wave types based on various boundary conditions: Lamb, Rayleigh, Love, and Stonley. Lamb waves exist in thin plates or layers as they propagate along the stress-free boundaries [8], Rayleigh waves propagate in similar media but are guided along the surface of a single stress-free boundary [9], and Love and Stonely waves exist and propagate in a single layer on a half-space and the interface between two solid half-spaces, respectively [10], [11].

Out of these four wave types, Lamb waves are primarily of interest here. Lamb waves can only be generated in materials of a few wavelengths thick but because of the abundance of plate-like structures in industry, they have become a primary focus in ultrasonic NDE research. Lamb waves have the capability to propagate long distances with relatively low amplitude attenuation when compared with bulk waves. This characteristic allows Lamb waves to maintain sensitivity to damage in large plate-like structures. However, despite these advantages, they are also multi-modal and highly dispersive in nature, which increases the complexity of received signals after wave propagation.

For anisotropic composite panels, the wave modes are Lamb-like and can exist as an infinite number of modes depending on the frequency, thickness of the plate, and direction of propagation relative to axis symmetry. These modes are commonly referred to as quasi-

symmetric or quasi-antisymmetric depending on their displacement profile in the cross-section of the plate. The lowest order modes are commonly denoted as quasi-A_0 and quasi-S_0 but for the remainder of this thesis they will be referred to as A_0 and S_0 modes for simplicity. These modes can exist and propagate at different velocities based on the wavelength relative to the thickness of the medium.

Dispersion refers to the wave propagation velocity varying with frequency. This results in a change of the overall wave shape to a wave packet as it propagates in a medium. In isotropic media, dispersion is well understood where the relation of wave velocity and frequency for each Lamb wave mode is described via a dispersion curve. However, to simplify interpretation of measured signals, lower frequency narrow-band excitations can be used to only excite lower order modes, e.g. the A_0 and S_0 modes, and minimize dispersion [1], [5].

2.2 Ultrasonic Measurements

NDE methods utilizing ultrasonic waves as a form of damage interrogation have been used for decades in industry. They are well suited for many commercial applications because of their ability to detect small damage in high detail and have reduced safety risks compared to X-ray methods. Newer ultrasonic methods such as wavefield imaging are frequently used in the laboratory to visualize wave interactions with anomalies within a material for damage characterization and localization.

2.2.1 Ultrasonic Inspection Methods

Ultrasonic testing (UT) refers to using ultrasound as a non-destructive testing method for making detailed characterizations and dimensional measurements of a material or a flaw

within that material. UT methods are commonly performed in industry for evaluating a part or the current health of a structure [12], [13]. UT inspection systems use ultrasonic waves as the excitation method in which pulsed excitations are transmitted into a material and received waves are measured in either a pulse-echo (single transducer) or through-transmission (dual transducer) configuration. There are many advantages to performing UT inspections over other NDT methods. These include higher sensitivities to surface and subsurface discontinuities where only single sided access is needed when performing pulse-echo measurements. Results are almost instantaneous and can be coupled with automated systems for detailed imagery, and they can be highly accurate in estimating shape and size of defects [12]. For these reasons, UT methods are excellent tools for characterizing internal damage in composite materials.

The two common UT methods used in industry for detecting and characterizing damage are pulse-echo and through-transmission. Pulse-echo mode determines the location of a defect from scattered waves signals that return to the original source transducer, which are typically resolved in time. The flaw's depth can be determined by comparing time of flight between an early scattered arrival caused by the defect and a back surface reflected wave. Through-transmission uses an independent source and receiver configuration to determine flaw location and size through energy level differences of the transmitted waves [13]. Unlike pulse-echo scans, through-transmission scans are performed by transmitting waves on one side of the material and receiving on the other. An example of each configuration can be seen in Figure 1. These methods exist commonly in industry and are performed using multiple types of equipment. The essentials for performing inspections are done using a pulser/receiver, transmitting and

receiving transducers, and an oscilloscope or some other device for viewing time and amplitude ultrasonic signals. These measured signals can typically be recorded over an evenly spaced grid to produce images of a planar material for determining the existence, location, and size of damage [12].

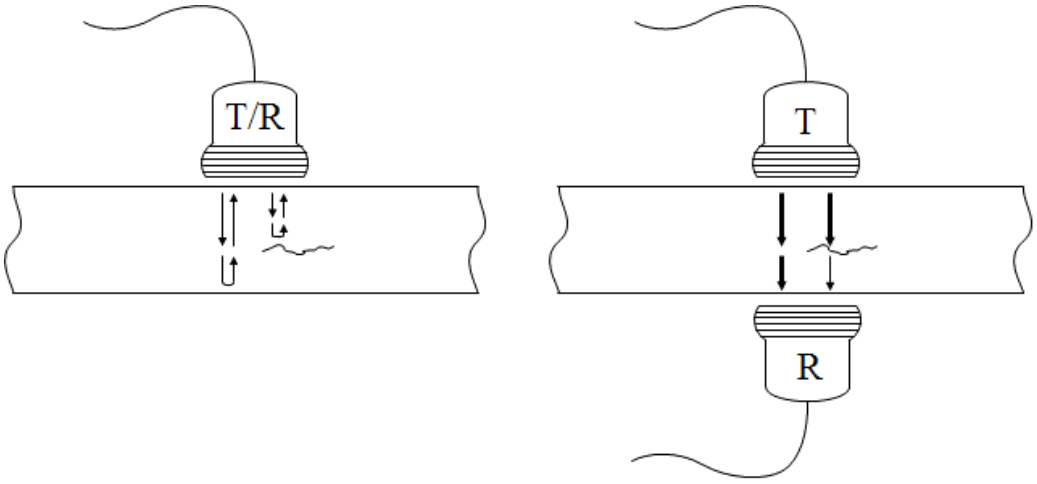

Figure 1 – Diagram of a pulse-echo and through-transmission setup.

2.2.2 Wavefield Imaging

Wavefield imaging refers to capturing wave motion on the surface of a material resulting from a spatially stationary excitation. This wave motion is represented using time-domain amplitude signals commonly measured in a 2-D rectilinear grid to form three-dimensional data, $w(t, x, y)$, where *t* is time and *x* and *y* are spatial positions on the material's surface. A common approach to acquiring such data utilizes a contact transducer to introduce ultrasonic waves and a laser Doppler vibrometer (LDV) to measure the displacements associated with the elastic wave's motion. This is done using either mechanical motion to move the laser head of the LDV over the material's surface [14] or by using systems with precision controlled mechanical mirrors [15]. The result is high fidelity wave motion that can be visualized to provide a more intuitive understanding of wave propagation and the

interactions experienced with boundaries and anomalies. Alternatively, an air-coupled ultrasonic transducer could be used instead of an LDV to provide rapid scanning but the quality of wavefield images acquired are typically reduced with impedance mismatch between air and the material being the largest contributing factor [16], [17].

Wavefield imaging has proven to be a valuable tool for studying guided waves in various materials and quantifying their interactions with defects and damage [18]. These studies have shown the versatility in using an LDV. For example, LDVs used to measure guided waves have been able to identify voids and damage in reinforced-concrete walls [19], localize thickness variations in aluminum using sub-1 MHz waves [20], and investigate characteristics of piezoceramic sensor damage and degraded performance [21], just to name a few. Additionally, efforts have been made to use LDVs for composite material inspection where studies have shown improved identification of matrix cracking and layer delaminations [22].

2.2.3 Representation of Data

Ultrasonic data can be measured in numerous formats, but it is important to represent data concisely. Three of the most common ways to represent ultrasonic data are A-scans, B-scans, and C-scans [12], [23]. In the context of ultrasonic inspection and wavefield imaging, these three formats will serve as the general form of representation for data presented in this thesis.

A-scan, short for Amplitude scan, is the primary format for which data are represented when measured. A natural way to represent an ultrasonic signal is by a function of time, $f(t)$, a one-dimensional representation of amplitude data along a horizontal axis. In ultrasonic inspections, the expected signal reflections from a boundary or edge presented

in an A-scan can be compared with unknown reflections that typically signify subsurface damage. For wavefield imaging, A-scans are signals obtained at a single spatial location, $w(t, x_0, y_0)$, within the wavefield.

A B-scan represents data measured in two-dimensions, one space and one time, typically along a linear spatial path. It can be displayed as an image formatted from a series of A-scans, $f(x,t)$, where the wave's time-of-flight is commonly displayed along the vertical axis and the location of the transducer is represented in the horizontal axis. For wavefield B-scan data, which is represented as $w(t, x_0, y)$ or $w(t, x, y_0)$, the propagating wave motion is measured along a single spatial dimension. In general, B-scan measurements for ultrasonic inspection are used to determine depth and width of subsurface damage [23] whereas B-scan wavefield data can be used to analyze propagation characteristics of a wave [18].

A C-scan refers to data represented as a function of two spatial variables. A two-dimensional C-scan, $f(x, y)$, can be constructed by extracting features from a 2-D spatial assemblage of A-scans. The time-of-flight corresponding to peak amplitudes within a time window at each spatial location in $f(x, y)$ can reveal the depth of damage while the peak amplitudes for each spatial location or a time summation of energy can be computed from $w(t, x, y)$. For 3-D wavefield data, the C-scan $w(t_0, x, y)$ is also called a "snapshot" [18].

2.3 Lamb Wave Scattering from Defects

Scattering is a result of incident waves encountering structural discontinuities or damage. For bulk waves, scattering occurs in three dimensions as the waves can propagate within the thickness of the material due to the wave's small wavelength. On the other hand, Lamb

waves propagate along plate boundaries where scattering can be treated as 2-dimensional. The reduced complexity of Lamb wave scattering can be described through incident and scattered angles and is illustrated by Figure 2 for a point-like scatterer. The scattering from a defect is related to its location, form, orientation, shape, and size and can be quantified by scattered amplitude values as a function of incident direction and scattered direction. Scattered wave directions are defined by the direction of the wavenumber vector for both incident and scattered waves as shown in Figure 2. Scattered waves that propagate in the same direction as incident waves (i.e., a positive inner product of their wavenumber vectors) are referred to as forward scattering while scattering in the opposite direction is referred to as backscattering.

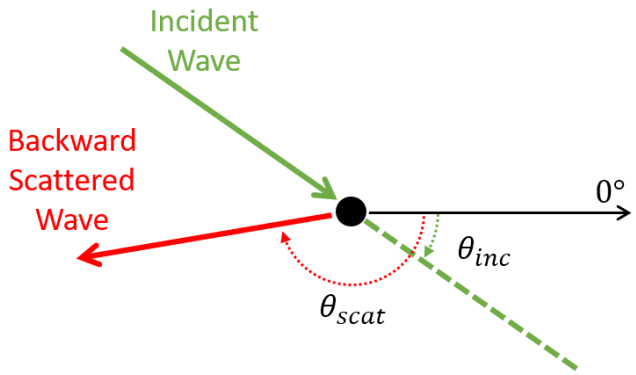

Figure 2 – Illustration of incident and scattered waves.

One method for quantifying scattering uses transmission and reflection coefficients that define an amplitude or energy ratio between the incident and scattered waves; however, this limits the description of scattering to a specific incident direction and does not provide additional information for alternate scattering directions [5]. This limitation has been addressed by describing all scattering directions through angular patterns for a specific incident direction, which has been applied to characterization of scattering from notches, through-holes, and cracks via experimentation and simulation in isotropic media

using guided waves [24], [25]. Extensions of this work by Chen *et al.* [26] showed how scattering patterns could be represented by a scattering matrix through experiments with guided waves in aluminum. The scattering amplitudes populate the matrix corresponding to the appropriate rows and columns that represent incident and scattered angles, respectively.

While defect scattering from guided waves in isotropic media has been well researched, guided wave defect scattering in composites, which are anisotropic, is more complicated. Common defects that form in composites, such as matrix cracking and delaminations, have more complicated scattering effects influenced by material anisotropy. For cracks in composites, studies have shown that significant correlation exists between scattering amplitude, incident wave frequency, and the size of cracks being evaluated with the S_0 and A_0 wave modes. For interrogation methods using the S_0 wave mode, studies by Bratton *et al.* [27] showed that the relations between scattering amplitude and crack depth were difficult to interpret but that their results showed the scattered signals were affected. Correlation between S_0 wave velocity and crack density was revealed through experiments by Toyama *et al*. [28] and led to a crack detection method that utilizes this changing S_0 wave velocity [29]. Karunasena *et al*. [30] showed how scattering from a crack of various lengths behaves differently for S_0 and A_0 modes and work from Karim and Kundu [31] showed that scattering amplitudes from an incident A_0 wave mode continually reduces as the length of a crack approaches the thickness of the plate.

The interaction of S_0 and A_0 wave modes with composite delaminations has also been a focus of research. Delaminations, which are layer disbonds in composites, can have various effects on scattering behavior based on their size, depth and shape. The depth of

the delamination can significantly affect S_0 scattering [32]; however, delaminations are more sensitive to the A_0 wave mode [33]. The frequency of the wave and the size of the delamination also play a significant role in how scattering occurs [34]. Hu *et al.* [35] verified through an experimental study that backscattering occurs more strongly at the entrance of the delamination rather than the exit and that the overlap of multiple backscattered waves in smaller delaminations can produce higher amplitude waves. In general, the interaction of the A_0 wave mode with a delamination produces backscattered waves that are smaller in magnitude than forward scattered waves [36]. This variation in scattering amplitude as a function of direction has been studied using finite element modelling (FEM) to analyze the angular-dependent scattering nature of delaminations and results have also been compared with some experimental studies [37]. Work by Murat *et al*. [38] compared finite element simulations with experimental data regarding angular scattering from multiple incident angles and it was shown that delamination depth and width can have a significant effect on scattering directivity. Full characterization of real delamination scattering as a function of both delamination size and depth is crucial to the improvement of NDE inspections, and in particular, SHM methods utilizing *in situ* imaging.

2.4 Guided Wave Propagation in Composite Media

Compared to isotropic media, guided wave propagation in homogenous anisotropic media is considerably more complicated due to wave mode coupling for off-symmetry wave propagation. These complications are further exacerbated in anisotropic layered composites due to their heterogeneous nature and layered structure. It is possible to approximate each layer as a homogenous orthotropic material; however, this assumption

is only valid for modal wavelengths much larger than individual fibers. Anisotropic material properties can cause directional dependence in the propagating waves. Specifically, phase and group velocities are affected based on the direction of propagation as well as amplitude attenuation. Energy of the wave tends to concentrate along directions of stiffness within the material and is weakened for paths that deviate from the fiber directions [39]. These complicated wave mechanics can affect SHM performance and should be properly characterized to improve the effectiveness of SHM methods.

Numerous methods are used in research and practice to characterize wave propagation in anisotropic media. In general, the most common methods performed can be classified in one of three categories: analytical models, finite element modeling (FEM), and experimental methods. Analytical models are derived from fundamental wave theory to predict wave motion and corroborate results from experimental and FEM methods. There are no closed form solutions for dispersion curves in either homogeneous or layered plates, but there are methods that have been developed to predict dispersion for anisotropic layered media using numerical approximations [2]. A general approach is to derive a matrix that describes the elastic wave interactions between layers. The original development of the transfer matrix (TM) by Thomson [40] for isotropic media, which was later improved upon by Haskell [41], combines the displacements and stresses above and below each layer to represent the wave propagation mechanics for the entire medium. Nayfeh [42], [43] continued this work and extended its application to composites with anisotropic layers; however, the matrix formulation suffers from numeric instability as the number of layers increases. Other methods do not have this instability issue, such as the global matrix (GM) method by Knopoff [44], the stiffness matrix (SM) method developed

by Kausel [45] and improved upon by Rokhlin and Wang [46], as well as others. The GM method, which addressed the numerical instability, suffers from inefficient computational time for panels with many layers. SM on the other hand reformulates the TM method to have only exponential terms and greater simplicity making it unconditionally stable when solving for dispersion relations. Numerous other methods that approximate composites as a general anisotropic medium have also been developed but apply specifically to certain layer symmetries or a limited number of layers and often produce inaccurate results for higher frequency waves. Additional context and information on these methods can be found in [47]-[51].

Finite element modeling is becoming more prevalent for modeling wave propagation as computational power continues to grow. It can simulate more complicated wave behavior at higher frequencies that generalized approximate analytical methods fail to accurately predict. To properly characterize guided Lamb wave propagation with FEM, careful consideration must be taken for modeling the signal input for both symmetric and antisymmetric wave modes, in addition to accurately describing the material's elastic properties and layer stacking pattern. For composite layered media, these properties can vary significantly from different manufacturers, and with such a large variation in panel properties, results from FEM are typically obtained for a specific composite medium. Additionally, the required size of an element and length of time step play a significant role in the accuracy of the simulation results. These two properties are often chosen to be a $1/20^{th}$ or less of the smallest wavelengths and 20 times larger or more than the largest frequencies evaluated during the simulation [52]. This relation between element size and

time step size, to wavelength, and frequency can cause a significant increase in simulation run times.

FEM has been used in numerous studies to estimate dispersion in composites and other anisotropic media. Nurhaniza *et al.* [53] and Sabau *et al.* [54] used FEM to analyze unidirectional fiberglass mechanical properties using commercial software like ABAQUS or SolidWorks Simulation Software. Kim *et al.* [52] studied directional propagation behavior of Lamb waves in quasi-isotropic CFRP panels using ANSYS commercial software in addition to Disperse [55], a software package utilizing the global matrix method, and experimental analysis, and showed good agreement between all three methods. Other in-depth comparisons between analytical, experimental and finite element modeling have also been done by Leckey *et al.* [56]. They examined guided wave propagation in an orthotropic CFRP laminate was examined using four finite element methods: ABAQUS, ANSYS, COMSOL and custom code implementing a Elastodynamic Finite Integration Technique (EFIT), as well as experimental validation using laser Doppler vibrometry and theoretically calculated dispersion curves from Disperse. The overall results showed adequate agreement between FEM results and the experimental and analytical approaches. Additional applications of FEM to composites can be found in [57]-[61].

Experimental analysis of guided wave propagation is often used to validate the accuracy of predicted results from either analytical theory or simulation. Additionally, experimental wave propagation characterization can be used for materials of unknown material properties. The type of experimental analysis used can vary by method and application due to the type of material being evaluated and the characterization being

performed. Specifically, for composite laminate materials, several LDV and air-coupled transducer experimental procedures have been developed to obtain dispersion relation information and material attenuation properties. One method known as ultrasonic polar scan (UPS) utilizes a non-contact transducer to insonify a spot on a plate specimen at all possible angles of incidence. The reflected or transmitted amplitudes are then recorded as a polar map that indicates the local mechanical stiffness of the material. Slowness, the inverse of phase velocity, as well as energy flow can be extracted from the recorded data and used to build a dispersion relation by repeating the experimental procedure for various frequencies. Several examples of this method have been performed by Kersemans *et al.* [62] specifically in anisotropic composites. Nadella *et al.* [39] used an alternative method to estimate guided-wave propagation characteristics using an LDV to measure radial lines emanating from a transducer source over a 65 mm distance at 5 separate angular directions. The source was excited at 75 kHz to produce a predominantly antisymmetric wave mode in a composite plate to characterize radial attenuation as a follow-up approach to theoretically calculated estimates. Harb and Yuan [63] used a similar approach by generating Lamb waves with an air-coupled transducer and recording radial lines with an LDV to estimate phase velocity within an anisotropic composite plate over a range of angular directions.

2.5 Structural Health Monitoring

Structural health monitoring (SHM) is a newer research area within NDE that focuses primarily on monitoring a structure's condition in "real-time" through an embedded sensor system. The main advantage for using SHM is the possibility to alleviate rising maintenance cost concerns by replacing scheduled-based maintenance with condition-

based maintenance, which reduces time that the structure must be removed from service while promptly identifying the existence of new damage. This can be achieved using either passive or active means. At the passive level, natural excitations that are generated during the structure's use can be used to help infer life expectancy of parts or the structure through developed algorithms. In contrast, active SHM directly monitors the presence of structural damage through actuation and sensing using permanently embedded transducers. Direct actuation of a structure provides greater flexibility than passive methods by controlling excitation signals and the measurements performed. Additionally, configurations for application-specific transducer arrays and signal processing algorithms can be implemented for improved damage detection [64], [65].

2.5.1 Non-Guided-Wave SHM

Numerous methods have been developed to interrogate composites for damage using SHM. Each method uses a form of sensor or sensors that are placed permanently across a structure, but they must also be affordable and lightweight so that they do not impose on the practical use or integrity of the structure. Each SHM approach to detecting damage for composites requires a different type of sensor, which includes resistance-based strain gauges, fiber optics sensors, electrical sensors that measure resistance, impedance, etc.

Methods that use conventional resistance-based strain gauges for damage detection are relatively straight-forward in approach. Relative resistance changes are monitored over the use of a structure until impact stress or any stress-induced damage is detected. The simplicity of such a monitoring system is also one of its biggest disadvantages as a long-term monitoring solution. The performance of theses gauges is commonly affected

by bonding issues or strain drift caused by extensive strain applied over time, making damage detection less sensitive or even impossible depending on the severity of damage to the sensor [2].

Another solution that addresses these drawbacks is the use of fiber optical sensors. Their immunity to electromagnetic interference, resistance to corrosion, sensor multiplexing over individual fibers, and ability to directly embed the optical fibers into the composites makes for robust performance over a variety of conditions. Damage is detected through fiber breakage or signal changes from strain or thermal expansion and can be quite accurate in localizing the damage when using cross-ply fiber directions. Optical signals can be measured in real-time to detect sudden impacts to the structure and perform localization and even characterization of the damage. They are not without limitations though. Expensive optoelectronic equipment is needed to make sense of the optical signals measured via complicated processing, in addition to the increased manufacturing cost of imbedding the optical fibers which can have a negative impact on the integrity of the structure [66], [67].

Damage sensing using the electrical properties of a composite material has also been studied as possible form of SHM. Carbon fibers are inherently conductive and are embedded in a insulative epoxy resin. Composites with densely packed fibers can be monitored for damage by measuring the electrical changes within the composite itself as the electrical characteristics of the composite can change from fiber cracking and inter-ply delaminations. This idea of “self-sensing”, which requires no additional sensors for active monitoring, is very cost effective and only requires electrodes to be attached for interfacing with monitoring instrumentation. The issue with this type of sensing, however,

is the interpretation of signal changes can be challenging as the electrical characteristics can vary even under normal use [68].

As an alternative to ultrasonic guided wave SHM, bulk waves have also been used with metallic structures for monitoring fatigue cracking. These cracks typically form in components under high flexural stress near fastener holes or notches where service in these areas of a structure are critical. Regions such as these can be interrogated with angle beam transducers to monitor crack generation and crack growth. While bulk waves in SHM are not a main research focus due to limited applications and feasibility, several studies have been conducted to analyze bulk wave signals and their interactions with cracks. A study done by Gupta *et al.* [69] showed how statistical analysis of the signals over time can be used for early detection of developing cracks emanating from a through-hole. Michaels and Mi [70], [71] determined that there was high correlation between ultrasonic signal energy and crack area in aluminum, but that variable loading at the damage location can affect results. Studies in microstructural changes in railroad steel have been conducted to determine crack origination and precursors for their generation. Kenderian *et al.* [72] examined the changes in ultrasonic attenuation and velocity for steel and how they correlate with material fatigue early on.

2.5.2 Ultrasonic Guided Wave SHM

Ultrasonic guided wave testing has emerged as an effective way to estimate location, severity and the type of damage. It is suitable as an SHM method utilizing transducer elements in a sensor network for damage sensing. Two approaches to guided wave SHM are pulse-echo and pitch-catch. Like the pulse-echo method for UT testing, a single source

or two collocated sources are used for actuation and sensing. A narrow-bandwidth pulse is transmitted into a specimen while echoes from the travelling pulse are recorded. Echoes that do not corresponds to boundaries or have unexpected arrival times are assumed to be those corresponding to defects or damage. In the pitch-catch scenario, as for through-transmission UT testing, the excitation is sent across the specimen by a source and recorded by another transducer element. The received signals can then be analyzed for delayed arrivals, echoes from scattering, amplitude changes, variations in frequency of the wave packet, etc. This type of in-depth analysis requires a network of transducers to adequately locate existing damage. Critical elements in the effectiveness of guided wave SHM are the transducers, signal processing methodology, array configuration and SHM architecture (supporting electronics, system robustness and packaging). Additionally, Lamb waves are the typical wave mode generated using these sensors and they can propagate significantly larger distances than bulk wave modes. This allows for large coverage of a structure to be interrogated with a small number of transducers and minimal equipment, making this a potentially cost-effective approach to SHM for composites [2], [64], [65], [68].

2.5.2.1 Baseline Subtraction

Most guided wave SHM applications involve baseline subtraction, a technique used to isolate the changes between two signals to help identify damage. These changes can be a result of external stress, impacts, or other instances of incurred damage. Ultrasonic signals are recorded when the structure is in a known condition and are typically referred to as baselines. After obtaining proper baselines, measurements are made at specific time intervals or after an event has occurred that would require structural health examination.

These measured signals, or current signals, are differenced with the previously acquired baselines to produce residual signals. Residual signals are examined for structural changes, e.g. damage, over the structure's life to both detect new damage and monitor existing damage.

The sensitivity of these residual signals to damage is dependent on appropriately matching baselines with current signals as uncontrolled environmental conditions can affect measurement consistency. Variations in temperature affect the speed of guided waves, which negatively influences baseline subtraction and makes it difficult to distinguish damage from temperature effects [73]. Methods such as optimal baseline subtraction and baseline signal stretch have been developed to compensate for environmental temperature changes [74], [75]. A combination of both methods by Lu *et al.* [76] showed improved performance of baseline subtraction over the individual methods by reducing the variability between the baseline and current signals.

2.5.2.2 Localization and Characterization via Transducer Arrays

Baseline subtraction is used in guided wave SHM applications for damage localization and characterization by many sparse array imaging algorithms. The differenced signals obtained after baseline subtraction contain scattered echoes that typically correspond to some form of damage. The first arrival of these scattered waves, which is assumed to be from the damage location, along with direct arrivals from source to receiver can help calculate relative distances between source, receiver, and the damage if the propagation velocity is either known or estimated. To triangulate the damage's location, a minimum of three unique transducer pairs is needed where an increase in transducer pairs can improve localization robustness in the presence of noise and edge reflections. More

directly, the amplitude of residual signals can be used to estimate the certainty for which damage is present and to possibly quantify its size. This need for multiple transducer pairs makes transducer arrays suitable for damage localization and characterization.

One possible guided wave sensor configuration that can be used is called a beamforming phased array. Phased arrays are compact in size and can steer guided wave beams within a structure by varying the transducer signal phases through electrical or synthetic means. These arrays are designed as transceivers that can transmit guided waves and receive scattered waves from defects within the beam focus direction while attenuating waves from all other directions. Research in this area for SHM is promising when applied to isotropic steel and aluminum materials [77], [78]. In composites, newer techniques and phased array designs are being developed to compensate for complicated wave propagation [79], [80]; however, smaller inexpensive arrays with simplified beam-forming algorithms can have limited area coverage due to low signal-to-noise-ratios affecting damage location performance [81].

In the case of guided wave SHM for larger areas, one of the most suitable sensor configurations is the spatially distributed array, or sparse array, due to the reduced total number of transducers needed to monitor a structure with fairly uniform sensitivity. Measurements are made by exciting one transducer and receiving on another. This is done for each transducer pair within the array. Baseline and current data are acquired and subtracted to detect changes in structural features. Various algorithms use baseline subtracted data as a foundation for localizing damage such as the delay-and-sum (DAS) algorithm originally proposed by Wang *et al.* [82] and the MV algorithm proposed by Hall and Michaels [83]. The MV algorithm incorporates *a priori* defect scattering information

to improve imaging performance. Hall *et al.* [84] demonstrated the success of using a sparse array with MV imaging to locate a through-hole in a composite plate using a rough approximation of the expected scattering. It is expected that further imaging improvements can be made provided more accurate quantitative scattering information is acquired.

2.6 Research Context

The literature review of guided wave SHM, as it pertains to anisotropic composite media, shows that there is a need for efficient characterization of damage for improving *in situ* imaging. Current sparse array imaging in isotropic media has been presented as a method to help monitor structural performance with real-time damage detection. The use of anisotropic composites for high stress and strain applications is on the rise and SHM imaging methods can benefit from incorporating complicated wave propagation effects and damage-specific scattering behavior associated with the material.

The main context of this research is focused on two aspects, guided Lamb wave propagation characterization and estimating damage scattering for improving sparse array imaging. Wave propagation in composite materials can vary significantly with propagation direction and is difficult to characterize analytically. A methodology for estimating wave propagation parameters experimentally utilizing wavefield imaging is explored. The second aspect of this research is to estimate high-resolution scattering for a variety of artificial and impact damage applied to composite panels of different layer symmetries, in addition to performing detailed UT of the damaged panels. The estimated

scattering results are applied to MV sparse array imaging and the imaging performance results are discussed.

3 CHARACTERIZING ANISOTROPIC WAVE PROPAGATION

This chapter presents an experimental methodology for characterizing anisotropic wave propagation, which is relevant for most composite materials that use fibrous ply layers in their structural composition. Specifically, phase and group velocity, in addition to material wave amplitude attenuation, are characterized for angular dependency in plate-like composites. The chapter concludes with a summary of experimental results from quantifying anisotropic wave propagation that are used in methodologies for estimating scattering.

3.1 Experimental Procedures

3.1.1 Panel Description

Two composite panels with a quasi-isotropic structure were purchased from Allred and Associates, Inc. [85] and used for separate experimental measurements in this study. Each panel had a smooth polished side and an unfinished side that was coarse from the exposed fibrous weave. For characterizing certain properties of anisotropic wave propagation, the smaller of the two panels, Panel A, measuring 309 mm × 309 mm × 3 mm (part number FDPLSC04G1212), was used. Additional information regarding the material properties, number of ply-layers, etc., was not available from the manufacturer.

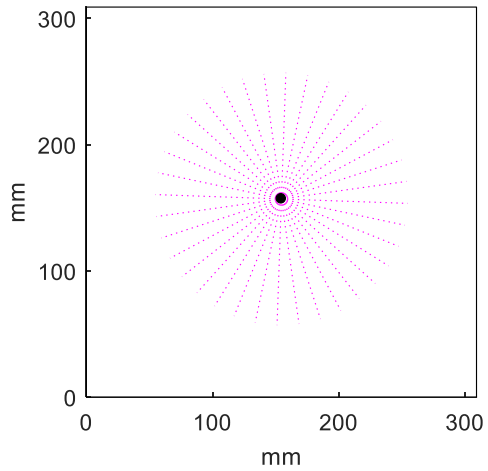

Figure 3 – Layout of Panel A with attached transducer (black dot) and defined path of radial wavefield fan scan (magenta lines).

3.1.2 Laser Vibrometer Measurements

Wavefield data were recorded along straight lines emanating radially from a single transducer permanently attached to the center of Panel A. The attached transducer was a 7 mm diameter × 0.5 mm thickness lead zirconate titanate radially polarized disc with a resonant frequency of 300 kHz. Each recorded line, beginning at the transducer's center, had a length of 100 mm and a radial increment of 2 mm. In addition, each segment was separated by an angular increment of 2° to measure the variation of wave velocity and amplitude attenuation along different propagation directions. A diagram of the panel and wavefield measurement paths can be seen in Figure 3.

A linear sine wave chirp excitation from 40 to 150 kHz was generated using an Agilent 33250A arbitrary waveform generator at 300 mVpp over a 200 μs time window. The chirp was then amplified using an E&I 1040L amplifier to approximately 100 Vpp. The use of the chirp permits deconvolution of the signals during post processing to any specified excitation tone burst within the transmitted bandwidth [86]. For this study, all data were post-processed to an equivalent response from a 3-cycle, 80 kHz, Hann-windowed tone

burst excitation. This burst was chosen so that the effects of the lowest order antisymmetric wave mode could be studied in an anisotropic composite material.

Wavefield measurements were obtained using a Polytec OFV-551 single point laser Doppler vibrometer (LDV) and corresponding Polytec OFV-5000 controller. The laser fiberoptic sensor was mounted to an XYZ carriage controlled by custom LabVIEW software that controlled moves point-to-point in either a raster pattern or a custom pattern defined by a pre-generated list of coordinates. The output of the LDV controller was amplified by 3 dB and bandpassed filtered from 30 kHz to 500 kHz with a Panametrics 5058PR pulser-receiver and then subsequently digitized by a Cleverscope digital oscilloscope model CS328A at a sampling frequency of 20 MHz and then down sampled to 2.5 MHz for postprocessing. The on-board averaging feature of the Cleverscope was enabled so that 64 averages were taken to help supress noise at each spatial location.

Wavefield data were recorded from the smooth finished side of the composite panel, which was opposite the side instrumented with the transducer. Although the surface was smooth, it exhibited poor optical reflectivity. This reflectivity issue can cause added noise to the measured signals using the LDV system. Efforts were made to reduce this affect by adding a layer of chrome automotive vinyl tape [87] that was applied to the scan region to improve optical reflectivity and minimize any nonhomogeneous surface effects. Additionally, adhesive putty tape was applied to the edges of the panel to dampen edge reflections and thus minimize their interference with the desired direct arrivals.

Spatial sampling was considered when choosing the 2 mm radial resolution given the frequency range of the excitation used. The minimum spatial sampling interval, or Nyquist

sampling interval, is based on the smallest wavelength and is calculated from maximum frequency contained within the excitation signal and the slowest phase velocity during wave propagation,

$$\Delta x = \frac{\lambda_{\min}}{2} = \frac{c_{p\min}}{2 f_{\max}}. \tag{11}$$

The linear sine chirp excitation of 40 to 150 kHz, contains a maximum frequency component of ~150 kHz. In composites, to estimate the minimum phase velocity, dispersion curves are commonly generated from theoretical models that contain the elastic constants associated with the layers of the composite material. This information, specific to the composite, was unavailable from the manufacturer. However, similar thickness quasi-isotropic materials from prior experiments exhibited minimum phase velocities no smaller than 1 mm/μs for the lowest order antisymmetric wave mode generated using the same excitation signal. Since the sampling interval is directly proportional to phase velocity, 1 mm/μs is used as a conservative number to estimate the minimum spatial sampling interval needed to prevent aliasing. Substituting both the maximum frequency and minimum phase velocity quantities into Equation (5) yields a minimum spatial sampling interval of 3.33 mm/μs; thus, the 2 mm spatial resolution chosen should be sufficient to prevent spatial aliasing.

3.2 Phase and Group Velocity Estimation

3.2.1 Application of the Radon Transform

An algorithm known as the Radon transform has been used for medical imaging and seismic wave identification in geophysics [88],[89]. Here it is adapted for extracting group

velocities and phase velocities of the quasi-A_0 guided wave mode along radial scan lines (radial B-scans) obtained from composite panel wavefield data for different propagation directions. Given B-scan data $f(x,t)$, the variables x and t, correspond to propagation distance and time, respectively. The Radon transform obtains a projection along a line within the data for a range of slopes and intercepts. The digital implementation of the projection is a sum of the pixel intensities within the image along a line with intercept τ and slope $1/c$, where τ corresponds to the time offset at $x = 0$ and c corresponds to the wave speed [88]-[90]. The integral form of the Radon transform $R(\tau,c)$ can be written as [91], [92]:

$$R(\tau,c) = \int_{-\infty}^{\infty}\int_{-\infty}^{\infty} f(x,t)\delta\left(t-(x/c+\tau)\right)\mathrm{d}x\mathrm{d}t\,, \tag{12}$$

where $\delta(t)$ is the Dirac delta function. Often called a Radon panel, the digital implementation is,

$$R(\tau_i,c_j) = \sum_k f(x_k, x_k/c_j+\tau_i)\,, \tag{13}$$

where the sum is taken over all pixels that fall within the B-scan data. For the application here of estimating wave velocity, the location of the peak (τ_{max}, c_{max}) within the Radon panel corresponds to an estimated wave speed of c_{max} at a time offset of τ_{max}.

Figure 4(a) shows a waterfall plot of the measured signals where the vertical axis is the radial coordinate, Figure 4(b) shows the B-scan as an image, and Figure 4(c) shows the Radon panel for a velocity range of 0.5 to 3.5 mm/μs and a time offset range of -5 to 55μs. The peak occurs at (τ_{max}, c_{max}) = (7.8 μs, 1.12 mm/μs) and is indicated by the open triangle on the image. These values correspond to a line going through the peaks as shown

on the waterfall plot. Since the signals are not rectified, c_{max} = 1.12 mm/μs is an estimate of the phase velocity at the center frequency of 80 kHz.

The dispersive nature of the signals is evident in Figure 4(a) because the location of the peak within the wave packet changes as a function of propagation distance. Figure 5 shows the corresponding plots for the signals after envelope detection. The peak of the Radon panel, which is at (τ_{max}, c_{max}) = (20.9 μs, 1.45 mm/μs), differs from the one of Figure 4(c) since it corresponds to the velocity of the wave packet; i.e. the group velocity.

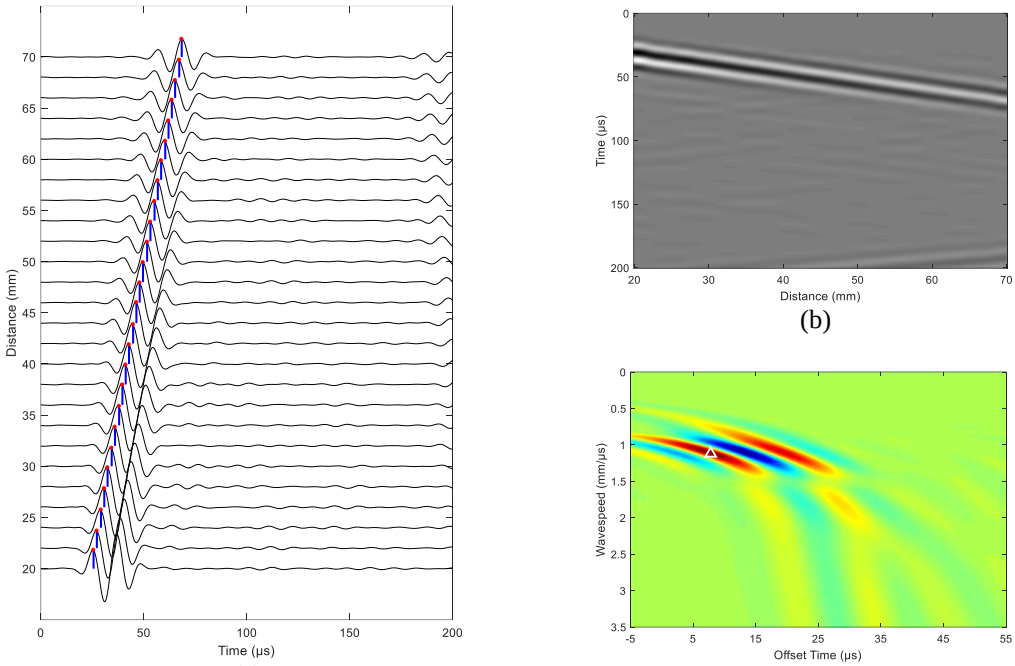

(a) (b) (c)

Figure 4 – Example of radial B-scan from Panel B wavefield data at +45° showing estimation of phase velocity. (a) Waterfall plot of signals, (b) B-scan image, and (c) Radon panel.

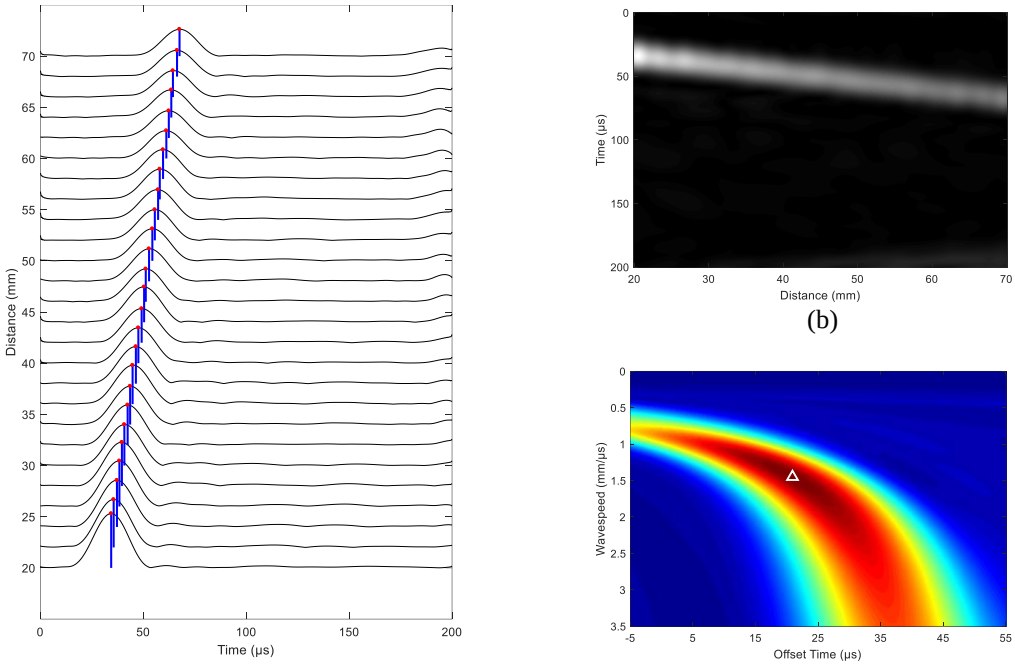

(a) (b) (c)

Figure 5 – Example of radial B-scan from Panel B wavefield data at +45° showing estimation of group velocity. (a) Waterfall plot of signals, (b) B-scan image, and (c) Radon panel.

3.3 Attenuation Estimation

3.3.1 Modeling Amplitude Attenuation

Amplitude attenuation is dependent upon the direction of propagation within the panel. To estimate this attenuation for all propagation directions, peak amplitudes are extracted from rectified radial B-scans using a narrow time window of 20 μs centered at the nominal arrival time,

$$t_{arr}(\theta) = \frac{r}{c_g(\theta)} + \frac{N_c}{2f} + t_{off}\,. \tag{14}$$

These arrival times are calculated using the group velocity profile, $c_g(\theta)$, estimated from the same data; r is the radial distance along the B-scan, N_c and f are the number of cycles

and frequency associated with the tone burst excitation, and t_{off} is a calibrated time offset associated with the real-time excitation of the transducer.

Once the amplitude values have been extracted, amplitude attenuation is characterized using two models that are a function of both direction of propagation and radial distance from the source. The first model is defined as,

$$A(r,\theta) = \frac{A_0(\theta)}{\sqrt{r}}, \tag{15}$$

where θ is the direction of propagation, $A_0(\theta)$ is the reference peak amplitude at a distance of 1 mm, r is the radial distance from the source, and $A(r,\theta)$ is the peak amplitude in the θ direction at a distance r from the source. This equation is motivated by the simple cylindrical spreading loss exhibited by guided waves propagating in an isotropic plate while including directional dependence.

Cylindrical spreading loss is the main source of attenuation for an isotropic plate, however, composite materials contain additional loss mechanisms such as matrix viscosity and energy losses from the fiber matrix interfaces [39], [93]. To better incorporate these material attenuation losses, the second model includes an exponential decay in addition to the cylindrical spreading loss,

$$A(r,\theta) = \frac{A_0(\theta)e^{-\alpha(\theta)r}}{\sqrt{r}}, \tag{16}$$

where $\alpha(\theta)$ is the θ-dependent amplitude decay rate. This exponential decay term effectively incorporates all additional loss mechanisms to provide a complete estimation of θ-dependent attenuation.

3.3.2 Material Inhomogeneity Correction

Material homogeneity refers to uniform structural composition throughout a material. If an anisotropic composite is truly homogeneous, it will exhibit the same propagation characteristics along directions separated by 180° (i.e., the waves propagating forwards and backwards along identical axial directions will have the same velocity and attenuation). To minimize any discrepancies from the acquired data related to lack of homogeneity, additional post-processing was performed by averaging points corresponding to a 180° separation in wave propagation direction. This averaging was applied after estimation of phase and group velocities and prior to modeling amplitude attenuation.

3.4 Panel A: Quasi-Isotropic Panel

Wavefield data were acquired from Panel A as described in Section 3.1 for characterizing anisotropic wave propagation properties. This data were post-processed using the methods described in Section 3.2 and 3.3. During post-processing, the radial range of each B-scan was restricted from 100 mm in length to 50 mm in length starting at the 20 mm radial coordinate position. This range was chosen empirically to avoid saturated signals close to the transducer location as well as interference from edge-reflected waves.

3.4.1 Estimated Group and Phase Velocity

Figure 6(a) and 6(b) shows estimated phase and group velocities prior to 180° averaging for all incident wave directions along with a corresponding 4-term Fourier fit. The composite panel is nominally homogeneous; however, the estimated velocities do not

agree completely with this assumption, particularly the group velocity. After applying the homogeneity correction discussed in section 3.3.2, the results are shown in Figure 6(c)-(f) on both rectangular and polar formats. It is evident from Figure 6(c) and 6(d) that phase and group velocities are faster along propagation directions of 0°, ±90°, and ±180° and slower along propagation directions ±45° and ±135°. Additionally, the phase velocities follow a more consistent sinusoidal pattern when compared to the group velocities. This makes a Fourier fit better for phase velocity than for group velocity. The primary reason for poorly fitting group velocity is that it is more difficult to precisely identify a peak from a rectified signal than an unrectified one. It must also be noted that the percent difference between maximum and minimum group velocities is only 5.6%. Such small variations in velocity mean that any measured noise in the wavefield data influences the estimation of group velocity more strongly than phase velocity due to the nature of the Radon panel and thus producing the poorer fitting results. This small variation in the both phase and group velocity indicates that this quasi-isotropic panel has little variation in wave propagation in any specific direction. This lack of variation is shown more clearly by Figure 6(e) and 6(f) as the velocity patterns are close to circular.

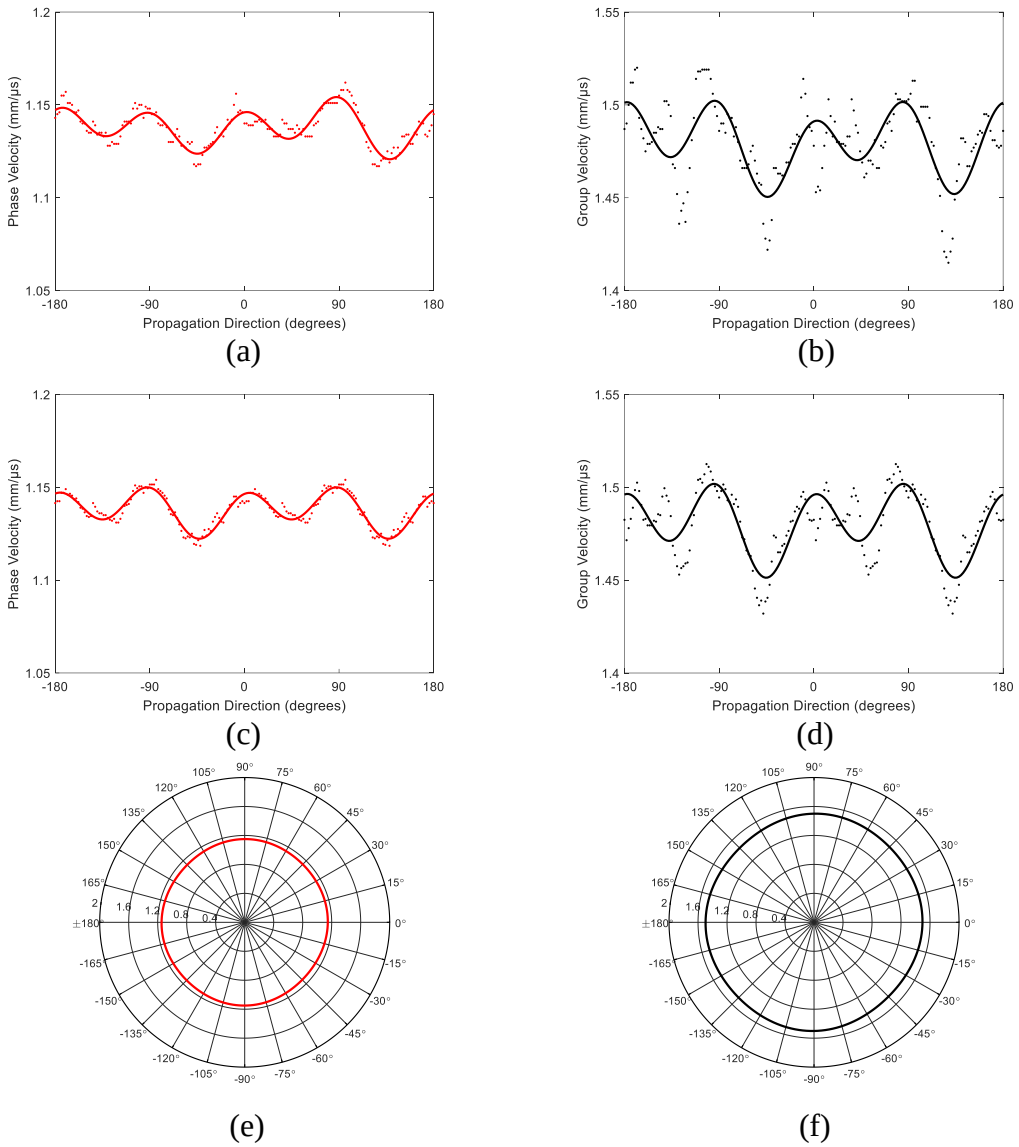

Figure 6 – (a) Phase and (b) group velocities as estimated by the Radon panels. (c) Phase and (d) group velocities after averaging to force symmetry. Polar plots of fitted (e) phase and (f) group velocities.

3.4.2 Estimated Attenuation

Figure 7 shows a comparison of the peak raw amplitudes at 45 mm away from the source before and after enforcing the expected 180° symmetry from the panel fiber layup. Amplitude attenuation was estimated using both a simplistic cylindrical wave spreading model and one that included exponential decay to correct for additional material losses. A

comparison between the two models is shown in Figure 8 for three incident wave directions. Similar to wave velocity, amplitude attenuation for this panel is not a strong function of the propagation direction. The variation of amplitude shown in Figure 7(b) after enforcing homogeneity has no specific pattern and is fairly uniform for all propagation directions. An outlier in Figure 7(a) at approximately -135° can also be seen twice in Figure 7(b) at -135° and +45° due to the averaging 180° apart. This outlier is undoubtedly a result of signal noise during wavefield measurements. Figure 8 shows slight improvement of fitting data after accounting for unknown material losses. Note that the vertical amplitude scale does not begin at zero to better visualize the raw and fitted data. A polar map of the exponentially fitted data is shown in Figure 9 after cubic interpolation in angle. It can be readily visualized that amplitude attenuation is almost uniform in all wave propagation directions.

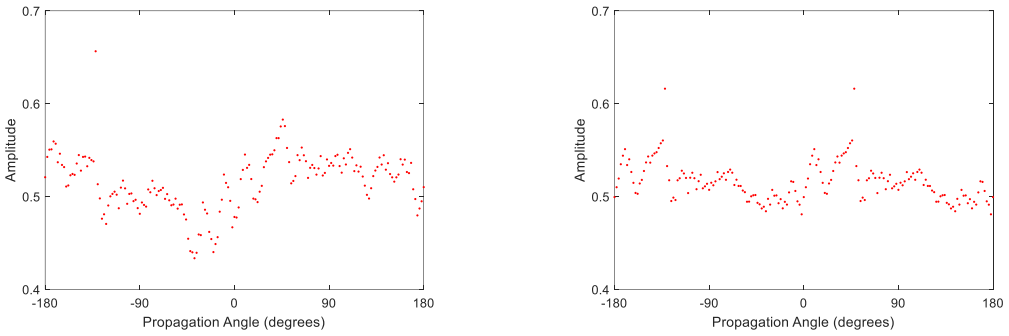

(a) (b)

Figure 7 – Peak amplitudes at 45 mm from the source as a function of propagation angle. (a) Raw data points, and (b) after averaging to force symmetry.

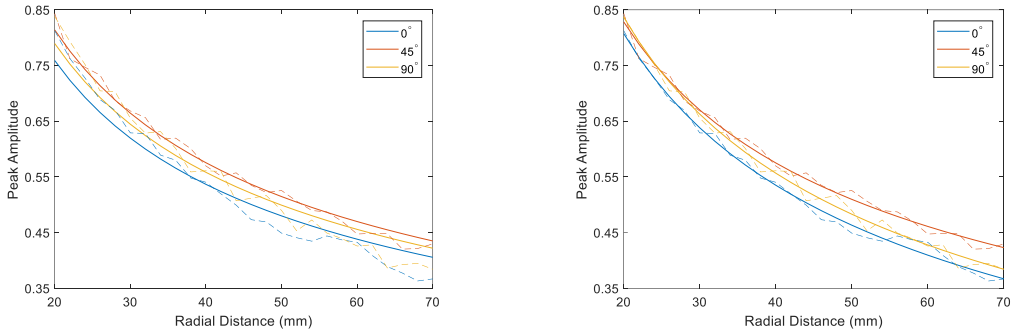

Figure 8 – Raw (dashed lines) and fitted (solid lines) peak amplitude as a function of radial distance for propagation directions of 0°, +45°, and +90°. (a) Fit based upon cylindrical spreading only, and (b) fit including an exponential decay term.

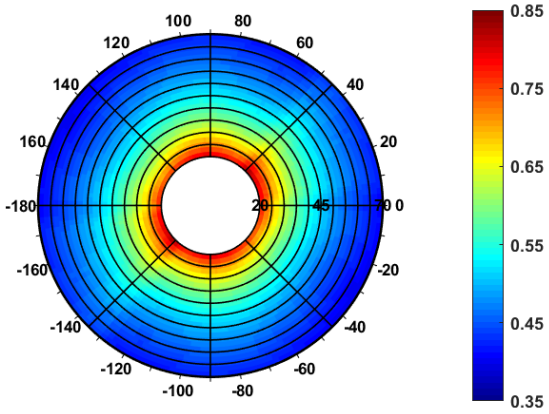

Figure 9 – Polar presentation of exponentially fitted amplitude data.

3.5 Panel C: Orthotropic Panel

3.5.1 Experimental Procedures

Experimental data were obtained from an orthotropic panel known to be of high quality. The obtained data were processed using the same methods described in Sections 3.2 and 3.3. The parameters used during post-processing were kept the same to maintain consistency between obtained results and to show robustness of the presented methods.

3.5.1.1 Panel Description

Data were acquired from an orthotropic panel to serve as a comparison to the data obtained from quasi-isotropic panels mentioned in Section 3.1.1. This 8-layer 470 mm × 470 mm × 2.5 mm composite panel with a fiber orientation layup described by $[0/90]_4$, symmetric about its center, was provided by Tencate [94] and is similar to the panel used by Hall in previous experimental work [84]. The panel is smooth on both sides with a semi-gloss finish and is a high-grade, aerospace-quality composite. The panel was used for both characterizing wave propagation and scattering from defects; it is referred to as Panel C throughout the rest of this study.

3.5.1.2 Laser Vibrometer Measurements

Wavefield data were recorded in the same manner as Panel A where an identical 300 kHz radially polarized transducer was permanently attached to the center of Panel C. All parameters of the radial fan scan and experimental procedures were identical between Panel A and Panel C, except for amplifying the LDV received signals by 18 dB instead of 3 dB for Panel A.

3.5.2 Estimation Results

After applying the methodologies described in Section 3.2 and 3.3, the estimated results for characterizing anisotropy of Panel C are shown in Figure 10 to Figure 13. The post processing parameters used for Panel A were maintained the same here for Panel C. Figure 10(a) and 10(b) show the estimated group and phase velocities along with their respective 4-term Fourier fits. As for Panel C, the group velocities are more scattered and have a less

consistent sinusoidal pattern when compared to the phase velocities. Enforcing homogeneity somewhat reduces these variations. The peak propagation velocities are along the 0° and ±180° directions with smaller peaks at ±90°. Figure 10(e) indicates minimal angular variation in group velocity while Figure 10(f) shows clear dominance along the 0°, ±90°, and ±180° directions for phase velocity.

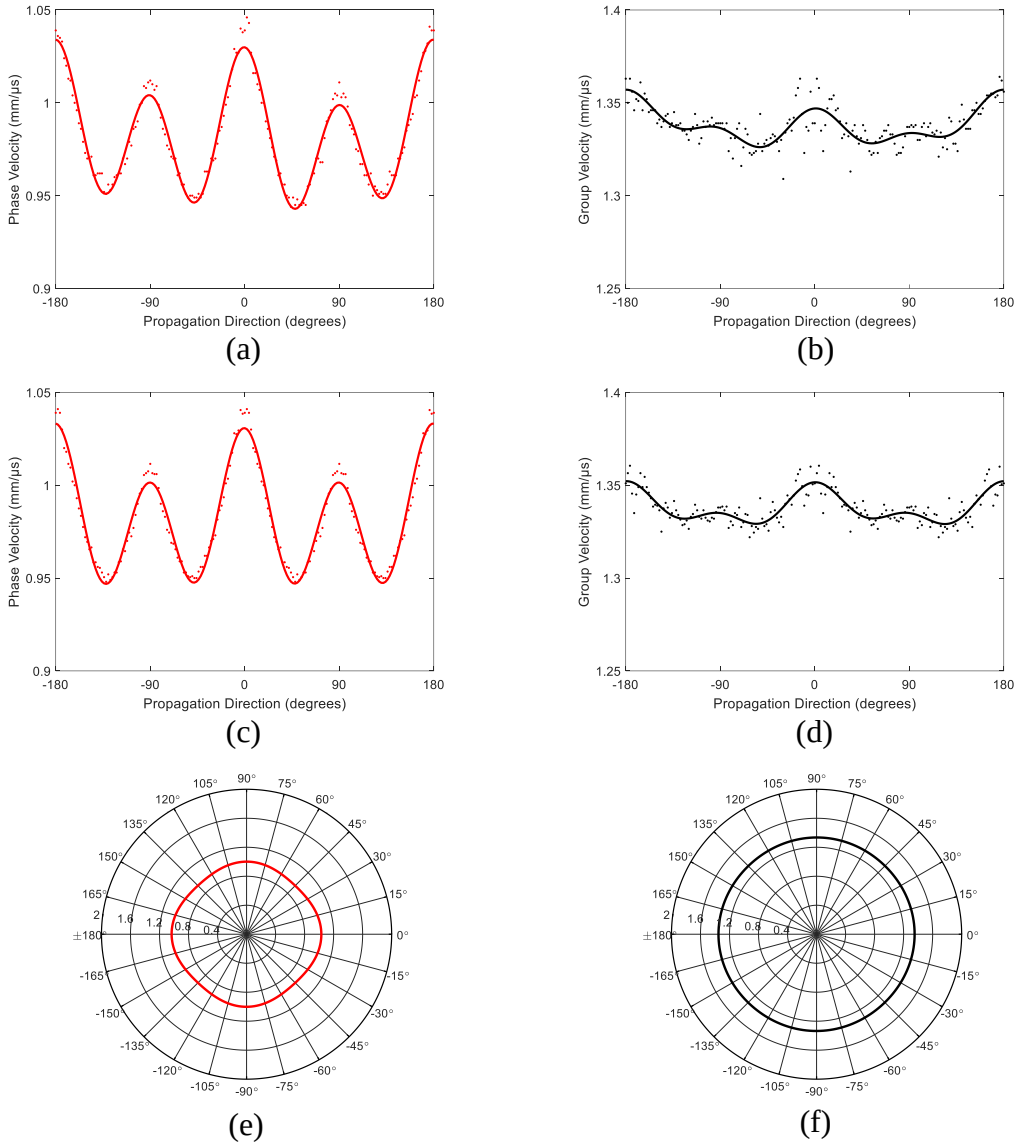

Figure 10 – (a) Phase and (b) group velocities as estimated by the Radon panels with Fourier fits. (c) Phase and (d) group velocities after averaging to force symmetry with Fourier fits. Polar plots of Fourier fitted (e) phase and (f) group velocities.

Figure 11 shows the peak amplitude of the propagating wave in all directions at a radial distance of 45 mm away from the source. Figure 11(a) shows peaks along the dominant fiber directions and has some systematic inhomogeneity producing an underlying curve centered at 0° to all sampled values. After forcing expected homogeneity, Figure 11(b) shows more symmetrical results. To visualize the attenuation as a function of angle, Figure 12 displays the amplitude attenuation over a 50 mm radial length at 0°, 45° and 90°. Figure 12(a) illustrates the cylindrical spreading model applied to the data where Figure 12(b) includes additional material loss compensation. Accounting for material loss improved the fit along the 45° direction; however, no additional losses could be accounted for at 0° and 180°. Amplitude loss was less than typical cylindrical spreading for those two directions, which could be a result of energy being channeled along the composite fibers. Figure 13, which was interpolated from the data in the same manner as Figure 9, helps visualize the amplitude attenuation dominance along fiber directions.

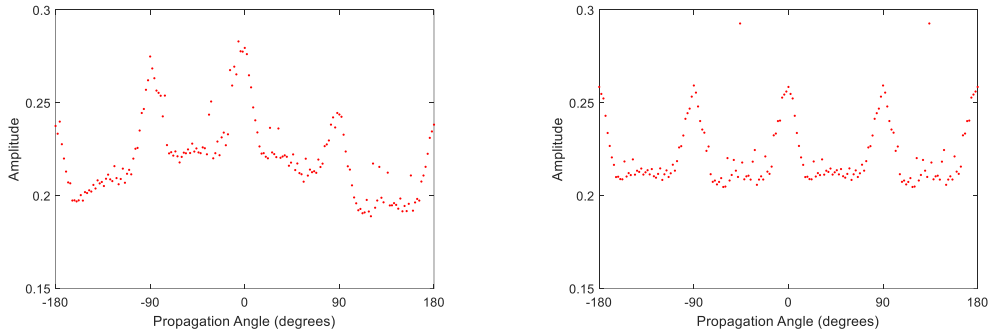

(a) (b)

Figure 11 – Peak amplitudes at 45 mm from the source as a function of propagation angle. (a) Raw data points, and (b) after averaging to force symmetry.

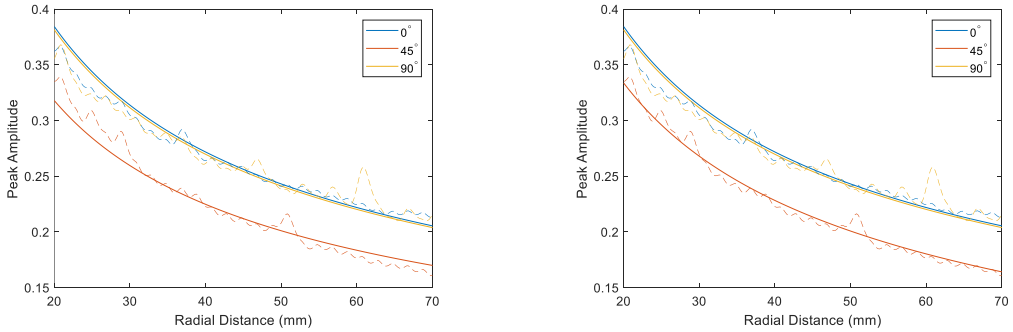

Figure 12 – Raw (dashed lines) and fitted (solid lines) peak amplitude as a function of radial distance for propagation directions of 0°, +45°, and +90°. (a) Fit based upon cylindrical spreading only, and (b) fit including an exponential decay term.

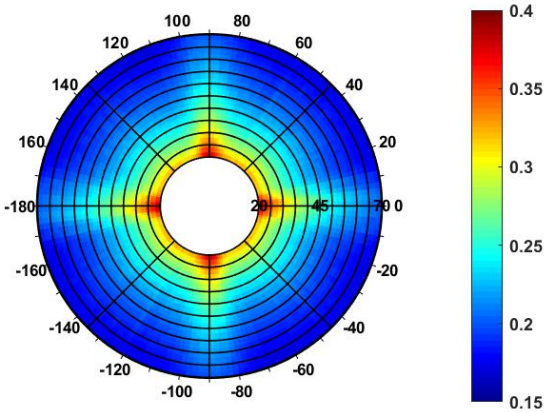

Figure 13 – Polar presentation of exponentially fitted amplitude data.

3.6 Summary

This chapter presented a straight forward approach to estimating angular dependent wave velocity and amplitude attenuation. However, instead of characterizing wave propagation for one or more single frequencies, the propagation of a guided wave packet with a defined center frequency was characterized from data obtained by an LDV system. The experiment was performed for two separate composite panels, one quasi-isotropic and the other orthotropic, to analyze differences in wave propagation for different fiber layups.

The estimated group velocity results for Panel A and Panel C were relatively similar as 0° and 90° were the dominating fiber directions. Overall, the velocity variation as a function of angle was relatively small with a percent difference between minimum and maximum group velocity of ~5% for Panel A and ~3% for Panel C was observed. This small variation in group velocity could be considered negligible on affecting arrival time estimates of wave packets made over small propagation distances; however, larger propagation distances can still be significantly affected. Phase velocity exhibited similar small changes of ~3% for Panel A while Panel C had a larger variation of ~9%. Ultimately, the primary distinguishing difference between the two panels was observed from their attenuation. Panel A showed almost no significant bias in any angular direction with close to uniform amplitude attenuation. On the other hand, Panel C showed significant amplitude attenuation away from the main fiber directions of 0° and 90°.

4 HIGH RESOLUTION SCATTERING PATTERN ESTIMATION

The purpose of this chapter is to present a methodology for experimentally estimating high resolution scattering patterns in anisotropic materials using wavefield imagery. The results from these estimates are used to form 2-D scattering matrices. Such matrices are generated for both impact damage and artificial defects.

4.1 Estimation Methodology

The methodology described here uses different signal processing techniques to isolate scattered waves for estimating scattering patterns. This methodology utilizes wavefield baseline subtraction to extract the residual wavefield, which is further processed to reduce noise and separate waves based on their direction of propagation. A model for estimating the propagation time of the scattered waves is used to estimate the scattering patterns from the processed residual wavefield for a specific incident wave direction. Finally, a method for generating a full 2-D scattering matrix given a sparse number of incident wave scattering patterns is presented.

4.1.1 Wavefield Baseline Subtraction

A composite structure can experience changes during its lifecycle that can affect its performance, possibly resulting in premature failure. Techniques such as baseline subtraction help to identify these changes by examining the differences in signals measured before and after the system incurs these changes. This same principal can be applied to wavefield imaging for evaluating signal-wise differences between two separate wavefields taken before and after a flaw is introduced.

To quantify scattering from a known flaw, wavefield baseline scans are acquired from a specimen assumed to be in pristine condition. Flaws are then introduced after removing the specimen from the wavefield scanning system. After remounting and aligning the specimen to minimize the spatial and temporal offsets, subsequent scans are performed. Direct wavefield baseline subtraction reveals the differences between corresponding waveforms,

$$r(x,y,t) = w_C(x,y,t) - w_B(x,y,t), \tag{17}$$

where $w_B(x,y,t)$ is the baseline wavefield, $w_C(x,y,t)$ is the corresponding current wavefield, and $r(x,y,t)$ is the pixel-wise difference between the two waveforms for all signals in the 3-D space-time domain.

4.1.1.1 Wavefield Baseline Subtraction Issues

To isolate the smaller scattered waves generated from the flaw, the larger incident waves must be removed, which is the purpose of baseline subtraction. Poor baseline subtraction performance is usually the result of measurement inconsistencies between baseline and subsequent scans and can cause scattering to be obscured by remaining incident waves. For the work presented in this thesis, the two main factors affecting subtraction performance are spatial misalignment and optical diffraction of the LDV caused by surface roughness of the specimen.

Spatial misalignment introduced by repositioning the specimen between scans is the primary cause of poor wavefield registration. While this effect is caused by a simple translation and/or rotation, the time-dependency of wavefield imaging introduces the possibility for temporal misalignment as well. This means that all three dimensions of the

wavefield (two spatial dimensions and time) are affected. Although the specimen is carefully repositioned on the scanning system to minimize any alignment issues, residual misalignment errors remain and must be compensated during post-processing to improve overall wavefield subtraction performance.

The other factor affecting image quality is pixel specific because of optical reflectivity issues encountered using an LDV. The specimen used has a polished, smooth finish; however, the polished coating is a transparent layer leaving the fibrous weave of the composite visibly exposed. Diffraction by the specimen's fibers affect the noise levels of the measured signals, producing poor signal quality randomly throughout the wavefield image. Reflective tape is applied on the panel's surface to minimize this effect, and additional steps to remove unwanted noise are performed during post-processing.

4.1.1.2 Global Space-Time Alignment Methodology

Global space-time alignment or GSTA is a wavefield image registration method that applies subpixel shifts to the baseline wavefield for optimal registration with the current wavefield [95]. Here, optimal is defined by minimizing the L_2 norm of the residual wavefield with respect to $(\Delta x, \Delta y, \Delta t)$, which are the applied shifts in the space-time domain prior to differencing the wavefields:

$$(\Delta x_0, \Delta y_0, \Delta t_0) = \underset{\Delta x, \Delta y, \Delta t}{\arg\min} \| W_C(k_x, k_y, \omega) - W_B(k_x, k_y, \omega) e^{-i(k_x \Delta x + k_y \Delta y + \omega \Delta t)} \| . \qquad (18)$$

W_B and W_C represent the baseline and current wavefield data, respectively, after transforming the data into the wavenumber-frequency domain using the 3-D Fourier transform. By performing the minimization in the wavenumber-frequency domain,

subpixel shifts can be obtained which would otherwise be too computationally intensive in the space-time domain. The optimal shifts are denoted by $(\Delta x_0, \Delta y_0, \Delta t_0)$, which minimizes the residual wavefield energy. The residual wavefield in the wavenumber-frequency domain is calculated as,

$$R(k_x, k_y, \omega) = W_C(k_x, k_y, \omega) - W_B(k_x, k_y, \omega) e^{-i(k_x \Delta x_0 + k_y \Delta y_0 + \omega \Delta t_0)}. \quad (19)$$

The optimal shifts are applied to the wavenumber-frequency baseline data, which are converted back to space and time through the inverse Fourier transform, and then differenced with the current wavefield for maximum removal of incident waves in the residual wavefield data.

Since alignment between baseline and current wavefield data is achieved though energy minimization in the wavenumber-frequency domain, the change in energy caused by the scattered waves in the current wavefield data will affect how well the optimal shifts are determined. To further improve spatial alignment, GSTA is applied to only a time windowed section of the wavefield data. This time window is applied to include only the incident waves prior to contacting the flaw, meaning that the baseline and current wavefield data should be nominally identical. After application of the time-windowed GSTA, the estimated spatial and temporal shifts are then applied back to the complete baseline wavefield for global alignment. Figure 14 illustrates how time-windowing around the incident waves produces better alignment between baseline and current wavefield for improved isolation of scattered waves.

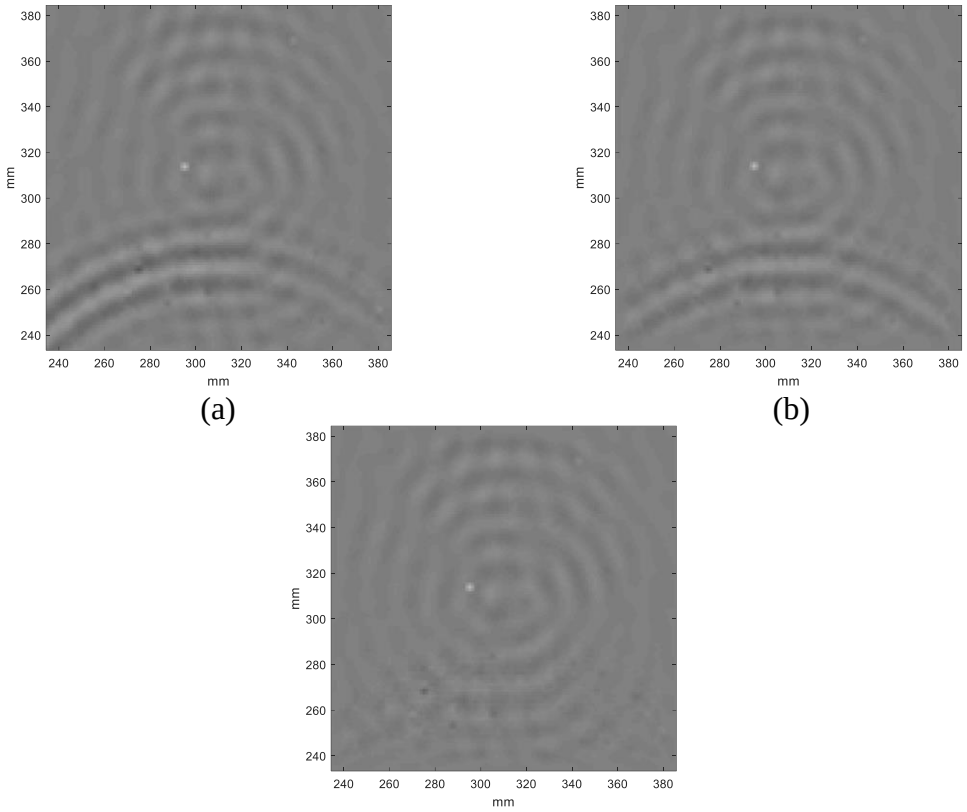

Figure 14 – Example of a residual wavefield "snapshot" after baseline subtraction. (a) No GSTA, (b) GSTA applied to full wavefield, and (c) GSTA applied to time-windowed wavefield.

4.1.2 Wavenumber-Frequency Domain Filtering

The filtering techniques used here on the acquired wavefield data are performed in the 3-D Fourier domain. The data are transformed from the space-time domain (x, y, t) to the wavenumber-frequency domain (k_x, k_y, ω) via the 3-D fast Fourier transform (FFT),

$$W(k_x, k_y, \omega) = \iiint \omega(x, y, t) e^{-j(k_x x + k_y y + \omega t)} \mathrm{d}x\mathrm{d}y\mathrm{d}t \,, \tag{20}$$

where ω is the angular frequency, and k_x and k_y are the wavenumber components along the x and y axes. Operating in the wavenumber-frequency domain allows for additional manipulation of the data to extract features and further isolate scattered waves more

effectively than in the space-time domain. The techniques used here are phase velocity filtering, which has the capability for noise removal, and directional wavenumber filtering, which can separate waves based on their propagation direction. Phase velocity filtering was applied to guided wavefields by Tian and Yu [96] to separate the A_0 and S_0 Lamb wave modes for individual processing, and by Flynn *et al*. [97] to separate guided wave modes based on dispersion curves. Ruzzene [98] used directional wavenumber filtering to separate backscattered waves from forward incident waves based on their opposing propagation directions to enhance guided wave imaging.

4.1.2.1 Phase Velocity Filtering

As previously described, chrome automotive tape was applied during each wavefield scan of Panel B to improve optical reflectivity of the composite panel's surface. This tape does improve overall reflectivity for the LDV, but random noise is still present. Phase velocity filtering is applied in the 3-D Fourier domain to help reduce noise artifacts and improve overall image clarity by removing information that does not correspond to the guided wave mode of interest.

After baseline subtraction, the residual wavefield data are transformed to the wavenumber-frequency domain. A 3-D wavenumber-frequency filter, developed using a specific range of phase velocities, is applied in the Fourier domain to retain only the guided wave components corresponding to those phase velocities. The wavenumber equation,

$$k_r = \frac{\omega}{c_p}, \tag{21}$$

defines the relation among radial wavenumber k_r, frequency ω, and phase velocity c_p. At each frequency, there is a corresponding range of radial wavenumbers with inner and outer radial bounds. The bounds are defined by upper and lower phase velocity limits that form a ring-like filter. The process of filtering a single frequency is illustrated in Figure 15 where a frequency slice at $\omega = 80$ kHz is multiplied by a wavenumber-frequency filter.

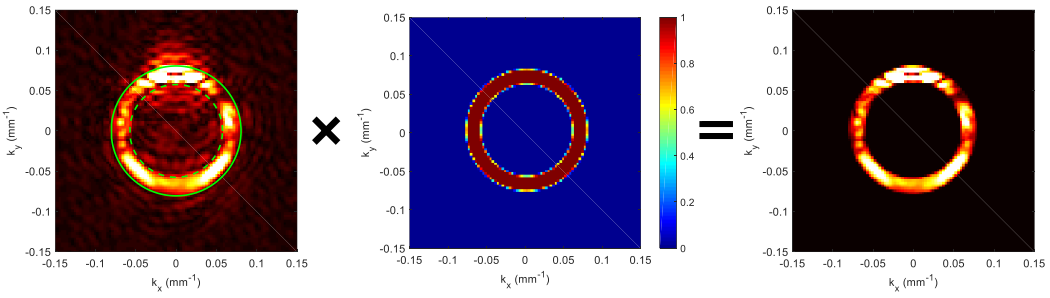

(a) (b) (c)

Figure 15 – Illustration of the phase velocity filtering process. (a) A wavenumber slice at 80 kHz, (b) the radial wavenumber-frequency filter for 80 kHz, and (c) post-filtered 80 kHz wavenumber slice.

Using Equation (21), the radial wavenumber range of 0.0571 to 0.08 mm^{-1} is determined from the corresponding phase velocity range of 1.0 to 1.4 mm/μs, which is chosen to prevent the removal of important energy content near $\omega = 80$ kHz. Tukey-windowed radial edges are applied to the filter for minimizing spectral leakage. Similar steps are done to filter each discrete frequency slice in the wavenumber-frequency domain. The filtered wavefield is then transformed back to the space-time domain via the inverse 3-D Fourier transform.

4.1.2.2 Directional Wavenumber Filtering

Directional filtering is a technique used to separate waves based on their direction of propagation within the captured wavefield. This method is well-described by Ruzzene [98] where he derives the methodology and utilizes it for analyzing wavefield imaging

data from an aluminum plate to detect backscattering from simulated cracks obscured by incident waves. That same principal applies here where the back scattering from flaws can still be obscured by incident waves even after wavefield baseline subtraction is applied. Unresolved wavefield baseline subtraction errors can allow residual incident wave feed-through to remain, which is caused by amplitude mismatch or phase misalignment of the two wavefields and can obscure the scattered waves of interest. However, the incident waves propagate in the opposite direction as the back scattered waves. This difference in propagation direction allows for separation and removal of these incident waves by filtering in the wavenumber-frequency domain.

The wave propagation direction is defined such that 0° corresponds to the +*x* axis. The relation between wavenumber and propagation angle is given by,

$$\theta_p = \operatorname{atan}2(k_y, k_x) = \begin{cases} \arctan\left(\frac{k_y}{k_x}\right) & \text{if } k_x > 0, \\ \arctan\left(\frac{k_y}{k_x}\right) + \pi & \text{if } k_x < 0 \text{ and } k_y \geq 0, \\ \arctan\left(\frac{k_y}{k_x}\right) - \pi & \text{if } k_x < 0 \text{ and } k_y < 0, \\ +\frac{\pi}{2} & \text{if } k_x = 0 \text{ and } k_y > 0, \\ -\frac{\pi}{2} & \text{if } k_x = 0 \text{ and } k_y < 0, \\ \textit{undefined} & \text{if } k_x = 0 \text{ and } k_y = 0. \end{cases}, \tag{22}$$

where θ_p is the wave propagation angle in the space-time domain and k_x and k_y are the components of $\bar{k}$ in the wavenumber-frequency domain. This relation allows us to filter a span of wavenumbers in the Fourier domain based on a defined range of wave propagation angles in the space-time domain. In Figure 16(b), a wavenumber filter is

shown spanning all $+k_x$ values, which corresponds to wave propagation angles from -90° to +90°. Filters can also be created to include (or exclude) other propagation angle ranges as shown in Figure 16(c). A 10% Tukey window is applied along the edges of the filter to minimize spectral artifacts when transforming back to the space-time domain. Each discrete frequency slice of the 3-D Fourier data is multiplied by the wavenumber filter to retain only the waves corresponding to the propagation directions related to the filter. The inverse FFT is applied to the data to transform it back to space and time for visualization and additional analysis.

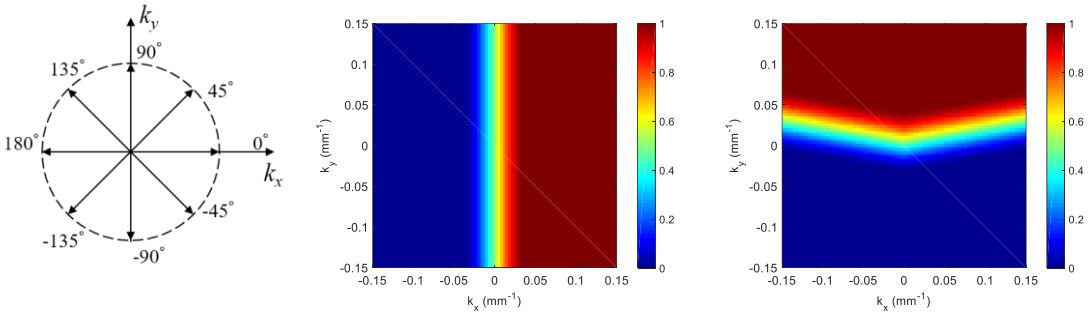

(a) (b) (c)

Figure 16 – (a) Wave propagation direction related to directional wavenumber. Wavenumber filters retaining waves propagating from (b) -90° to +90°, and (c) +10° to +170°.

4.1.3 Scattering Pattern Estimation

The scattered waves caused by interactions between waves incident on artificial and real impact damage can be estimated in the space-time domain after applying both GTSA baseline subtraction to full wavefield data and post-filtering techniques discussed in sections 4.1.1 and 4.1.2, respectively. However, the filtered full residual wavefield consisting of 3-D space-time data must be remapped to 2-D angle-time data to directly acquire a scattering pattern. This mapping is achieved through bilinear interpolation of points in space from a 3-D wavefield to a specified angle and radius with respect to the

flaw location. This mapping from (x,y,t) to (r,θ,t) for a specific radius r is referred here as a circular wavefield B-scan. An example can be seen in Figure 17 where the circular wavefield was interpolated from residual wavefield data acquired from Panel B with magnet stacks used as artificial damage. The interpolated circular wavefield has an angular increment of 1° and a radius of 35 mm. The scattered wave packet from an incident wave at 45°can readily be seen around 150 μs where the peak amplitudes in the B-scan correspond to shadowing by the defect (forward scattering). Back-scattered waves can be visualized around -135° which have lower amplitudes when compared to the forward scattered waves at 45°.

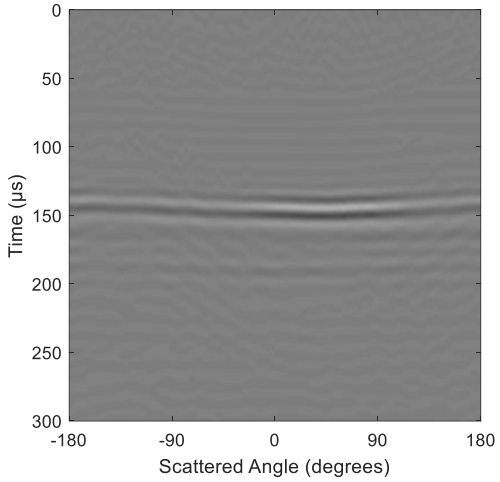

Figure 17 – Interpolated circular wavefield represented as a circular B-scan.

To accurately estimate arrival times of the scattered wave packets, a scattering model based on a circular flaw geometry is assumed. In the case here, the geometry of a flaw is approximated as a circular disc with a specified radius. This approximation assumes that incident rays contacting the circular edge of the flaw result in specular reflection.

A diagram of the ray tracing model for a single ray is shown in Figure 18(a). A transmitter located at (x_t,y_t) sends a ray, $\vec{t}$, to a reflection point located at (x_i,y_i). The

damage center location, (x_d,y_d), and its radius, r_d, are known as well as the receiver location (x_r,y_r); $\vec{r}$ is the scattered ray. Given the assumption of a specular reflection where $\theta_1 = \theta_2$, the reflection point (x_i,y_i) can be solved using two equations and two unknowns. The first equation defines the geometric shape of the flaw, in this case a circle,

$$r_d^{\,2} = (x_i - x_d)^2 + (y_i - y_d)^2, \tag{23}$$

which restricts the reflection point to any location a distance r_d away from the damage center. To help understand the second equation given by the specular reflection constraint, a simplified version of the ray tracing diagram is shown in Figure 18(c), where γ_1 and γ_2 are the inclusive angles between the Euclidean vectors $\vec{t}$ and $\vec{d}$ as well as $\vec{r}$ and $\vec{d}$; $\vec{d}$ is the vector defined from the damage center location to the reflection point. These vectors and their inclusive angles are related by,

$$\vec{t} \cdot \vec{d} = \left\|\vec{t}\right\| \left\|\vec{d}\right\| \cos(\gamma_1), \tag{24}$$

and,

$$\vec{r} \cdot \vec{d} = \left\|\vec{r}\right\| \left\|\vec{d}\right\| \cos(\gamma_2). \tag{25}$$

Requiring that $\theta_1 = \theta_2$ for a specular reflection also implies that $\gamma_1 = \gamma_2$. Using this relation, Equations (24) and (25) can be rearranged and equated,

$$\frac{\vec{t} \cdot \vec{d}}{\left\|\vec{t}\right\|} = \frac{\vec{r} \cdot \vec{d}}{\left\|\vec{r}\right\|}. \tag{26}$$

The final equation can be written more explicitly in terms of coordinate values as,

$$\frac{(x_i - x_t)(x_i - x_d) + (y_i - y_t)(y_i - y_d)}{\sqrt{(x_i - x_t)^2 + (y_i - y_t)^2}} = \frac{(x_i - x_r)(x_i - x_d) + (y_i - y_r)(y_i - y_d)}{\sqrt{(x_i - x_r)^2 + (y_i - y_r)^2}}, \tag{27}$$

where x_i and y_i are the coordinates of the reflection point, x_d and y_d are the coordinates of the damage center, x_t and y_t are the coordinates of the transmitter center, and x_r and y_r are the coordinates for the receiver center.

Because of the quadratic nature of both equations, an analytical solution is not feasible; however, utilizing the MATLAB™ Math Toolbox, the function 'solve' [99] can be used to solve up to 4th degree polynomials, which is the polynomial degree for this case. Up to four pairs of possible solutions are returned given the other known parameters. One solution pair corresponds to the desired reflection point on the near-side of the constraint circle, another pair corresponds to the reflection point on the far-side of the constraint circle, and the other two pairs are spurious solutions. For the usual case when $\vec{t}$ and $\vec{r}$ are not coincident, the spurious solutions have imaginary components and are easily recognized and discarded. If $\vec{t}$ and $\vec{r}$ are coincident (i.e., the transmitter and receiver are in line with the center of the circle), the spurious solutions are real but repeated; the unique solutions can be readily identified. The desired near-side reflection point is chosen by selecting the solution with the shortest incident ray length. In addition, for receiver points that are located behind the damage edge relative to the transmitter location, a single direct ray from the transmitter to receiver is assumed as shown in Figure 18(b) (i.e., the waves travel through the damage along a straight line).

Arrival times of the scattered wave packet are calculated using angle-dependent group velocities for each path of the incident and scattered waves. The nominal arrival times, t_{arr}, are calculated from the ray path lengths from transmitter-to-scatterer and scatterer-to-receiver, D_{ts} and D_{sr}; the point (x_i,y_i) is the scatterer location. The incident and scattered angles, θ_{inc} and θ_{scat}, are obtained from the ray tracing model. The group velocity profile,

$c_g(\theta)$, is used to calculate the nominal arrival times as a function of the incident and scattered angles,

$$t_{arr}(\theta_{inc},\theta_{scat}) = \frac{D_{ts}}{c_g(\theta_{inc})} + \frac{D_{sr}}{c_g(\theta_{scat})} + \frac{N_c}{2 f_o} + t_{off}\,, \tag{28}$$

where N_c and f_o are the number of cycles and frequency, respectively, of the tone burst excitation, and t_{off} is a calibrated time offset associated with the real-time excitation of the transducer. Raw scattering patterns are obtained by first applying the Hilbert transform to obtain the envelopes of the scattered signals, then calculating the nominal arrival times as a function of angle using Equation (28), and finally extracting the scattered amplitude values from the envelope signals at the calculated arrival times. The result is a scattering pattern, $S(\theta)$.

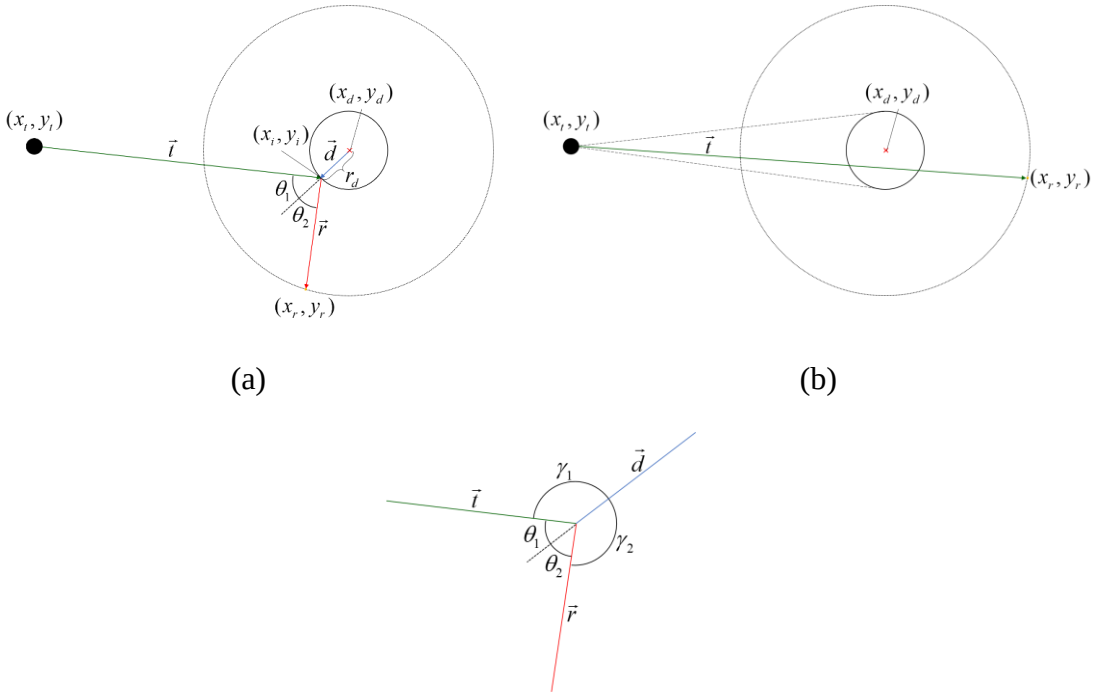

Figure 18 – (a) Ray tracing diagram of specular reflection for a single transmitted and reflected ray, (b) ray tracing diagram for receiver locations located behind the scatterer and, (c) a simplified diagram of specular reflection at a single point.

4.1.4 2-D Scattering Matrix Estimation

A scattering pattern $S(\theta)$ represents scattering amplitudes for all scattering directions given a specific incident wave direction. For non-axisymmetric scatterers and anisotropic materials, the angular-dependent scattering amplitudes are also dependent upon the incident wave direction. An appropriate way to represent scattering as a function of incident and scattered angles is through a 2-D scattering matrix. This matrix is composed of scattered signal amplitudes from a flaw indexed by incident and scattered angles spanning ±180° and is defined here as an $N \times N$ matrix,

$$A(\theta_{inc}, \theta_{scat}) = [s_{-180} \quad s_{-180+\Delta\theta} \quad s_{-180+2\Delta\theta} \quad \cdots \quad s_{-180+(N-1)\Delta\theta}], \tag{29}$$

where each column is a scattering pattern for a specific incident angle θ_{inc},

$$s_{\theta_{inc}}(\theta_{scat}) = \begin{bmatrix} a_{-180} \\ a_{-180+\Delta\theta} \\ a_{-180+2\Delta\theta} \\ \vdots \\ a_{-180+(N-1)\Delta\theta} \end{bmatrix}. \tag{30}$$

The angular resolution of the incident and scattered angles $\Delta\theta$ is such that the N numbers of amplitude values are equally spaced; that is,

$$N \cdot \Delta\theta = 360. \tag{31}$$

The estimated scattering patterns for a flaw obtained at different incident angles are used to populate individual columns in the 2-D scattering matrix. The size of the matrix is dependent on the angular resolution of the scattering patterns and, while high resolution scattering patterns can be acquired from the data, the number of incident directions is limited by the number of attached transducers and wavefield datasets acquired. Due to

high scan times, there are relatively few incident wave directions, resulting in a sparsely populated matrix. However, this sparsity can be overcome by interpolating columns of the 2-D scattering matrix.

Interpolation is done by first aligning the scattering patterns of all populated incident wave directions to 0° via circular shifting of each column. If n_0 is the index corresponding to an incident angle of 0°, then a circular shift,

$$s(n) = n_0 - n\,, \tag{32}$$

is applied to the n^{th} column.

Once aligned, an 8-term Fourier series is fit to each column using least squares. The Fourier series is defined by,

$$f(\theta_{scat}) = \sum_{k=0}^{8} a_k \cos(k\theta_{scat}) + b_k \sin(k\theta_{scat})\,, \tag{33}$$

where $f(\theta_{scat})$ is the fitted curve and a_k and b_k are the Fourier coefficients. These 17 coefficients then form a column vector for each incident direction,

$$c_{\theta_{inc}} = \begin{bmatrix} a_0 \\ a_1 \\ b_1 \\ a_2 \\ b_2 \\ \vdots \\ a_8 \\ b_8 \end{bmatrix}. \tag{34}$$

These columns sparsely populate a separate 17×*N* coefficient matrix,

$$C = [c_{-180} \quad c_{-180+\Delta\theta} \quad c_{-180+2\Delta\theta} \quad \cdots \quad c_{-180+(N-1)\Delta\theta}]. \tag{35}$$

1D linear interpolation is applied across each row of Fourier coefficients to fully populate the matrix. Each column of $A(\theta_{inc},\theta_{scat})$ is reconstructed from the interpolated Fourier coefficients and circularly shifted back to its proper incident direction,

$$s(n) = n - n_0 . \tag{36}$$

Reciprocity between source and receiver is used to generate an additional matrix with scattering amplitudes corresponding to the reciprocal incident and scattering angles (i.e., the source and receiver are flipped). The reciprocal angles are defined by,

$$\tilde{\theta}_{inc} = \begin{cases} \theta_{scat} + 180°, & \theta_{scat} < 0° \\ \theta_{scat} - 180°, & \theta_{scat} \geq 0° \end{cases}, \tag{37}$$

and,

$$\tilde{\theta}_{scat} = \begin{cases} \theta_{inc} + 180°, & \theta_{inc} < 0° \\ \theta_{inc} - 180°, & \theta_{inc} \geq 0° \end{cases}, \tag{38}$$

and the reciprocal matrix is created by remapping the original scattering matrix,

$$\tilde{A}(\tilde{\theta}_{inc},\tilde{\theta}_{scat}) = A(\theta_{inc},\theta_{scat}) . \tag{39}$$

To produce the final matrix, the two matrices are averaged,

$$\overline{A} = \frac{(A + \tilde{A})}{2}, \tag{40}$$

where the averaging process reduces artifacts caused by linear interpolation of the Fourier coefficients. The final scattering matrix is $\overline{A}$.

4.2 Panel B: Quasi-Isotropic Panel

A series of experiments was conducted to characterize scattering from artificial and real impact damage using a quasi-isotropic composite panel referred to as Panel B. The

experimental setup is described here, and the acquired data are processed according to the methodologies described in section 4.1.

4.2.1 Panel Description

As described in section 3.1.1, two composite panels were purchased from Allred and Associates, Inc. [85]. The smaller panel (Panel A) was used to characterize anisotropic wave propagation properties of the material while the larger panel (Panel B), 619 mm × 619 mm × 3 mm (part number FDPLSC04G2424), was used to estimate scattering from damage. Panel B had the same surface finish as Panel A where one side was smooth and polished and the other had exposed fiber weave with a coarse texture. They both had a nominally identical quasi-isotropic fiber layup so that the characterization results of Panel A could be applied to Panel B. Panel B was used for a series of experiments where wavefield data were acquired to estimate scattering from both artificial and real impact damage. The larger panel size also allowed for longer wave propagation distances without interference from edge reflections, which was useful for making wavefield measurements within a radial array of transducers.

Panel B was instrumented with a sparse array of eight transducers, the same type as described in Section 3.1.2, permanently attached using 5-minute clear epoxy. The surface of the panel was prepped prior to bonding by sanding the contact surface to ensure proper adhesion of the epoxy. The transducers were arranged in a circular pattern with a radius of 150 mm and equally spaced around the damage location as shown in Figure 19 to evaluate scattering from incident waves along the main fiber directions.

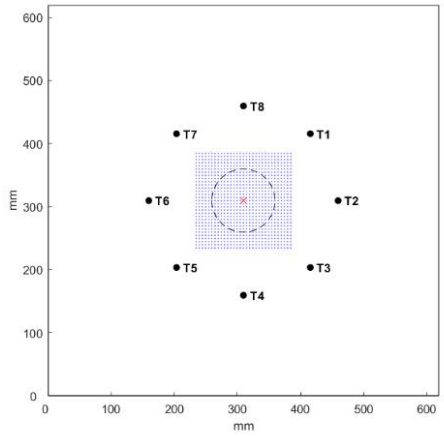

Figure 19 – Diagram of Panel B indicating the transducer locations (small solid circles), the circular wavefield measurement path (black dashed line), the full wavefield measurement path (blue dashed lines), and the applied damage location (red "x").

4.2.2 Laser Vibrometer Measurements

Wavefield data were recorded in both circular and rectilinear grid patterns. The circular pattern data were acquired at a radius of 50 mm and an angular resolution of 1° as shown in Figure 19 while the rectilinear grid data were acquired in a grid measuring 150 mm in both the *x*- and *y*-directions and with a 2.5 mm spatial increment. Both patterns were centered about the applied damage location.

Measurements were conducted using the same equipment setup described in section 3.1.2 where the same linear sine wave chirp excitation from 40 to 150 kHz was used. Additionally, all wavefield data were down-sampled from 20 MHz to 2.5 MHz and were deconvolved to a 3-cycle, 80 kHz tone burst equivalent excitation before post-processing. The signals obtained during circular wavefield measurements were amplified by 12 dB while the rectilinear grid data were amplified by 5 dB to prevent saturation of signals recorded close to the source transducer. The filtering and digitization parameters used for Panel B data matched those used for acquiring Panel A data.

The 80 kHz center frequency of the wave packet was chosen because it provided the best tradeoff between resolution and attenuation. The dominant wavelength of the wave packet is given by,

$$\lambda = \frac{c_p}{f_o}, \tag{41}$$

where f_o is the center frequency of the wave packet (80 kHz), and c_p is the phase velocity at that frequency. The maximum measured phase velocity for the wave packet in Panel B was 1.16 mm/μs at an angle of 96°, which corresponds to a maximum wavelength of 14.5 mm at the center frequency of 80 kHz.

4.2.2.1 Artificial Damage

Artificial damage of various types was applied to Panel B to estimate scattering prior to impacting the panel. These experiments were an attempt to find a suitable candidate for an artificial scatterer that would provide similar scattering characteristics to real impact damage. By using artificial damage, multiple flaws at multiple locations can be tested without permanently damaging the structure or specimen. Three artificial damage types were used. The first was a magnet stack comprised of two 10 mm diameter, 5 mm-thick neodymium rare earth magnets co-located on each side of the panel (four magnets in total). A magnet stack was chosen because of its common use in other studies and its closer approximation to a point-like scatterer. The second was a 20 mm diameter, 2 mm-thick aluminum disc adhered to the transducer side of Panel B using a 5-minute clear epoxy. This added mass was considered because its dimensions were similar to impact damage (i.e., not point-like). The third was a copper tube with 12.7 mm height, an inner diameter of 15.9 mm, and an outer diameter of 17.8 mm. It was also adhered to the transducer side

using the same epoxy. This copper pipe was chosen as an effort to cause energy trapping such as is exhibited by a typical impact delamination. A minimal amount of epoxy was used to prevent damaging the panel during removal while still properly securing each mass. Each artificial damage type can be seen in Figure 20.

(a) (b) (c)

Figure 20 – Photographs of artificial damage: (a) magnet stack, (b) aluminum disc and (c) copper pipe.

Two series of scans were conducted using Panel B. The first series of scans ("BC" series) consisted of circular wavefield scans that were designed to directly estimate scattering via baseline subtraction, while the second series ("BG" series) consisted of rectilinear grid data that could be additionally post-processed in the wavenumber-frequency domain for noise suppression and wave separation as described in section 4.1.2. The circular scans have the distinct advantage of short acquisition times due to the small number of wavefield sampling points needed when compared to the rectilinear scans; however, the circular configuration of sampling points prevents the use of wavenumber-frequency filtering and requires greater control of environmental conditions during data acquisition to obtain adequate baseline subtraction performance.

Scan series "BCA" is summarized in Table 1 where all circular scans are categorized based on the type of artificial flaw and incident wave direction described by Table 2. These scans were acquired with all eight transducers for all possible incident wave directions.

Series “BGA” scans are listed in Table 3 for all grid pattern scans acquired. These scans were limited to incident directions of 0°, 45°, and 90° because of the long acquisition times for each grid scan. Prior to applying each artificial flaw, baseline datasets were acquired for all incident directions. Applying each flaw required remounting the panel which can introduce misalignment errors relative to when the baseline data were acquired; however, care was taken to help mitigate such effects.

Table 1. Circular wavefield scans of artificial damage from Panel B.

Scan	Flaw	Source	Description
BCA1 – BCA8	---	T1 – T8	Baseline circular wavefield measurements
BCA9 – BCA16	Magnets	T1 – T8	Circular wavefield measurements for estimating scattering from magnet stacks
BCA17 – BCA24	Al Disc	T1 – T8	Circular wavefield measurements for estimating scattering from aluminum disc
BCA25 – BCA32	Cu Pipe	T1 – T8	Circular wavefield measurements for estimating scattering from copper pipe

Table 2. Transducer source number related to incident direction.

Source	Incident Direction Relative to Flaw Location
T1	-135°
T2	-180°/180°
T3	135°
T4	90°
T5	45°
T6	0°
T7	-45°
T8	-90°

Table 3. Rectangular grid wavefield scans of artificial damage from Panel B.

Scan	Flaw	Source	Description
BGA1 – BGA3	---	T4 –T6	Baseline grid wavefield measurements
BGA4 – BGA6	Magnets	T4 –T6	Grid wavefield measurements for estimating scattering from magnet stacks
BGA7 – BGA9	Al Disc	T4 –T6	Grid wavefield measurements for estimating scattering from aluminum disc
BGA10 – BGA12	Cu Pipe	T4 –T6	Grid wavefield measurements for estimating scattering from copper pipe

4.2.2.2 Impact Damage

In addition to acquiring wavefield data from artificial damage, impacts were performed on Panel B to create internal separation of the ply layers. A drop station was constructed from a rigid aluminum frame and a 2.4 m clear guide tube attached to a solid steel base. A drop weight, or impactor, was fit narrowly within the tube and held at various heights above the panel using a manual string release. During each drop a foam pad was placed between the panel and impactor during the impact debounce to prevent further damage from successive bounces. The impactor itself was machined from a low carbon steel rod, with a 25.4 mm diameter, 253 mm length, and 50.8 mm curved radius impact face and weighed 978 g. It also had four symmetric slits down the length of its body to allow air flow around it during a drop. A support backing for the impact location of the panel was 3D printed from ABS plastic in the shape of a circular donut measuring 50 mm in height with an inner diameter of 45 mm and outer diameter of 100 mm. This backing support was mounted to a 305 × 305 × 25.4 mm aluminum plate for stability during impacts.

A series of impacts was carried out from varying heights to induce increasing damage with higher energy impacts. A summary of impacts with calculated energies is presented in Table 4. Calculated values are based upon the total mass of the impactor and the calculated free-fall velocity at the time of the impact. Impacts were applied at the center of the transducer array to simulate growing impact damage; i.e., successive impacts were on top of each other. Wavefield scans were taken after each successive impact to measure scattering for four sizes of delaminations. The same approach for acquiring wavefield data for artificial damage was also performed for impact damage. Scan series “BCI” is

summarized in Table 5 for circular scans while series “BGI” is listed in Table 6 for grid scans.

Table 4. Impact drop heights and calculated impact energies.

Designation (Impact Level)	Drop Height (cm)	Calculated Impact Energy (J)
1	30.5 (12")	2.92
2	35.5 (14")	3.40
3	40.6 (16")	3.89
4	45.7 (18")	4.38

Table 5. Circular wavefield scans of impact damage from Panel B.

Scan	Flaw	Source	Description
BCI1 – BCI8	---	T1 – T8	Baseline circular wavefield measurements
BCI9 – BCI16	Impact 1	T1 – T8	Circular wavefield measurements from impact 1
BCI17 – BCI24	Impact 2	T1 – T8	Circular wavefield measurements from impact 2
BCI25 – BCI32	Impact 3	T1 – T8	Circular wavefield measurements from impact 3
BCI33 – BCI40	Impact 4	T1 – T8	Circular wavefield measurements from impact 4

Table 6. Rectangular grid wavefield scans of impact damage from Panel B.

Scan	Flaw	Source	Description
BGI1 – BGI3	---	T4 –T6	Baseline grid wavefield measurements
BGI4 – BGI6	Impact 1	T4 –T6	Grid wavefield measurements for estimating scattering from impact 1
BGI7 – BGI9	Impact 2	T4 –T6	Grid wavefield measurements for estimating scattering from impact 2
BGI10 – BGI12	Impact 3	T4 –T6	Grid wavefield measurements for estimating scattering from impact 3
BGI13 – BGI15	Impact 4	T4 –T6	Grid wavefield measurements for estimating scattering from impact 4

4.2.3 Estimation Results

Data acquired and used for the analysis in this section corresponds to Panel B. Both Panel A and Panel B are considered nominally identical and the panel anisotropy

characterization from Panel A is used for estimating the scattered amplitude profile of the damage in Panel B.

4.2.3.1 Postprocessing of Full Wavefield Data

GSTA baseline subtraction is performed on all rectilinear wavefield data. Additional 2x spatial upsampling is applied to improve visualization of the data only. A time window from 80 to 100 μs is utilized during GSTA as described in section 4.1. Figure 21 and Figure 22 shows time "snapshots" at 100 μs, 120 μs, 140 μs, and 160 μs of the baseline subtraction performance after applying GSTA to series data BGA and BGI at an incident direction of 90° for an aluminum disc and impact 3.

After applying baseline subtraction, noise and interfering waves are evident in the residual images in Figure 21 and Figure 22; note that the residual images shown are on the same grayscale level as the baseline and current data. It is evident when comparing the current and baseline subtracted residual signals in Figure 21 and Figure 22 that the main forward incident waves have been substantially reduced; however, the remaining amplitude of incident waves is still large enough to obscure and interfere with the backwards propagating scattered waves. In the backscattered region, directional wavenumber filtering can be applied to further separate forward and scattered propagating waves. Additionally, the pixel-noise has become more visually prominent and phase velocity filtering can be applied to help mitigate such effects. Both types of wavenumber-frequency filtering are applied to the residual wavefield data as described in section 4.1.2.

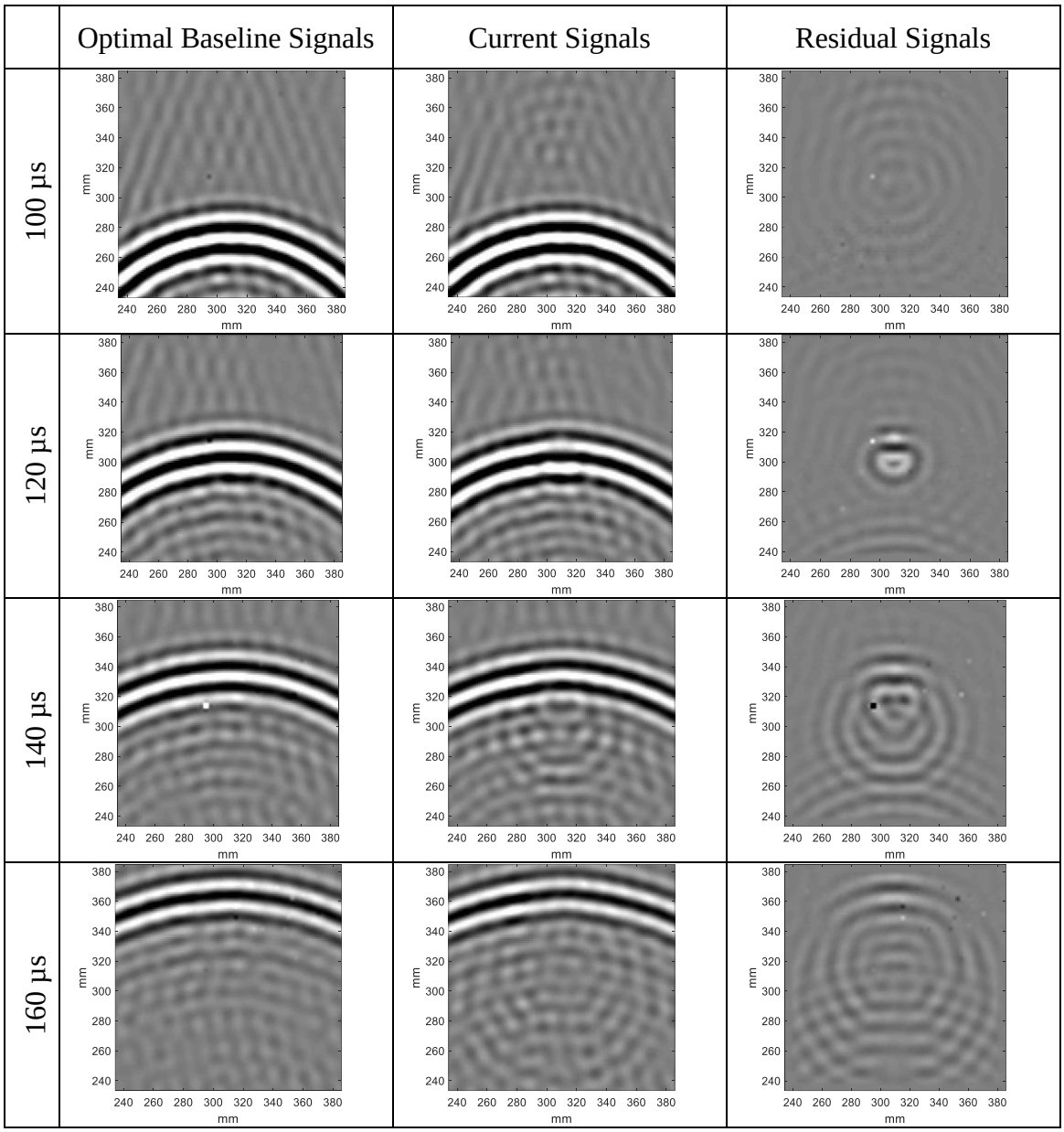

Figure 21 – Wavefield "snapshots" from the optimally shifted baseline signals, current signals and residual signals produced from source T4 with aluminum disc artificial damage.

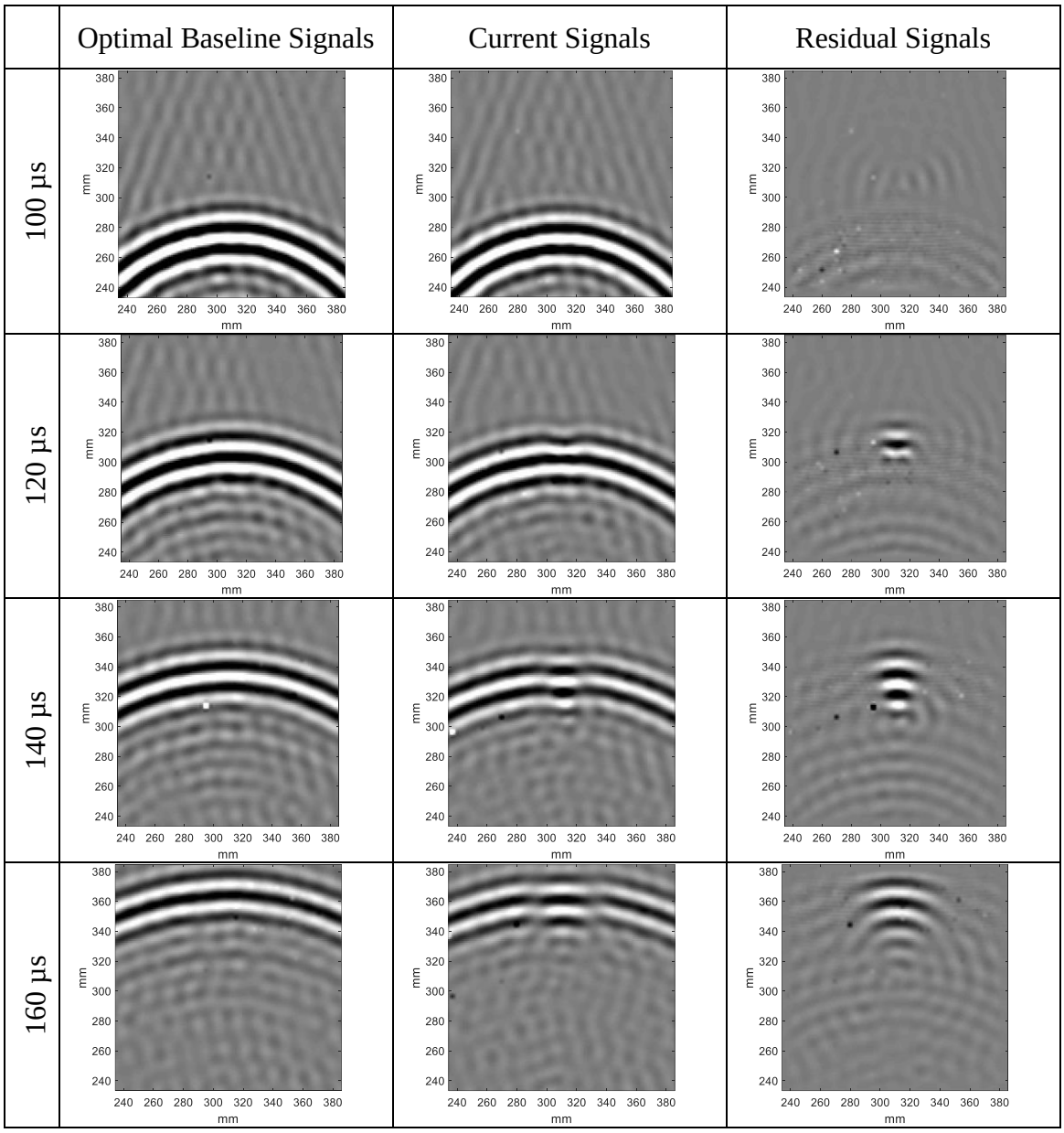

Figure 22 – Wavefield "snapshots" from the optimally shifted baseline signals, current signals and residual signals produced from source T4 with impact 3 damage.

The 3-D wavenumber-frequency filter restricts phase velocity to a desired range. This range was determined by the estimated phase velocity results in section 3.4.1 and then empirically adjusted to 1-1.4 mm/µs to account for the smoothed edges of the phase velocity filter.

The specific steps of the phase velocity filtering process are as follows:

- Take 3-D Fourier transform: $w(x,y,t) \xrightarrow{\mathcal{F}} W(k_x,k_y,\omega)$.
- For each discrete frequency, calculate wavenumber filter boundaries: $k_{\min} = \omega/c_{\max}$ and $k_{\max} = \omega/c_{\min}$.
- Apply filter with 33% Tukey window edges to smooth k_r filter boundaries.
- Apply a 33% Tukey window across 0 to 150 kHz to avoid aliasing.
- Take inverse 3D Fourier transform: $W'(k_x,k_y,\omega) \xrightarrow{\mathcal{F}^{-1}} w'(x,y,t)$.

Figure 23 illustrates the filtering process applied to 3-D residual wavefield data with the aluminum disc. The results in the space-time domain after applying this filtering process are shown in column 2 of Figure 24 and Figure 25.

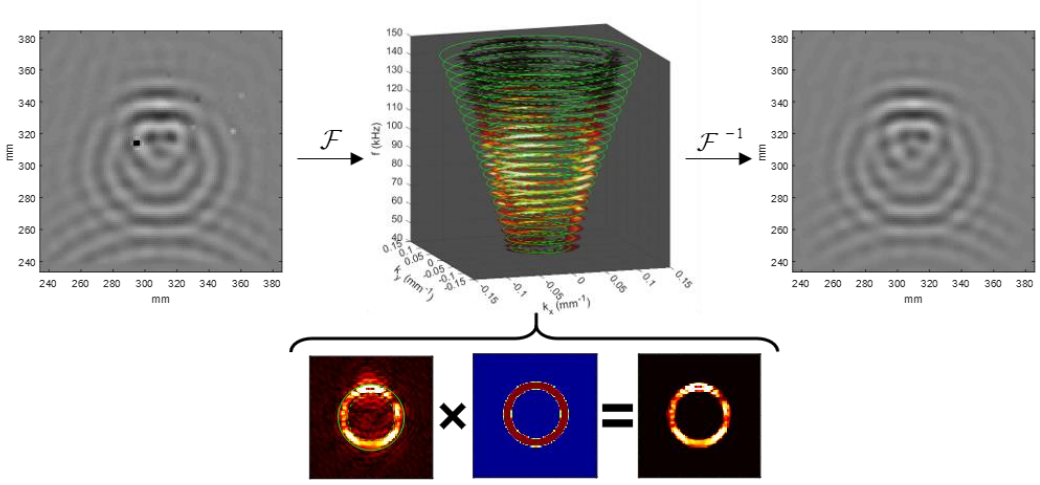

Figure 23 – Flowchart illustrating phase velocity filtering process for 3-D wavefield.

A comparison between the unfiltered and phase-velocity-filtered images indicates that most of the noise was suppressed without affecting the scattered wave data, however, the scattered waves are still partially masked by overlapping incident waves due to imperfect alignment from baseline subtraction. To correct for this, directional wave filtering is

applied to the phase velocity filtered data to isolate the back scattered waves from forward propagating incident waves.

The specific steps of the directional filtering process are as follows:

- Apply spatial window with 10% Tukey windowed edges for a desired angular range to separate the full wavefield $w'(x,y,t)$ into $w'_f(x,y,t)$, which contains forward scattering and $w'_b(x,y,t)$, which contains backward scattering .
- Take 3-D Fourier transform of backward scattering window: $w'_b(x,y,t) \xrightarrow{\mathcal{F}} W'_b(k_x,k_y,\omega)$.
- Apply directional filter with 10% Tukey windowed edges along wavenumber vectors relative to incident direction: $\theta_p = \theta_{inc} \pm 45°$.
- Take inverse 3D Fourier transform: $W''_b(k_x,k_y,\omega) \xrightarrow{\mathcal{F}^{-1}} w''_b(x,y,t)$.
- Add forward scattered and filtered backscattered wavefields: $w'_f(x,y,t) + w''_b(x,y,t) = w''(x,y,t)$.

Figure 26 shows the process for directional wavenumber filtering the 3-D wavenumber-frequency data. The range of -45° to +45° for incident wave propagating angles was chosen as the differential between scattered wave direction and incident wave direction and is large enough to remove interfering waves without affecting scattered wave information. Column 3 of Figure 24 and Figure 25 shows fully filtered wavefield "snapshots" for both aluminum disc and impact 3 damage cases.

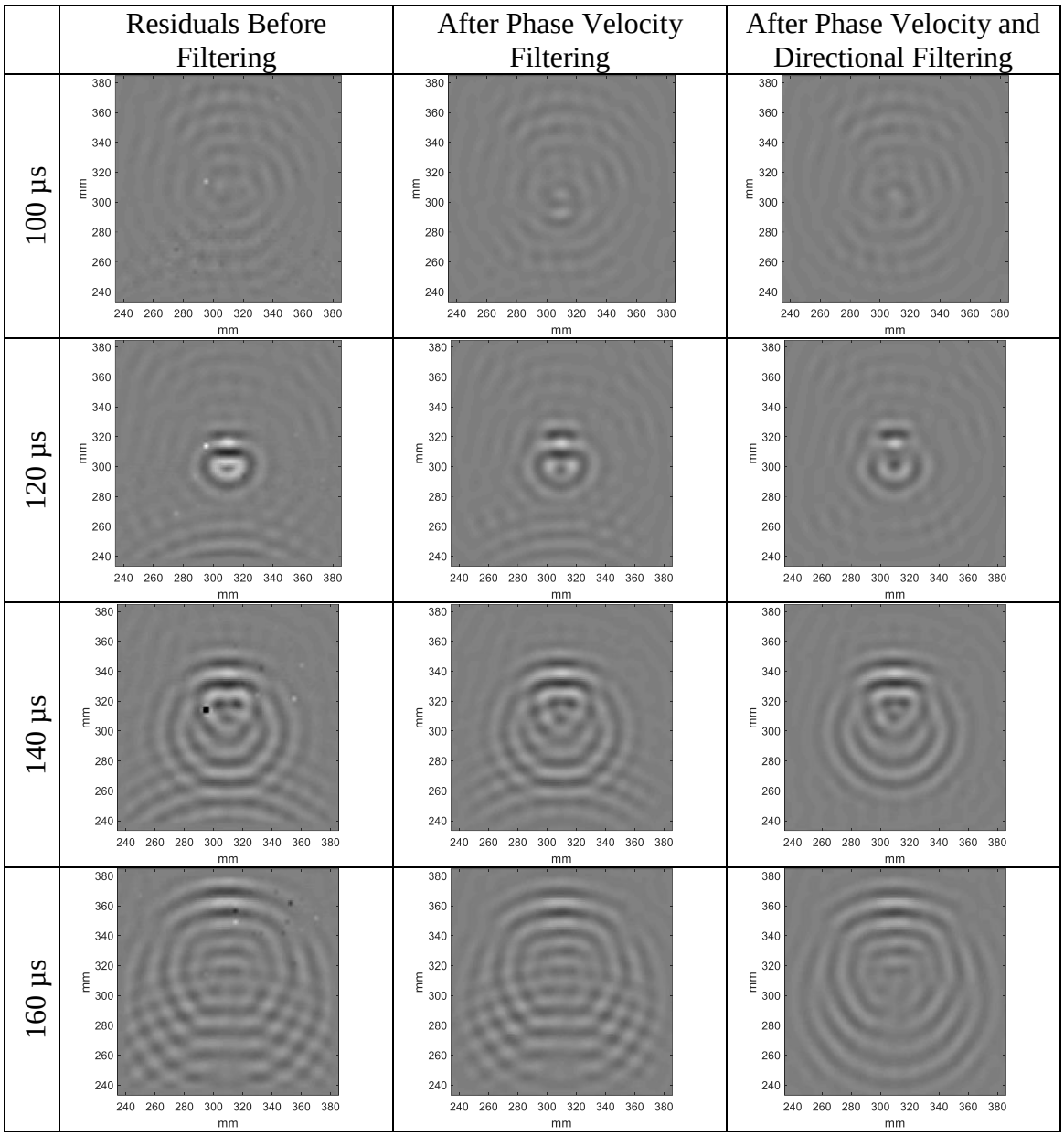

Figure 24 – Wavefield residual "snapshots" from source T4 with aluminum disc artificial damage before and after wavenumber-frequency filtering.

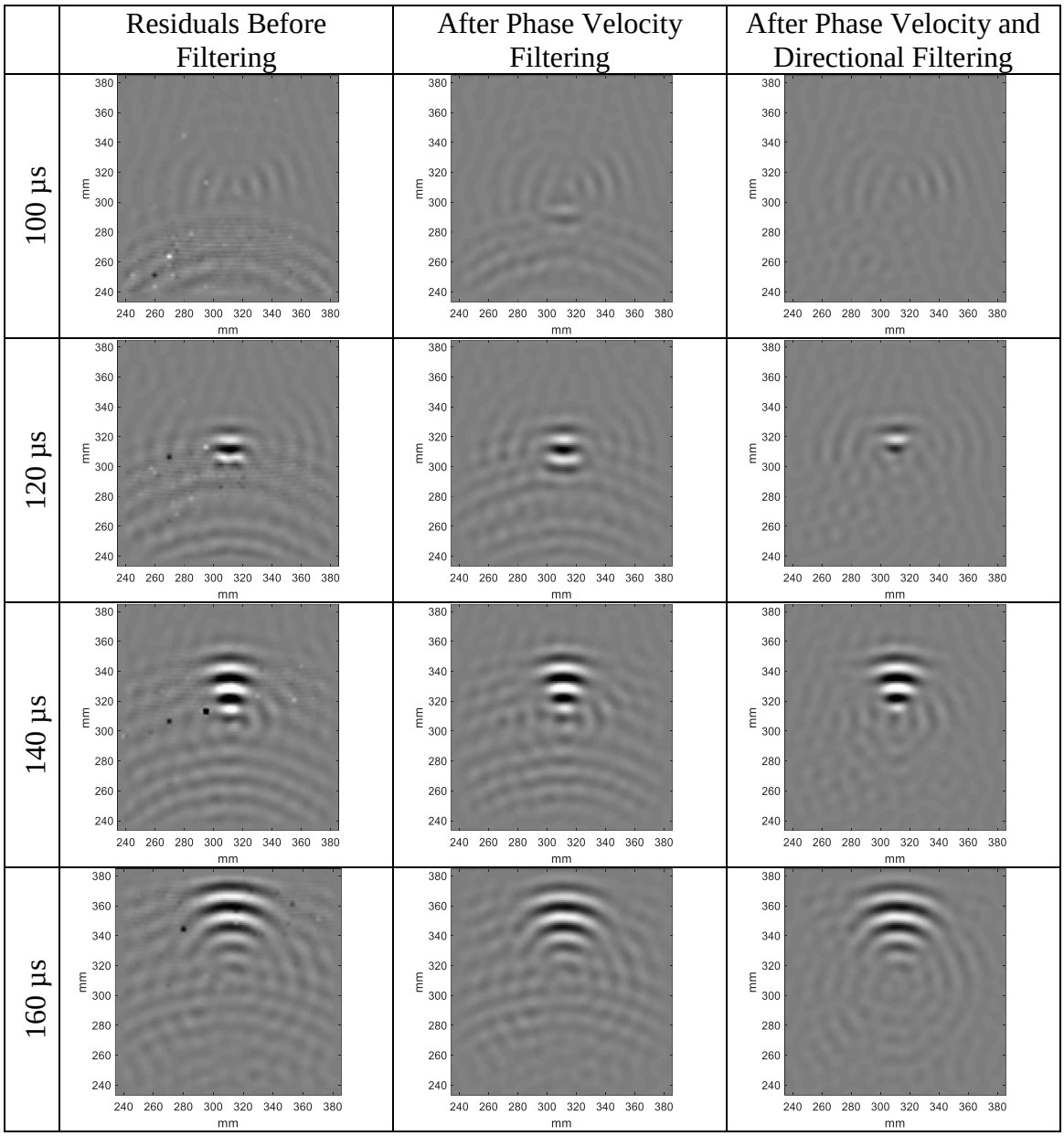

Figure 25 – Wavefield residual "snapshots" from source T4 with impact 3 damage before and after wavenumber-frequency filtering.

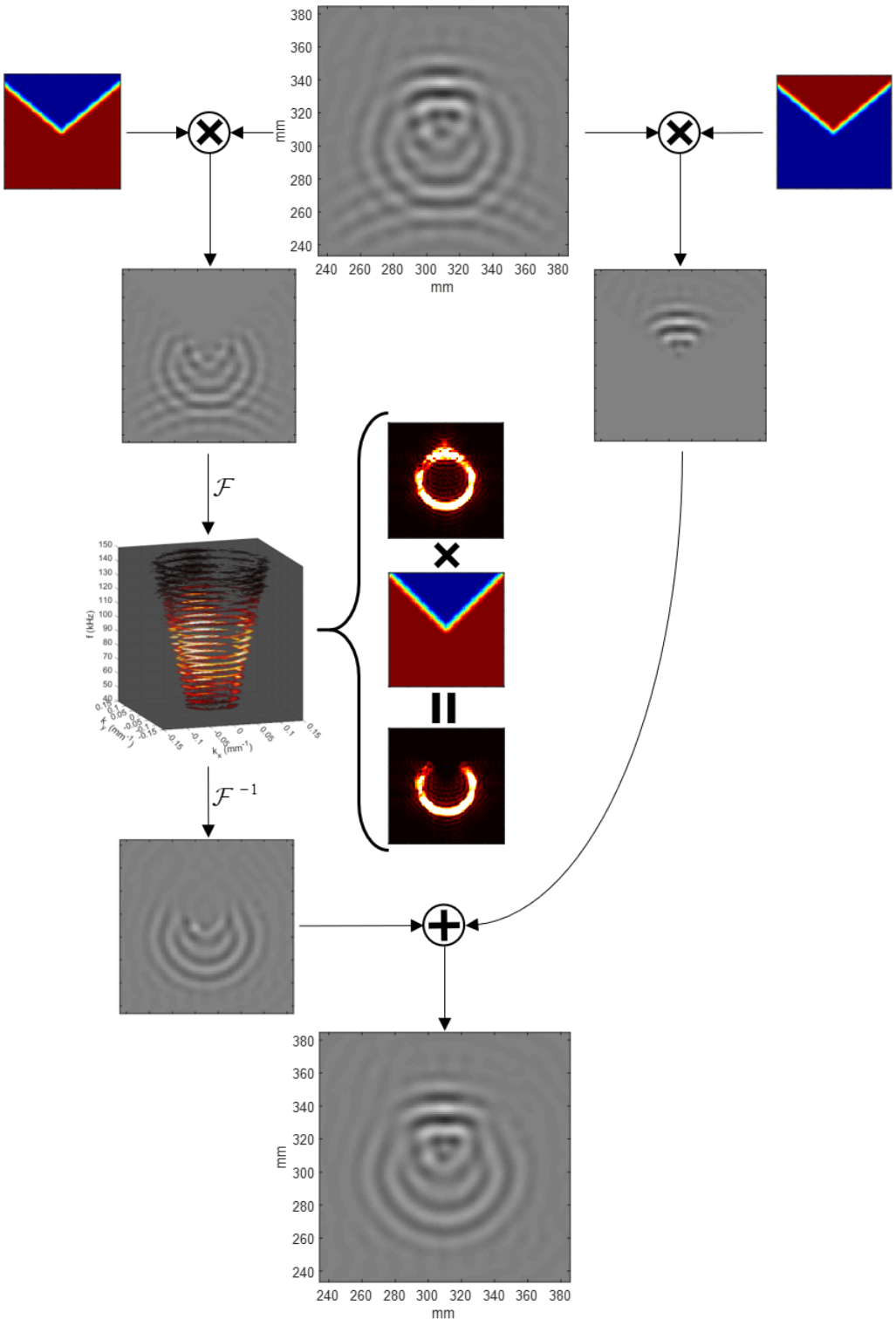

Figure 26 – Flowchart illustrating directional wavenumber filtering process for 3-D wavefield.

In both damage cases, the pixel-wise noise and the incident waves obscuring the scattered waves were significantly reduced. The remaining scattered waves are readily visible. The scattered waves generated by the aluminum disc in Figure 24 consist of comparable forward and back scattered waves. The back scattered waves, however, have a doublet scattering effect caused by the wave packet's interaction with the disc's near-side and far-side edges. The change in local mass and thickness at the disc's edge produces scattering as the propagating wave packet continues to contact the disc's edge over time. This was not observed for the impact damage in Figure 25 where large forward scattering and almost no back scattering occurred.

4.2.3.2 Estimated Scattering

The scattered waves from each flaw have been isolated from noise and interfering waves. Baseline subtracted circular wavefield residual data directly measured using the LDV from series "BCA" and "BCI" without additional processing is used as a comparison to validate the effectiveness of wavenumber-frequency filtering to remove noise and unwanted wave interference. To estimate the scattering profile of the flaw from the grid data, the grid data is remapped to 2-D angle-time data as discussed in section 4.1.3. The radius and angular increment for interpolating a circular wavefield from the grid data are chosen to match the directly measured 2-D circular data. This mapping from (x,y,t) to (θ,t) is achieved using a 50 mm radius and a 1° angular increment. Figure 27 shows a side-by-side comparison of the directly measured circular wavefield, unfiltered circular wavefield extracted from the rectangular data, and the corresponding filtered circular wavefield for both the aluminum disc and impact 3 with a 90° incident direction. The scattered wave packet is visible on both the directly measured and the linearly interpolated circular

wavefields; however, the 3-D filtering of full wavefield data before interpolating the circular wavefield provides an improved isolation of the scattered wave packet with almost no incident wave interference or noise. Note that the signal amplitude levels in Figure 27(a) and 27(b) are different from Figure 27(c)-(f) because of the different gains used during acquisition of circular and full wavefield data while the grayscale is kept the same amongst each image. All further analyses are based solely on the grid scan data because of the significantly improved quality of the residuals as compared to those obtained from the circular scans.

	Directly Measured Circular Wavefield	Extracted Circular Wavefield Before Filtering	Extracted Circular Wavefield After Filtering
Al Disc	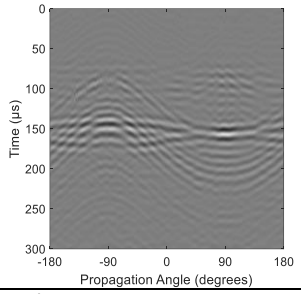	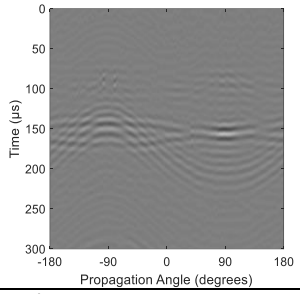	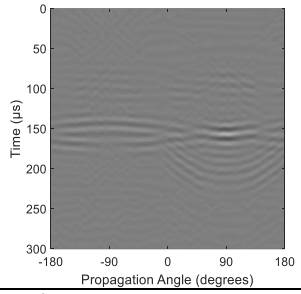
Impact 3	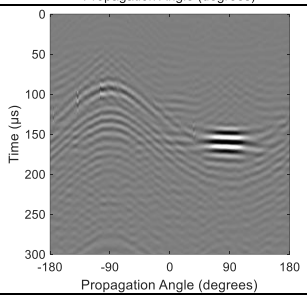	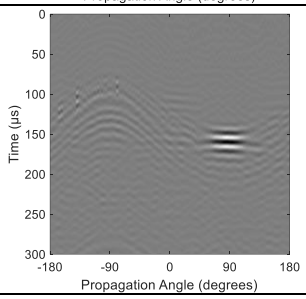	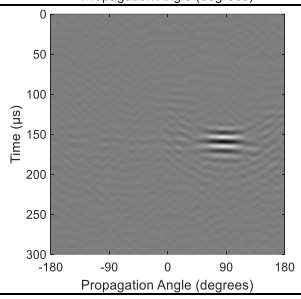

Figure 27 – Directly measured circular wavefields and unfiltered and filtered extracted circular wavefields represented as B-scans from T4 source data for the aluminum disc and impact 3.

The wave doublet as seen from the filtered wavefield residual signal snapshots in Figure 24 is again visible in Figure 27 for the aluminum disc; this doublet is centered around -90° and 155 μs. The radial geometry of the damage, in this case the 20 mm-diameter aluminum disc, is responsible for both an initial reflection off the near edge of

the damage and then a secondary reflection off the far edge of the damage. The damage geometry is used when calculating the scattered wave arrival times from the front edge since the damage does not resemble a point-like scatterer previously assumed in prior work [100].

Figure 28 shows the RF signals and envelope-detected signals of the filtered circular wavefields for the aluminum disc and impact 3 overlaid with the calculated arrival times given from the specular reflection model described in section 4.1.3. The scattering profile is estimated directly from the enveloped signals using the estimated arrivals.

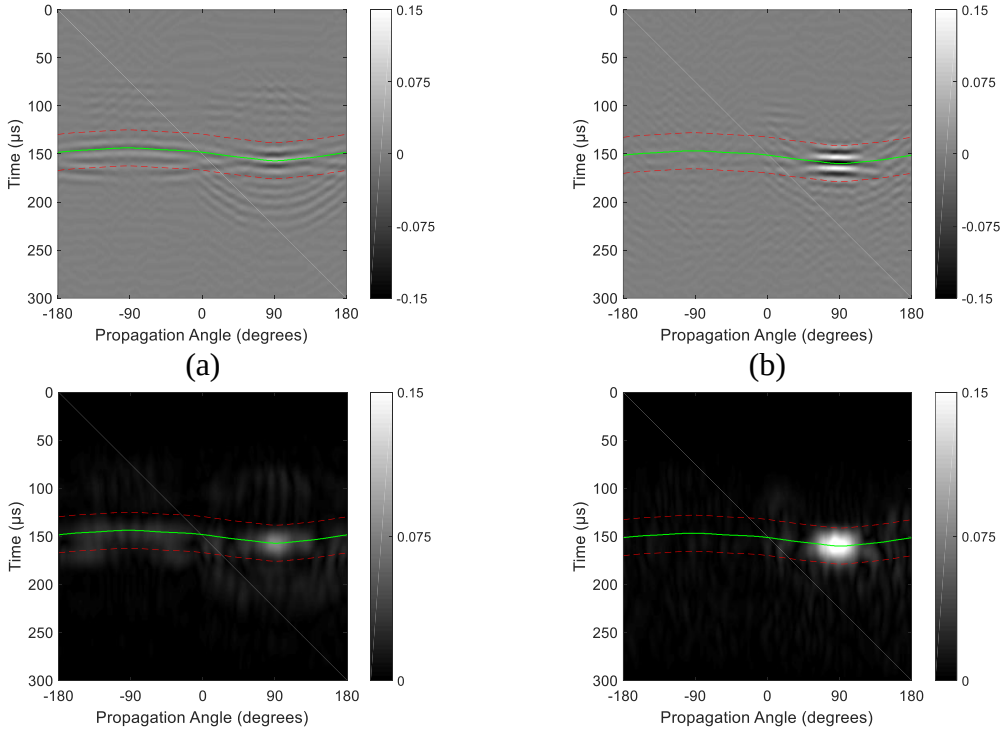

Figure 28 – Filtered estimate of circular wavefield from T4 source data. RF signals for (a) aluminum disc damage and (b) impact 3 damage. Enveloped signals for (c) aluminum disc damage and (d) impact 3 damage. Wave packet boundaries and peak arrival times shown by dashed red lines and green dashed line, respectively.

Scattering patterns are shown in Figure 29 and Figure 30 for all artificial and impact damage cases. In Figure 29, the scattering from each artificial defect has its own unique

pattern that varies with incident wave direction. With respect to each defect, the patterns associated with 0° and 90° are very similar in shape and amplitude. Additionally, it is observed that the patterns from the 45° incident direction have slightly narrower forward scattering lobes and a small reduction in backscattering amplitude when compared with the other two incident directions. The forward scattering amplitude levels are considerably larger in all cases compared to the backscattered amplitudes. The overall scattering amplitude is similar between the magnet stack and aluminum disc but is almost double for the copper pipe. Unlike the magnet stacks, the aluminum disc and copper pipe have reduced scattering amplitudes along the axis perpendicular to the incident propagation direction. Additionally, small secondary lobes can also be seen forming at about 45° from the 0° and 90° incident directions for these two artificial damage types, while the scattering from the magnet stack is generously less directional and more elliptical in shape.

In Figure 30, the impact damage scattering patterns are more consistent between varying incident wave angle and damage size growth apart from the 45° incident wave patterns, which have slightly smaller amplitude than those for 0° and 90° incident directions. Almost no back scattering is observed in all impact damage sizes while a narrow, single forward scattering lobe increases in amplitude with the increasing size of each impact damage case.

	0° Incidence	45° Incidence	90° Incidence
Magnet Stacks	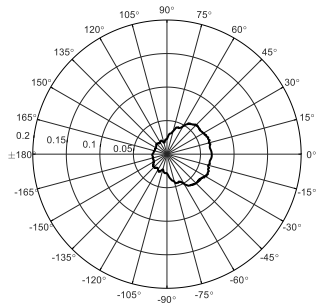	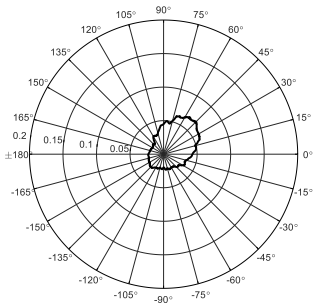	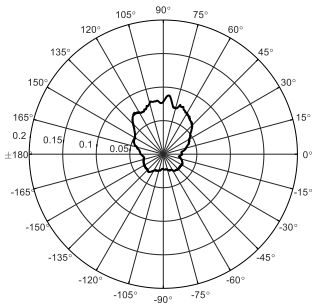
Aluminum Disc	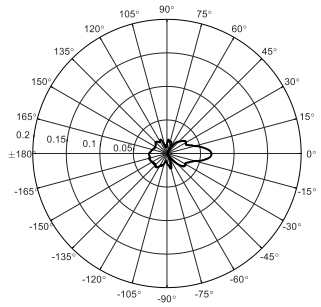	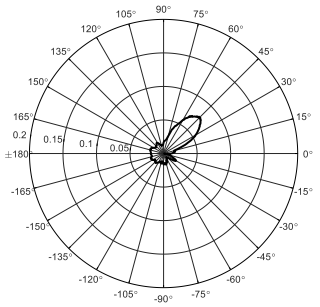	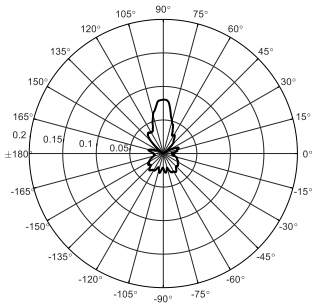
Copper Pipe	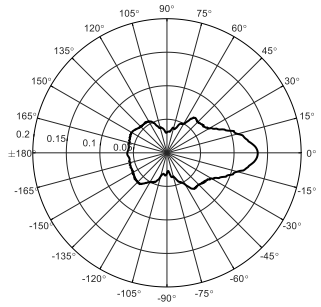	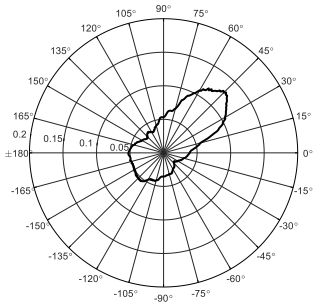	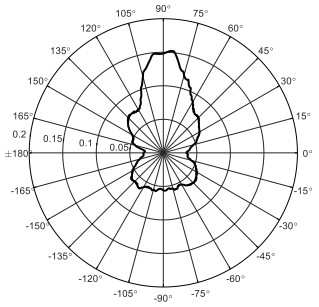

Figure 29 – Raw estimated scattering patterns of all artificial damage cases for 3 different incident directions.

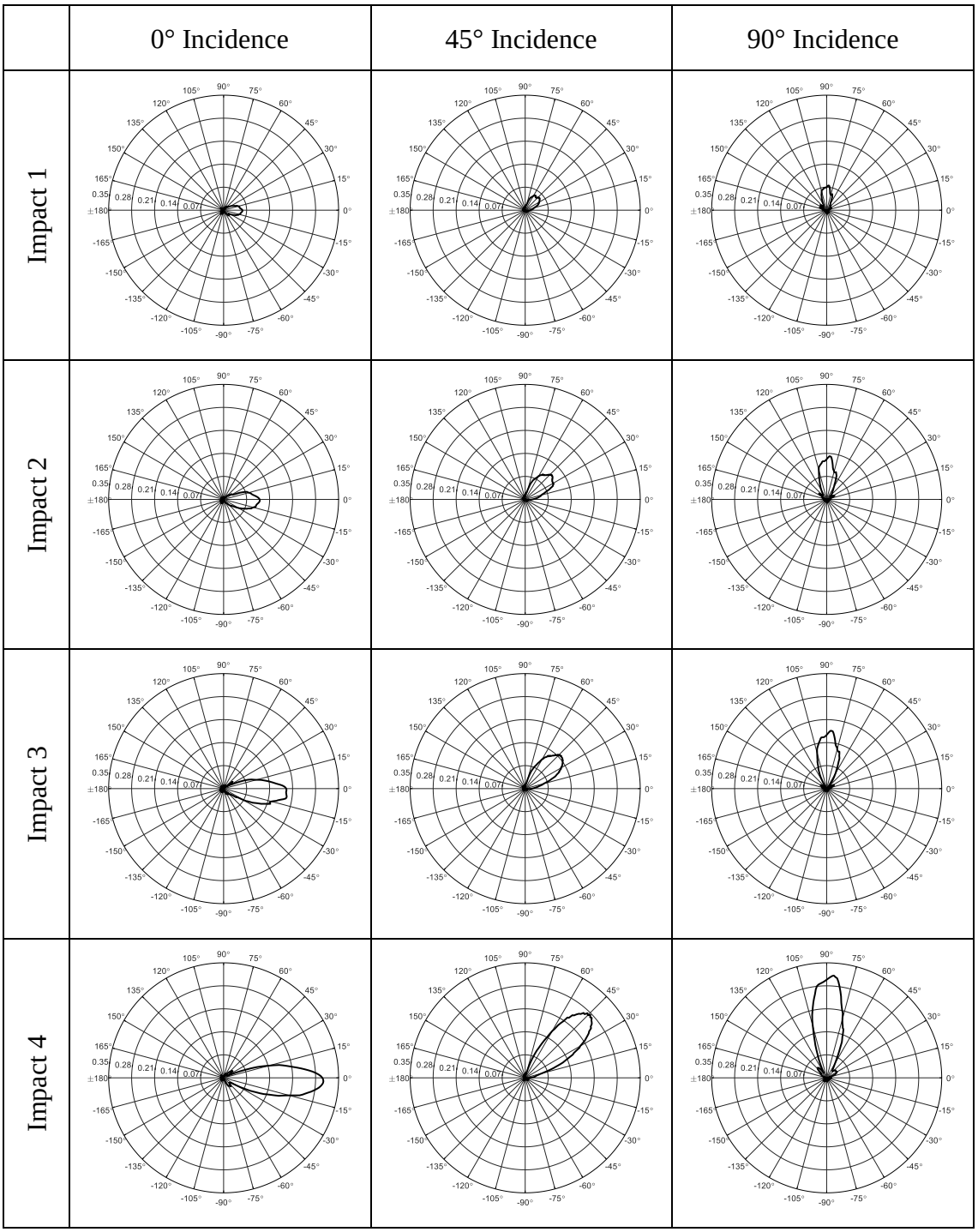

Figure 30 – Raw estimated scattering patterns of all impact damage levels for 3 different incident directions.

4.2.3.3 Estimated 2-D Scattering Matrices

The methodology described in Section 4.1.4 is used to generate scattering matrices for the estimated scattering patterns. Before the initial matrix, A, is filled according to Equation (29) with scattering amplitude values, symmetry from the quasi-isotropic fiber layup is exploited to generate additional datasets to fill columns within the matrix. The symmetry applies to incident waves propagating at 0°, ±90°, and ±180° and again for ±45° and ±135° propagation directions. Since data were acquired along the 0°, 45° and 90° incident directions, these three scattering patterns were mirror-imaged about their propagation direction to help reduce noise in the patterns. Additionally, the patterns from 0° and 90° were aligned to their incident direction and averaged together to form a single pattern that applies to 0°, ±90° and ±180° incident directions while the 45° pattern can be applied to the ±45° and ±135° incident directions. The result is two distinct scattering patterns that form datasets for nine incident wave propagation directions that must be shifted to represent the incident direction of the column in A for which it is applied. As it applies here, this matrix has the following populated columns:

$$A = [s_{-180} \quad s_{-135} \quad s_{-90} \quad s_{-45} \quad s_0 \quad s_{45} \quad s_{90} \quad s_{135} \quad s_{180}]. \tag{42}$$

From here, the methodology derived in section 4.1.4 can be used to produce both an estimated scattering matrix and its reciprocal matrix as shown in Figure 31 for the aluminum disc case. Uniform normalization is applied to each matrix as only the amplitude pattern of the matrix is significant. Figure 32 shows the resulting scattering matrices after averaging the estimated and reciprocal scattering matrices for all artificial and impact damage cases.

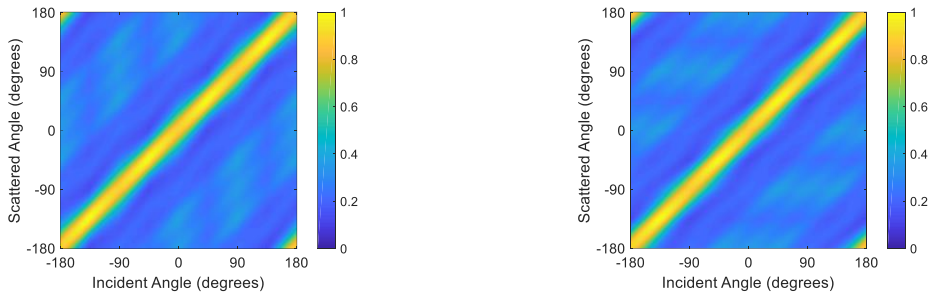

(a) (b)

Figure 31 – (a) Estimated and (b) reciprocal 2-D scattering matrices (normalized).

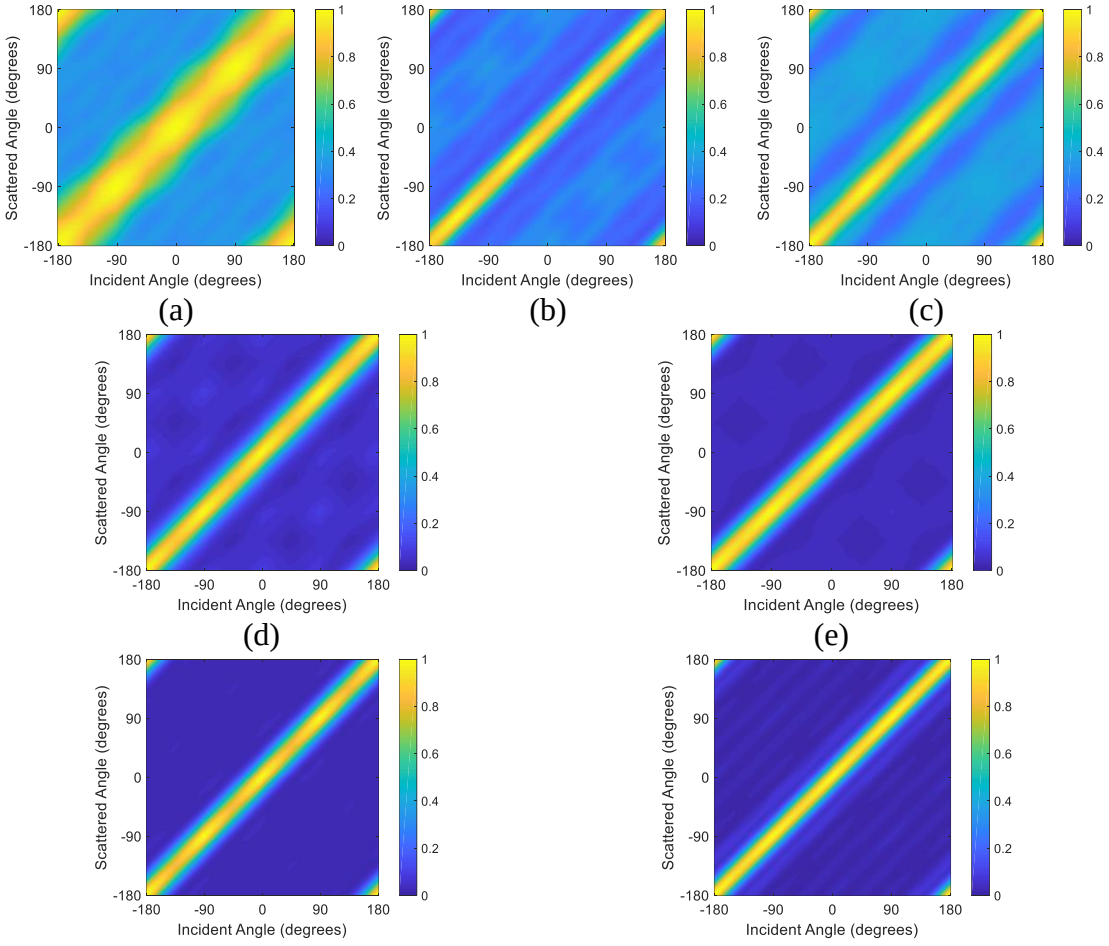

(a) (b) (c)

(d) (e)

(f) (g)

Figure 32 – Normalized 2-D scattering matrices for: (a) magnet stacks, (b) aluminum disc, (c) copper pipe, (d) impact 1, (e) impact 2, (f) impact 3 and (g) impact 4.

4.3 Panel C: Orthotropic Panel

An additional series of experiments was conducted to characterize scattering from artificial and real impact damage using a higher-quality orthotropic composite panel referred to as Panel C. The experimental setup is described here, and the acquired data are processed according to the methodologies described in section 4.1

4.3.1 Panel Description

The panel described in section 3.5.1.1, Panel C, was used for characterizing wave propagation and measuring scattering from artificial and real impact damage. The transducer bonded to the center of Panel C during wave propagation measurements described in section 3.5 was removed. An 8-element array was then bonded to the surface of Panel C in the same manner described in Section 4.2.1 using identical transducers. The array configuration and panel layout are shown in Figure 33.

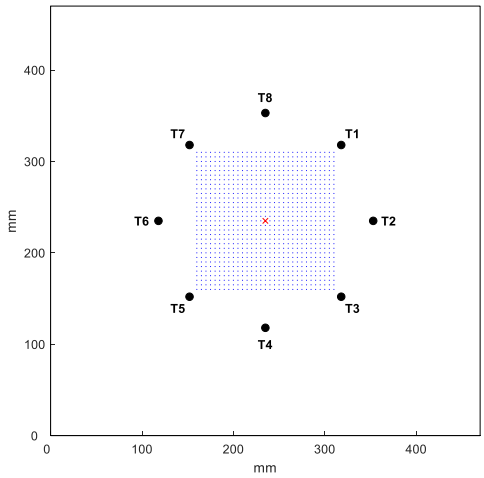

Figure 33 – Diagram of Panel C indicating the transducer locations (small solid circles), the full wavefield measurement path (blue dashed lines) and applied damage location (red "x").

4.3.2 Laser Vibrometer Measurements

Wavefield data were recorded in a rectilinear grid pattern measuring 150 mm in both the *x*- and *y*-directions with a 2.5 mm spatial increment. The pattern was centered about the applied damage location shown in Figure 33. The same measurement equipment and procedures described in section 3.1.2 were conducted here along with using the same linear sine wave chirp excitation from 40 to 150 kHz. All data were post-processed to an equivalent response from a 3-cycle, 80 kHz, Hann-windowed tone burst excitation. Amplification of the received data signals was not required; however, the filtering and digitization parameters were kept the same.

4.3.2.1 Simulated Damage

The same artificial damage types discussed in section in 4.2.2.1 were also used to estimate scattering behavior in Panel C. A series of grid scans ("CGA" series) were performed and summarized in Table 7. These scans were only performed for the 0°and 45° incident directions due to time constraints preventing acquisition of data generated from additional incident directions. The 90° incident direction can be assumed to be nominally identical to 0° in an orthotropic panel.

Table 7. Rectangular grid wavefield scans of artificial damage from Panel C.

Scan	Flaw	Source	Description
CGA1 – CGA2	---	T5 –T6	Baseline grid wavefield measurements
CGA3 – CGA4	Magnets	T5 –T6	Grid wavefield measurements for estimating scattering from magnet stacks
CGA5 – CGA6	Al Disc	T5 –T6	Grid wavefield measurements for estimating scattering from aluminum disc
CGA7 – CGA8	Cu Pipe	T5 –T6	Grid wavefield measurements for estimating scattering from copper pipe

4.3.2.2 Impact Damage

Impact damage was created in Panel C using the same method described in section 4.2.2.2. Only one delamination was introduced in Panel C for these measurements where the impact energy needed to produce the delamination referenced in Table 8 was roughly twice of what was needed for Panel B for a similarly sized delamination. The same approach for acquiring wavefield data was taken for impact damage as was for artificial damage, where the scan series "CGI" for the grid scans performed is summarized in Table 9. Both size and depth of the delamination were evaluated by immersion C-scans and is described in section 5.2.

Table 8. Impact drop height and calculated impact energy.

Designation (Impact Level)	Drop Height (cm)	Calculated Impact Energy (J)
1	83.82 (33")	8.04

Table 9. Rectangular grid wavefield scans of impact damage from Panel C.

Scan	Flaw	Source	Description
CGI1 – CGI2	---	T5 –T6	Baseline grid wavefield measurements
CGI3 – CGI4	Impact 1	T5 –T6	Grid wavefield measurements for estimating scattering from impact 1

4.3.3 Estimation Results

Anisotropy was characterized on Panel C since a separate panel was not available. This characterization was used in estimating the scattering from artificial and impact damage. All wavefield data were down-sampled from 20 MHz to 2.5 MHz and were deconvolved to a 3-cycle, 80 kHz tone burst excitation before post-processing. Here the methodologies described in section 4.1 are applied and the estimated results are shown.

4.3.3.1 Postprocessing of Full Wavefield Data

The same postprocessing approach used for Panel B was performed on Panel C data. GSTA baseline subtraction is performed and 2x spatially upsampling is applied to improve visualization of data. A different time window of 50 to 80 μs was used for aligning incident waves during application of GSTA. Figure 34 and Figure 35 shows time "snapshots" at 80 μs, 100 μs, 120 μs, and 140 μs to illustrate baseline subtraction performance for data series CGA and CGI at an incident direction of 90° for an aluminum disc and impact 1.

As was seen after baseline subtraction with Panel B data, the forward incident wave amplitude has been reduced significantly. The scattering from both the artificial and impact damage is now visible. There is still interference from the remaining forward incident waves and pixel-wise noise that partially obscures the scattered waves.

After applying baseline subtraction, phase velocity filtering is applied to the residual data as done previously in section 4.2.3.1. Here, the phase velocity range used for Panel C was adjusted from its estimated range in section 3.5.2 to 0.9 to 1.6 mm/μs. This range was chosen to prevent the removal of wavenumber content corresponding to propagating waves of interest. Results from applying both phase velocity and directional filtering are shown in Figure 36 and Figure 37.

Very similar results to Panel B are observed after applying both types of wavenumber-frequency filtering. The remaining forward incident waves are almost completely removed, and the added pixel-wise noise has been significantly reduced for both damage cases. These results show the robustness of the methodology for reducing noise and interfering waves.

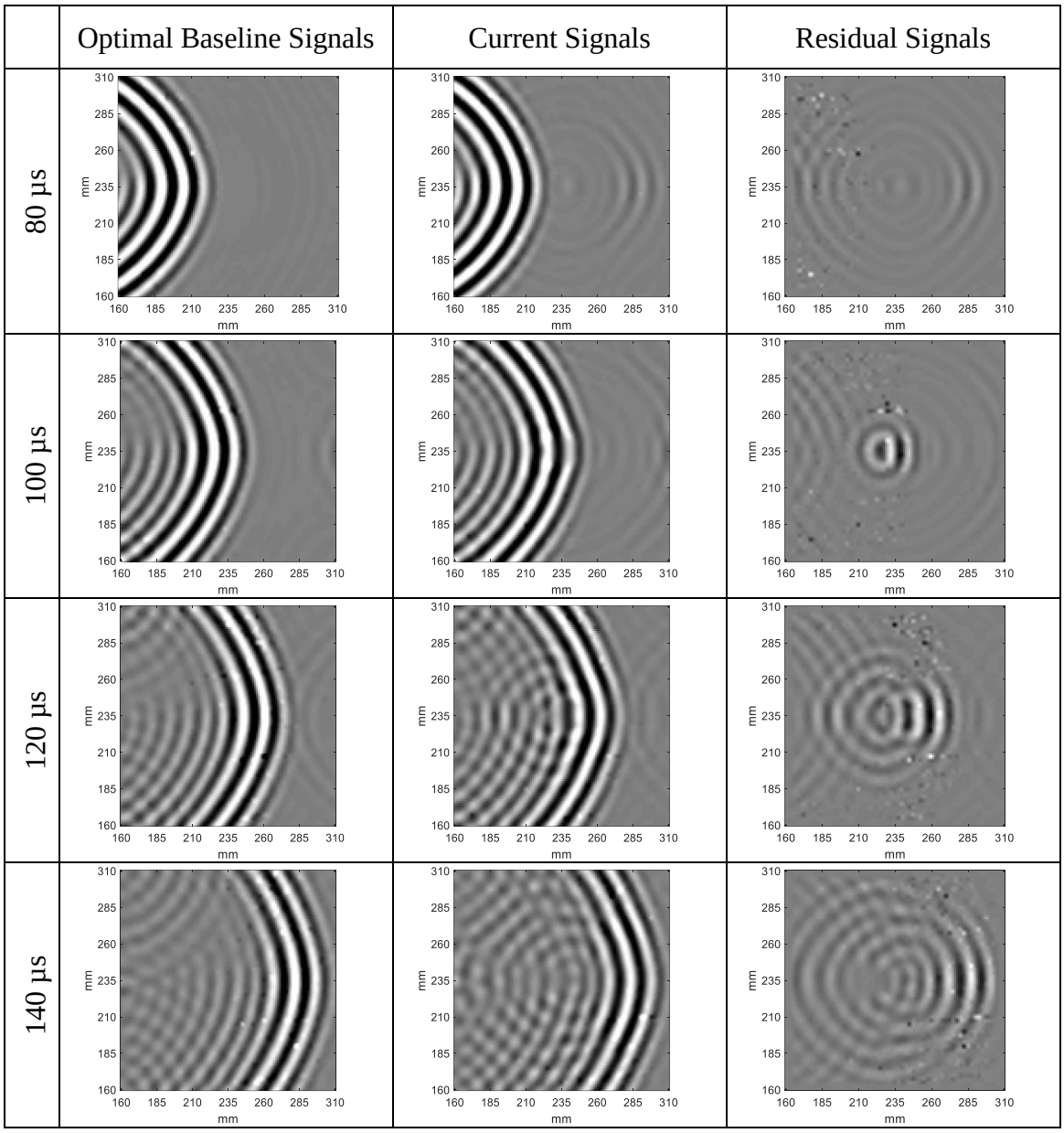

Figure 34 – Wavefield "snapshots" from the optimally shifted baseline signals, current signals and residual signals produced from source T6 with aluminum disc artificial damage.

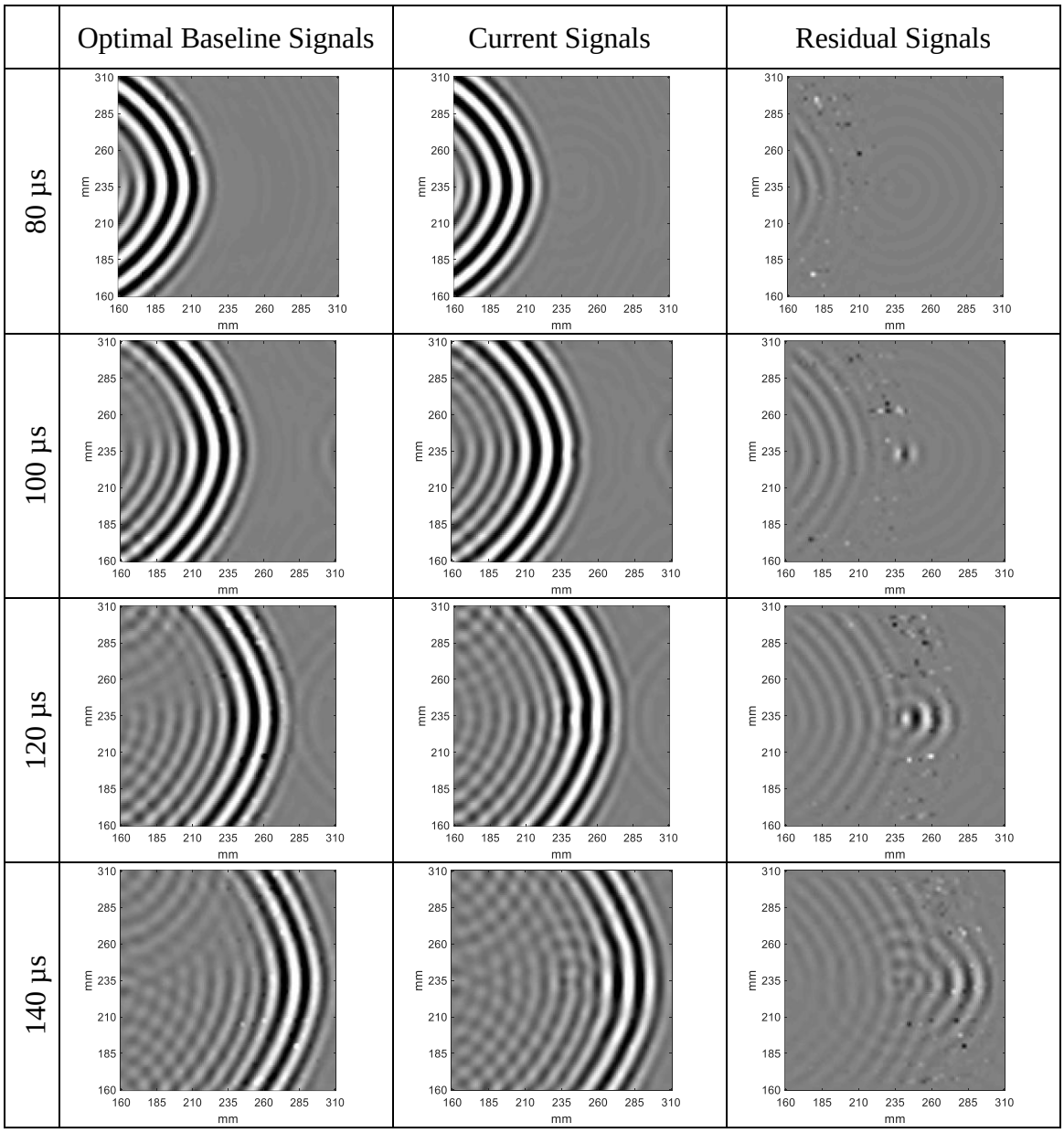

Figure 35 – Wavefield "snapshots" from the optimally shifted baseline signals, current signals and residual signals produced from source T6 with impact 1 damage.

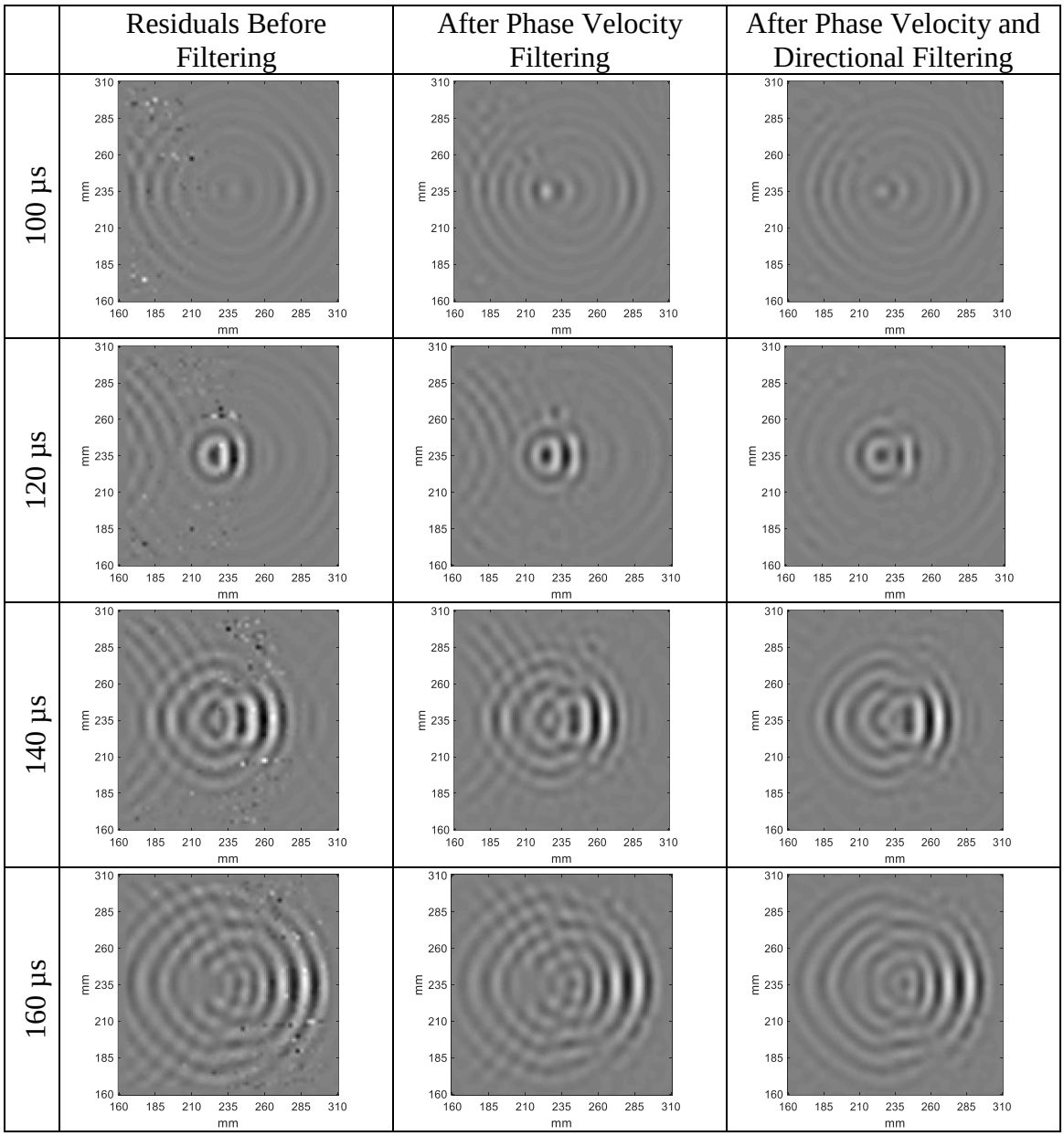

Figure 36 – Wavefield "snapshots" from the residual signals, phase velocity filtered residual signals and phase/directionally filtered residual signals produced from source T6 with aluminum disc artificial damage.

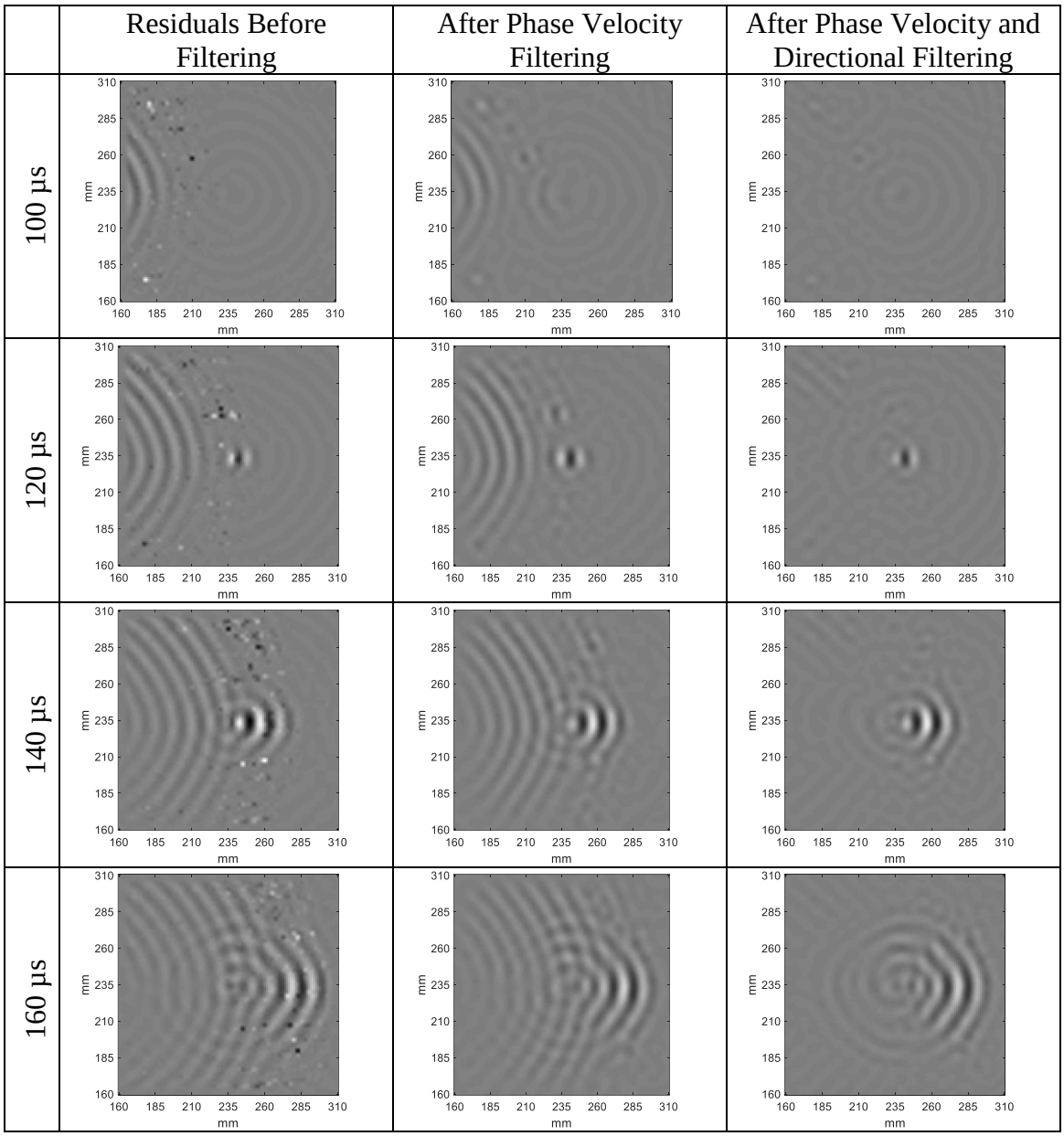

Figure 37 – Wavefield "snapshots" from the residual signals, phase velocity filtered residual signals and phase/directionally filtered residual signals produced from source T6 with impact 1 damage.

4.3.3.2 Estimated Scattering

The mapping of data from (x,y,t) to (θ,t) is performed so that a direct estimate of the scattering profiles can be obtained. A 1° angular increment and 35 mm radius was chosen

instead of the previous 50 mm radius because of edge reflections arriving earlier in time for the smaller panel.

Figure 38 shows the unfiltered and filtered circular wavefield B-scans for the aluminum disc and impact damage cases. It is evident that the interfering waves and noise from the unfiltered B-scans are substantially reduced, leaving the scattered wave packets readily visible. The wave doublet corresponding to the aluminum disc previously mentioned from Panel B data is again shown in Figure 38 while the impact damage shows only scattering primarily in the direction of the incidence wave.

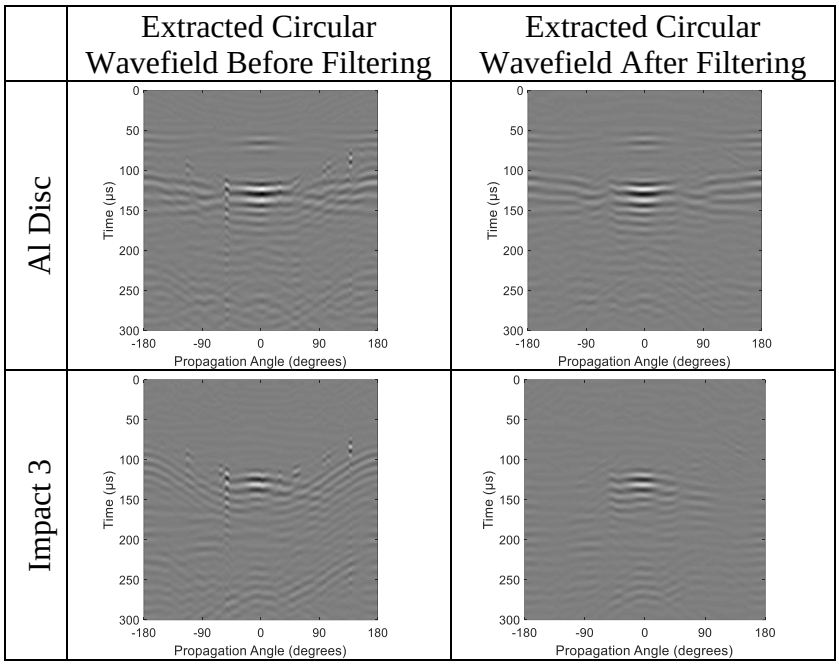

Figure 38 – Unfiltered and filtered extracted circular wavefields represented as B-scans from T6 source data for the aluminum disc and impact 1.

After incorporating the specular reflection model in section 4.1.3 to estimate the arrival times of the scattered wave packet for each specific damage type, the raw scattering profiles were extracted and are shown in Figure 39 for both artificial and impact damage cases given two separate directions of incidence. In Figure 39, each damage case exhibits

a unique scattering pattern with some similar behavior depending on incident wave propagation direction. For all three artificial damage cases at 0° incidence, similar backscattering behavior is observed. Scattered energy in the form of directional lobes is focused along the ±180° directions. Additional energy can be seen along the ±90° directions for the magnet stacks and ±105° for the aluminum disc and copper pipe roughly perpendicular to incident wave propagation direction. This concentration of energy follows the general fiber directions of this orthotropic panel, as to be expected, while the amplitude of these lobes varies with damage type. With regards to forward scattering for 0° incidence, a single large lobe is focused along the 0° direction with varying amplitudes for all three artificial damage cases. Among these main lobes focused primarily along fiber directions, there is additional evidence of much smaller lobes beginning to form along the ±45° and ±135° directions for both the magnet stacks and copper pipe but not for the aluminum disc.

For 45° incidence, backscattered energy again continues to concentrate along the main fiber directions. This is evident from two separate lobes forming along the -90° and ±180° directions for all three cases. Forward scattering, however, is significantly different for the magnet stacks than for the aluminum discs and copper pipe as the forward scattered energy is less focused along the direction of incidence and more evenly distributed between the 0° and 90° fiber directions. The forward scattering of the aluminum disc and copper pipe is more concentrated along the 45° incident direction with the lobe having two separate peaks centered around 30° and 60°. In addition, the aluminum disc and copper pipe have smaller lobes beginning to form along the 0° and 90° fiber directions, as well as, even smaller lobes along the -45° and 135° directions for the copper pipe.

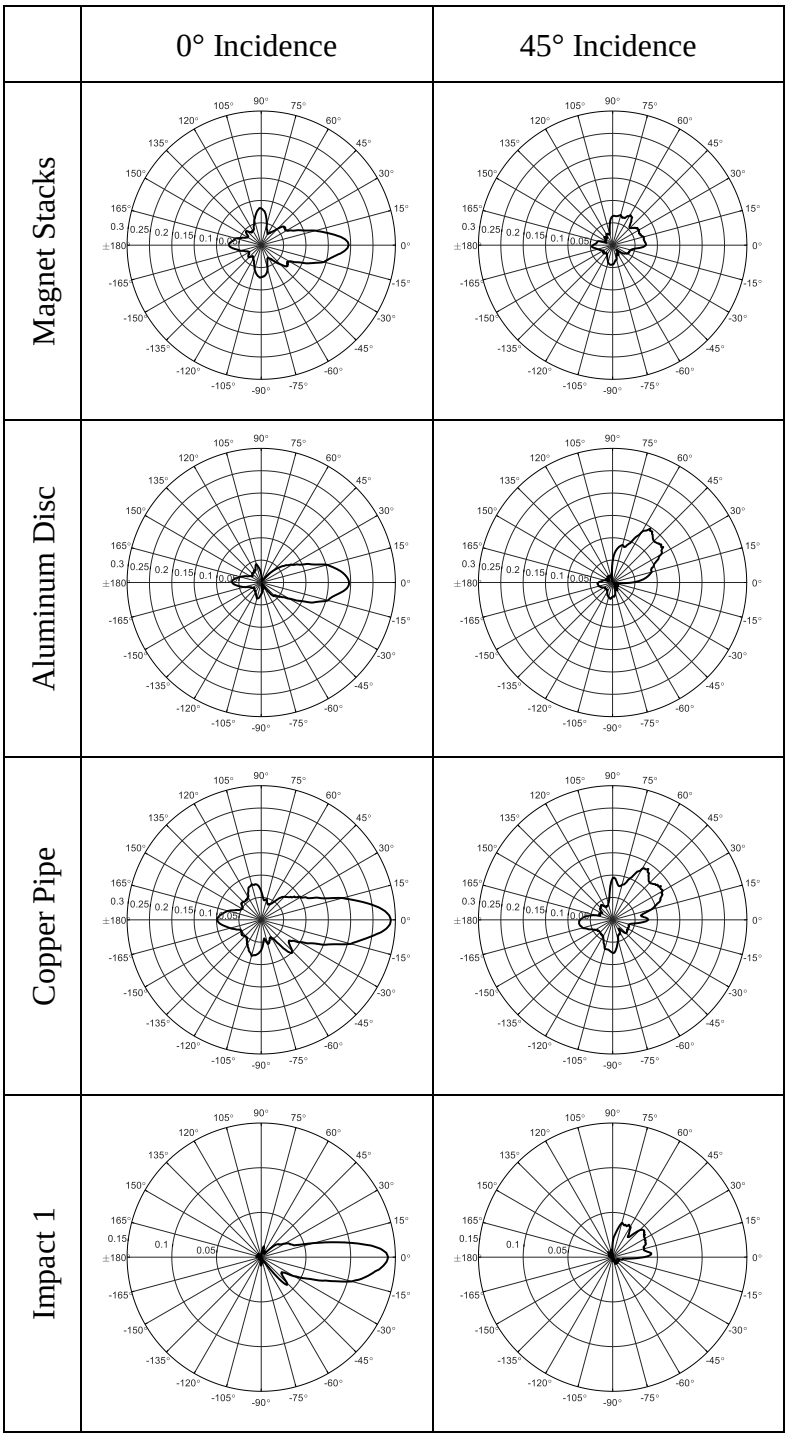

Figure 39 – Raw estimated scattering patterns of all artificial damage and impact damage cases for 2 different incident directions.

The scattering related to impact damage is much simpler than the artificial damage in both directionality and amplitude. For both 0° and 45° almost no backscattering is

observed. For forward scattering with 0° incidence, there is a single lobe that forms along the 0° fiber direction with an additional singular lobe focused along the -45°. This additional lobe could be a result of measurement error or inhomogeneities as the pattern should be symmetric. For 45° incidence, the forward scattering is like the magnet stack as the forward scattered energy is distributed more evenly between the 0° and 90° fiber directions.

4.3.3.3 Estimated 2-D Scattering Matrices

The same methodology for Panel B is used to generate scattering matrix estimates for Panel C from two unique incident direction datasets. Fiber symmetry is again exploited to fill more columns in the initial scattering matrix, A. Both datasets for 0° and 45° incidence are mirrored across their incident wave direction and averaged, as done previously with Panel B. The averaged scattering profile for 0° incidence can be used to fill in the columns that represent the 0°, ±90°, and ±180° incident directions of the initial scattering matrix while the 45° dataset is used to fill in the ±45° and ±135° columns after the appropriate shift is applied for each column. Once the initial scattering matrix is sparsely filled, the methodology discussed in Section 4.3.3.3 for estimating the final scattering matrix are applied. Normalized estimates of the final scattering matrix for both artificial and impact damage cases are shown in Figure 40.

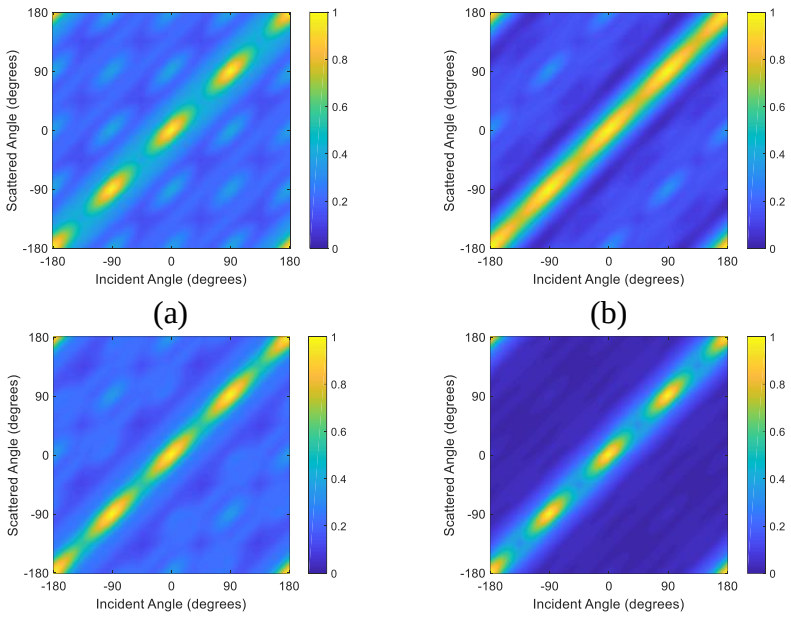

Figure 40 – Normalized 2-D scattering matrices for: (a) magnet stacks, (b) aluminum disc, (c) copper pipe and (d) impact 1.

4.4 Summary

This chapter covers the methodology developed to extract high resolution scattering patterns from wavefield imaging data as well as the methodology for estimating the 2-D scattering matrix from a sparse set of incident directions. The experimental procedures discussed here can be used to help validate FEM data or alternative analytical approaches for estimating scattering in layered composite media.

To capture high-resolution scattering patterns of damage, initial circle scan measurements of guided waves produced from a single direction of incidence were acquired at the center location of damage before and after its application. The measured points within a scan were acquired at defined angular increments with a specified radius away from the damage center. After direct baseline subtraction, the result was residual wavefield imaging data that contained scattering produced by the damage for all angular

directions; however, residual signal amplitudes were relatively small compared to the initial incident waves. These incident waves partially obscured the scattered waves in addition to noisy signals caused by poor surface reflection conditions inherent in many composite materials resulting in noisy scattering pattern estimation. To overcome these drawbacks, additional post-filtering was needed and was achieved through a rectangularly spaced grid of measured data. After improved baseline subtraction was applied, noise reduction through phase velocity filtering and the removal of interfering waves via directional wave filtering was implemented. This method of filtering helped isolate the residual scattering within the wavefield from interfering waves and signal noise. A circular wavefield was extracted from the full wavefield data where the residual scattering was then estimated using a geometric scattering model to determine the expected arrival times of the scattered waves. This was performed for a sparse set of incident wave directions to capture multiple scattering profiles for a specific damage type. Finally, a method to estimate the 2-D scattering matrix for damage within a composite material was developed. The sparsity of incident wave directions was overcome through Fourier fitting of the damage scattering patterns and linearly interpolating the coefficients to estimate scattering patterns for incident wave angles in between the sparse set of incident wave directions.

The results of the estimated scattering had elements that were both expected and unexpected given the two different composite layups examined along with the different types of artificial and impact damage. In the case of Panel B, each artificial damage type had clear and defined scattering characteristics that differed depending on the incident wave direction. Specifically, when comparing the aluminum disc with the copper pipe in

Figure 29, the overall scattering amplitudes of the copper pipe were much larger. Both had relatively large forward scattering when compared to their backscattering and their overall scattering shape was similar except for one difference. The aluminum disc had more defined nulls perpendicular to the incident wave direction. For Panel C, the scattering patterns of the aluminum disc and the copper pipe seem to be dominated more by the fiber direction layup of the orthotropic panel as is evident from the scattering patterns of Figure 39. Scattered energy is concentrated along the 0° and 90° fiber directions, which is seen for both incident directions and is even more evident from the amplitude attenuation map in Figure 13. Interestingly, this energy concentration along the fiber directions affects the forward and backward scattering lobes in the 45° incident wave direction causing separate lobes to be formed symmetrically about the incident wave direction.

The results from estimating scattering from impact damage are generally simpler with less structure than those from artificial damage. In the case of Panel B, as shown in Figure 30, the overall shape of the scattering patterns for all incident directions and damage sizes is predominantly a single forward scattering lobe that increases with size as the impact damage grows in diameter. Unexpectedly, relatively no backscattering is observed. For Panel C, the results are similar. One key difference that stands out is the scattering pattern observed for 45° incidence where the forward scattering amplitude is drastically reduced, which is shown in Figure 39. The scattering observed for impact damage seems to be mostly attributed to a velocity change as the wave propagates over the damage site. As can be seen in Figure 41, the baseline and forward scattered waves for 0° incidence have approximately the same amplitudes while only the phase mismatch caused by slower

propagation speeds over increasingly larger damage results in increasing residual forward scattering amplitudes.

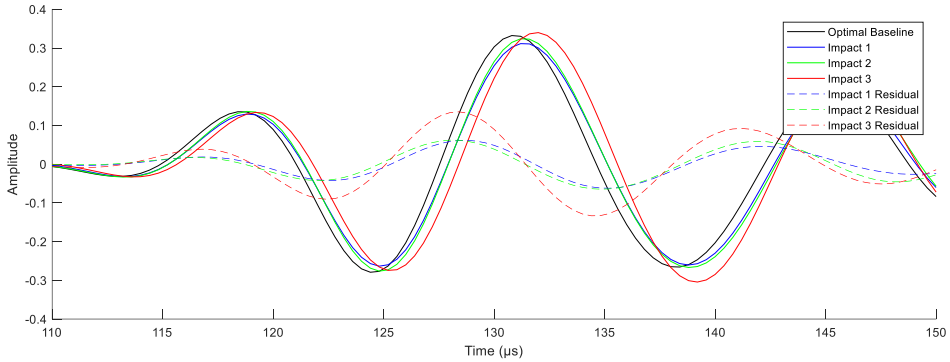

Figure 41 – Baseline and forward scattered wave packets are shown to have increasing phase mismatch with increasing damage size.

5 IMPACT DAMAGE CHARACTERIZATION BY ULTRASONIC INSPECTION

The sites of impact damage in both panels were further characterized using ultrasonic testing (UT) methods to better understand the physical attributes of the induced damage as well as the panels themselves. Through an in-depth characterization of both damage and the panels, comparisons of physical differences in size and depth as well as panel quality are made.

5.1 Air-Coupled Scans

After each impact to Panel B, through-transmission C-scans were performed using air-coupled transducers to evaluate the existence and estimate the size of incurred delaminations. With the use of an automated scanning system, these measurements could be made quickly. Since it is difficult to visually identify when the ply layers have disbonded, these rapid C-scans help determine when the threshold for damage has been met. This saves time when compared to verifying the existence of impact damage with slow wavefield imaging scans. After the existence of damage is confirmed, wavefield imaging can then be performed to gather high resolution scattering data for various delamination sizes.

5.1.1 Experimental Procedures

An immersion tank, typically used for performing UT inspection of materials under water, was retrofitted with a custom aluminium bracket that secured both a transmitter and receiver transducer. These were air coupled transducers in coaxial alignment spaced 90

mm apart to perform through-transmission scans. Panel B was suspended in air using a custom aluminium shelf that mounted to the side of the immersion tank as shown in Figure 42 and was placed in between the transmitter and receiver so that the focal points of the transducers were approximately at the panel's center. A PC running Olympus ScanView Plus software was used to control the xyz scanning stage and performed bilinear raster C-scans over a 254 mm × 254 mm area at a spatial resolution of 1.27 mm centered at the damage location. Pulse-on-position hardware was used with the ScanView Plus software to ensure that excitation of the transmitter occurred at the desired spatial location. An Agilent 33250A arbitrary function generator was used to produce a linear sine chirp from 300 to 500 kHz at 300 mVpp over a 100 μs time window. The chirp was then amplified using an E&I 1040L amplifier to approximately 100 Vpp and transmitted using a QMI AS400Ti air-coupled transducer. The C-scan data were received by a QMI AS400ARi air-coupled transducer that was connected to a custom DC biasing power supply. The received signals were amplified 16 dB and bandpassed filtered from 0.1 to 1 MHz with a Panametrics 5058PR pulser-receiver and then digitized using a DP210 2 GHz 8-bit digitizer PCI card at a sampling frequency of 20 MHz. A block diagram of the scanning setup is shown in Figure 43.

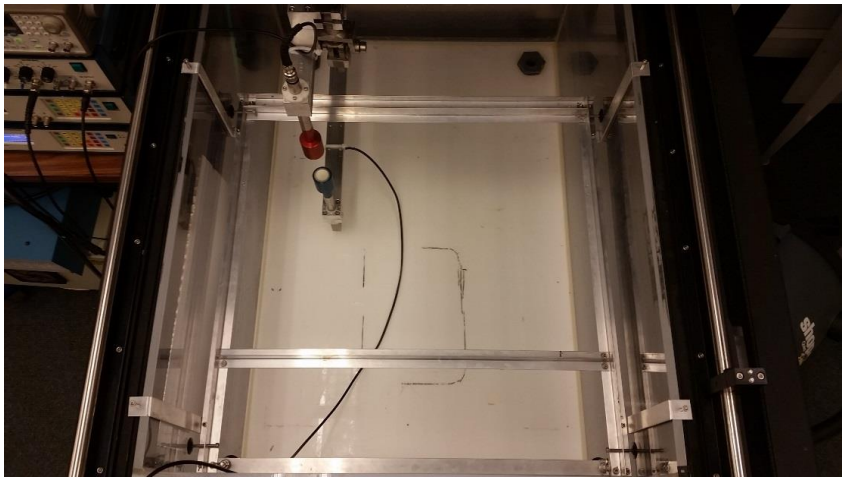

Figure 42 – Immersion scan tank with custom aluminum bracket for suspending materials and performing air C-scans.

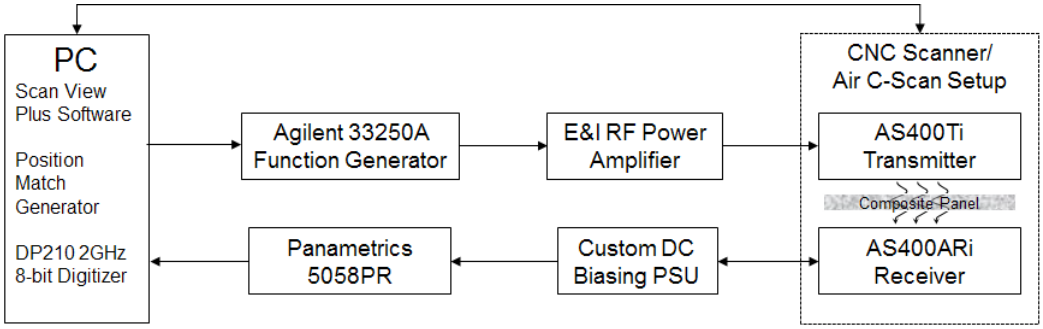

Figure 43 – Block diagram of all equipment used during air C-scan data acquisition.

5.1.2 Through-Transmission Scans

After performing through-transmission air-coupled wavefield scans on Panel B of all four impact damage levels, peak amplitudes are extracted from the received raw unprocessed chirp signals and are shown as C-scans in Figure 44. While the quality of the images is relatively poor due to high signal attenuation in air, the defect locations and estimates of their sizes can be made from the resulting images. A direct estimate of each delamination's size is made from the C-scan images and is displayed in Table 10. The 25.4 mm copper adhesive square was measured to be 28.4 mm in both dimensions from the C-scan images; this ratio of 1.12:1 can be used to adjust the overestimates of all other directly measured

sizes for more accurate sizing of damage. These adjusted estimates are also shown in Table 10.

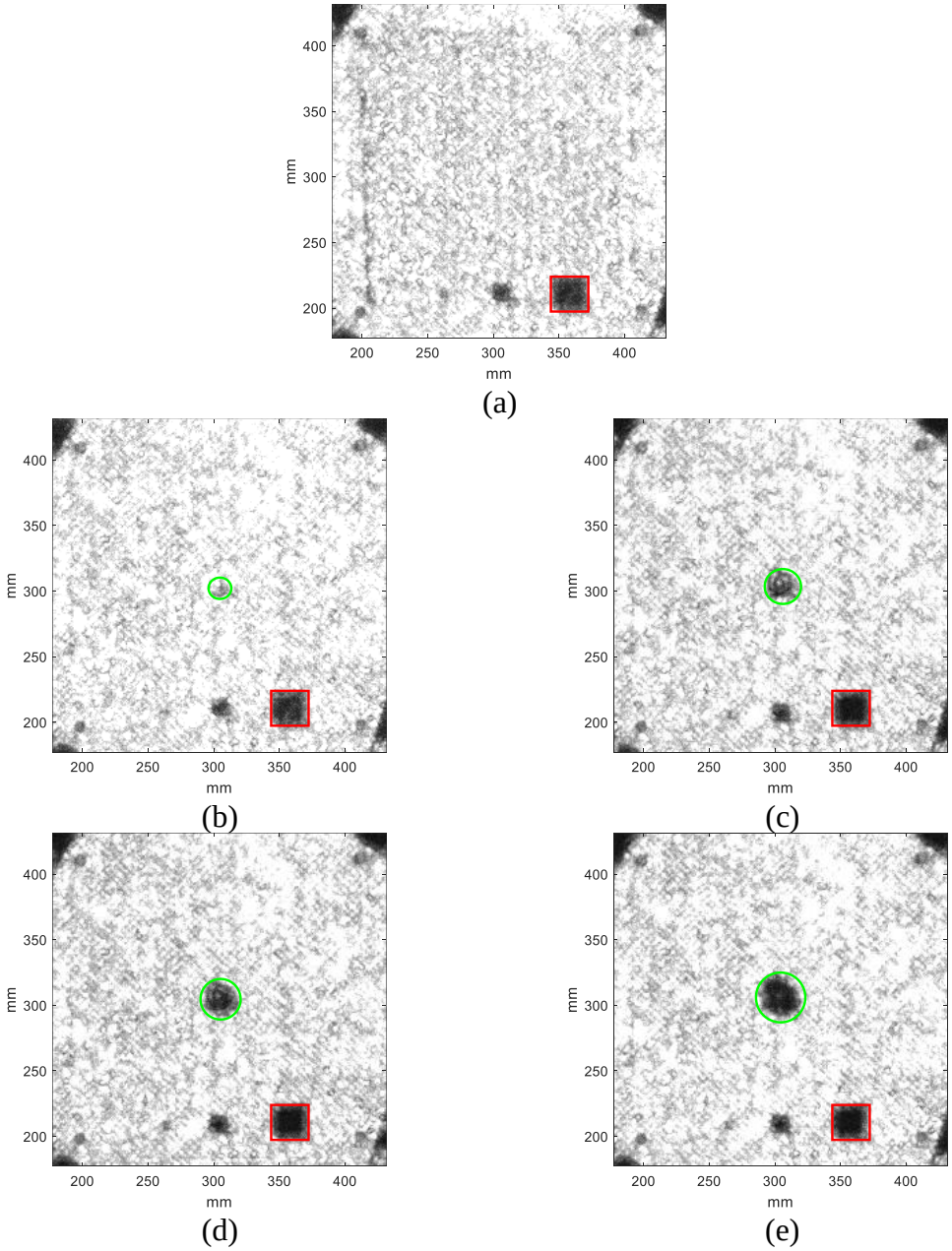

Figure 44 – Air C-scans of Panel B before and after impact damage marked by green circles with adhered precut copper tape marked by red squares. (a) Baseline, (b) impact 1, (c) impact 2, (d) impact 3 and (e) impact 4.

Table 10. Measured and adjusted diameter of the delamination for each impact level.

Designation (Impact Level)	Directly Measured Diameter (mm)	Adjusted Diameter (mm)
1	18.3	16.3
2	21.3	19
3	26.4	23.66
4	31.5	28.1

5.2 Immersion Scans

Immersion scanning techniques are commonly used for rapid inspection of components where the material is submerged in water or another fluid. By transmitting ultrasound in water instead of air, transmitting higher frequencies is possible, improving lateral and near-surface resolution. Damage within a composite can be more accurately characterized, not only in terms of size, but in shape and depth from the panel's surface. Both pulse-echo and double through-transmission modes are used here to characterize the impact delaminations in terms of ply-layer depth and geometry.

5.2.1 Experimental Procedures

The aluminium bracket used with the immersion tank from Figure 42 was removed and the tank was filled 0.25 m high with water. A Panametrics V312 10 MHz transducer was used to conduct both pulse-echo and double through-transmission scans on both Panel B and Panel C. The same PC with ScanView Plus software was used to control the xyz scanning stage with the transducer aimed toward the bottom of the tank. Composite panels were placed 19 mm above the tank bottom's surface using rubber pads in all four corners of the panel. A Panametrics 5800 pulser/receiver was used to produce a 100 μJ pulse excitation.

For Panel B, received signals were then amplified 45 dB and 52 dB for pulse-echo and double through-transmission scans, respectively, in addition to being bandpassed filtered from 1 to 35 MHz while received signals from Panel C were amplified 20 dB and 33 dB for the same respective scans and filtering parameters. All resulting signals were then digitized using the DP210 2 GHz 8-bit digitizer PCI card at a sampling frequency of 200 MHz.

5.2.2 Pulse-Echo Scans

Full waveform measurements used to generate amplitude and time-of-flight C-scans were conducted prior to impacting Panel B and Panel C to obtain baseline data that can be compared to current data obtained after impacts. The scan area is approximately 205 × 205 × 1.27 mm for Panel B and 152 × 152 × 1.27 mm for Panel C where the signals were recorded for a total of 5 μs. Figure 45 and Figure 46 shows signals for data centered at the impact location from Panel B and Panel C obtained before and after applied impacts. The signals represented in Figure 45(a) and 45(b) were averaged over a 10 × 10 mm area to reduce noise. The high signal amplitude beginning at 0 μs indicates the first reflected wave off the front surface or impact side of the panel. Subsequent reflections indicated by each crest in the signal mark individual layers within the composite panel while the last crest in the signal indicates the back-wall reflection and is followed by minimal signal amplitude. The receiver gains were set to visualize this back-wall reflection, but due to the high signal attenuation within Panel B, the points corresponding to the first several reflected waves in Figure 45(a) were saturated.

To visualize the impact damage size and layer depth, C-scans are obtained by extracting the peak amplitude at each pixel location over a specified time-window. The time window is chosen to include all reflections excluding the front surface reflection; a delamination residing within the composite layers would reflect signal energy and would typically be identified by a high amplitude change in the signal when compared to its baseline followed by amplitude loss in the back-wall reflection. Concurrently, the point in time when the signal peaks can be mapped into a time-of-flight C-scan which reveals the depth and relative structure of the delamination.

In the case of Panel B, a time window of 1.0 to 2.5 μs was chosen to avoid the saturated signals. The reduction in energy around 1.5 μs in Figure 45(b) indicates that the delamination is detected in that time window. However, Figure 45(c)-(f) shows peak amplitude and time-of-flight C-scans for baseline and current data where a slight reduction in backwall energy is seen. Figure 45(g) and 45(h) show a horizontal B-scan at y = 305 mm for baseline and current signals. Larger amplitude reflections can be seen at approximately 1.2 μs when comparing the current and baseline signals. While the signal quality is still poor, the back-wall reflection around 2.25 μs also shows a loss of amplitude caused by the delamination. The signals reveal the panel's poor homogeneity, and saturating the signals to compensate for large attenuation effects further exacerbates the poor results.

For Panel C a time window of 0.5 to 2.0 μs was chosen. Figure 46(c)-(f) shows peak amplitude and time-of-flight C-scans that indicate clear and measurable damage along with depth characterization from the time-of-flight C-scan. Figure 46(g) and 46(h) show horizontal B-scans at y = 234 mm. The horizontal lines correspond well with individual

layers of the panel. In Figure 46(h) larger amplitude echoes are visible between 1 μs and 1.25 μs waves caused by the delamination and correspond to a layer depth of 4 to 6 layers, roughly midway in the panel. As a result, a large reduction in the back-wall reflected wave amplitude can also be seen at 1.7 μs. The signals from Panel C are much more uniform unlike Panel B and provide more definitive characterization of the damage within the composite layers.

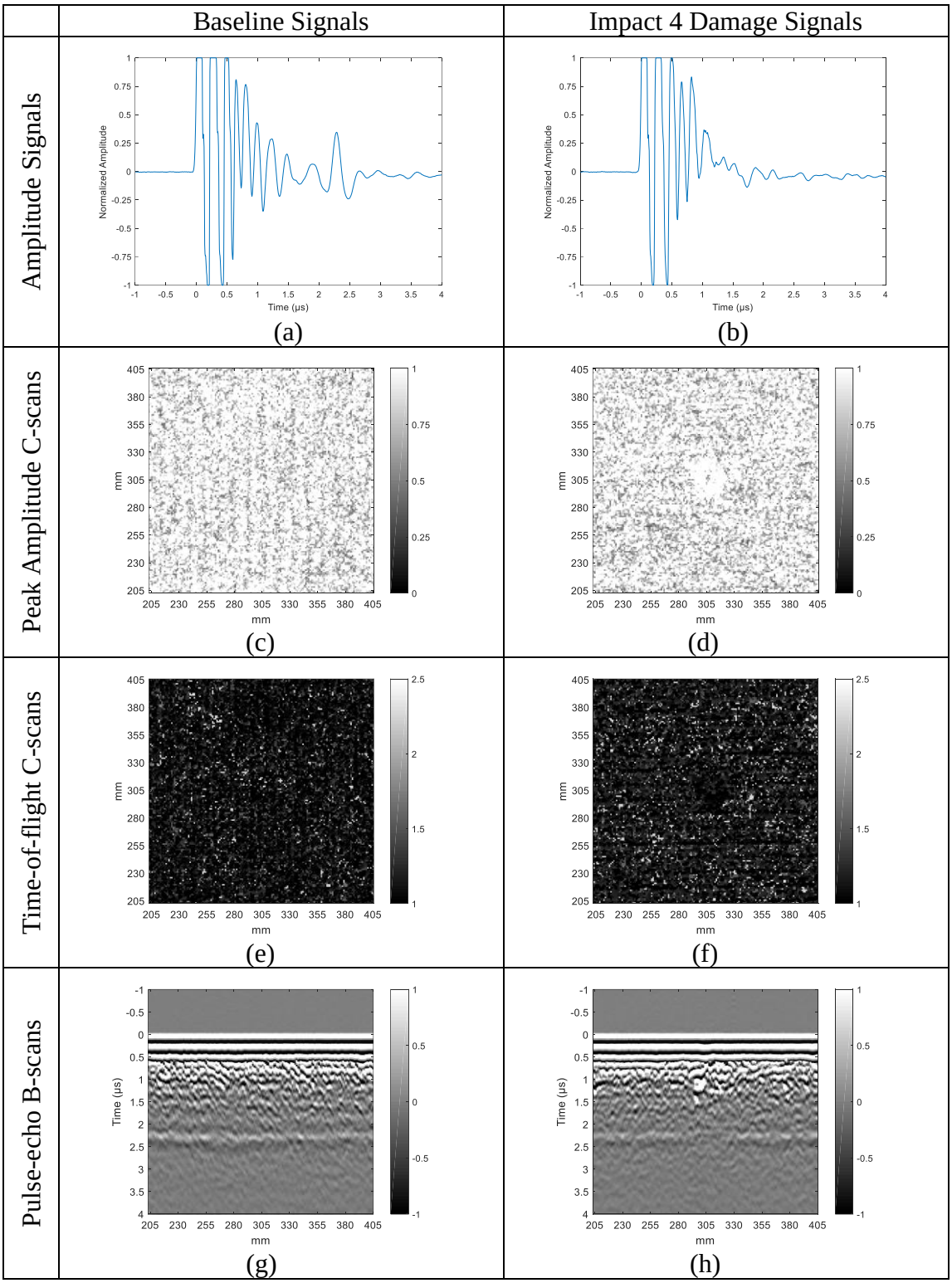

Figure 45 – Baseline and current signals from Panel B immersion scans.

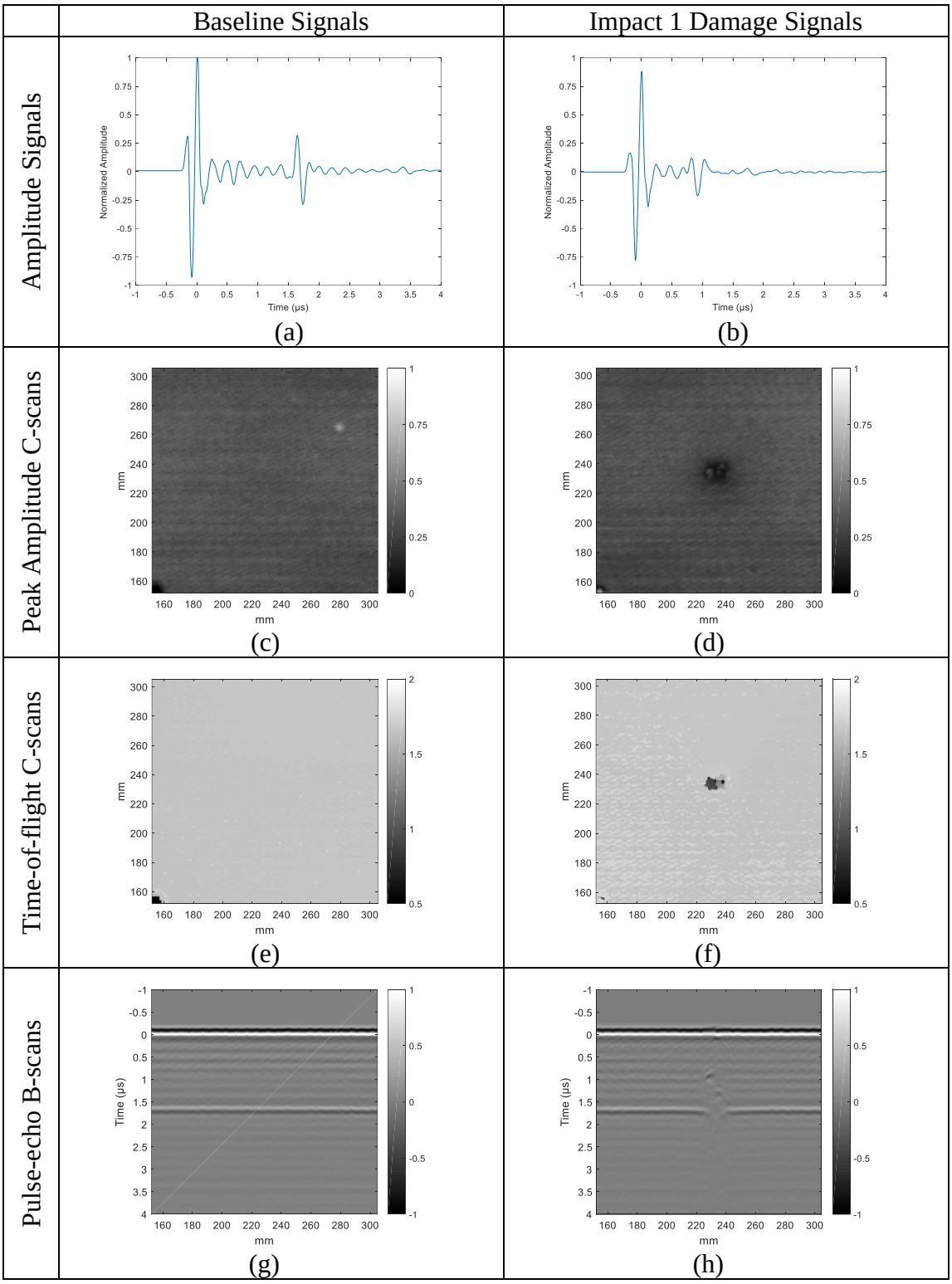

Figure 46 – Baseline and current signals from Panel C immersion scans.

5.2.3 Double Through-Transmission Scans

The double through-transmission scanning method is a form of through-transmission scanning that utilizes only a single transducer. Transmitted waves traverse through the material twice instead of once where a reflective plate under the material is used to reflect energy back to the transducer. Double through-transmission scans were performed on Panel B and Panel C before and after conducting impacts to size the damage. Scan area and resolutions were kept the same as for the pulse-echo measurements for each panel. Peak amplitudes of the received signals were recorded and are shown as C-scans in Figure 47 and Figure 48. Homogeneity issues in Panel B are observed from the C-scans in Figure 47 as the point-by-point peak signal amplitudes are inconsistent. The signals recorded from the pulse-echo measurements of Panel B also showed poor homogeneity between layers where signal quality was inherently inconsistent. Figure 48 of Panel C, on the other hand, shows greater peak amplitude consistency while also revealing fiber structure that can be seen travelling vertically within the image. While the quality of signal differs greatly between the two panels, C-scans of both panels still show the clear presence of impact damage at their respective impact locations. In Figure 47(b), the delamination is almost circular with an approximate diameter of 28 mm, closely matching the adjusted diameter of impact level 4 in Table 10. Figure 48(b) also shows a close-to-circular delamination and has a measured diameter of 11.5 mm.

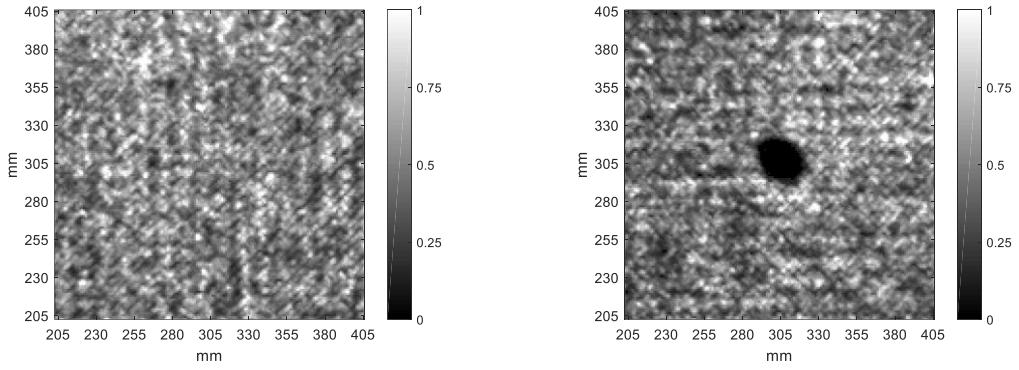

(a) (b)

Figure 47 – Panel B immersion double through-transmission peak amplitude C-scans of (a) baseline and (b) impact 4 damage.

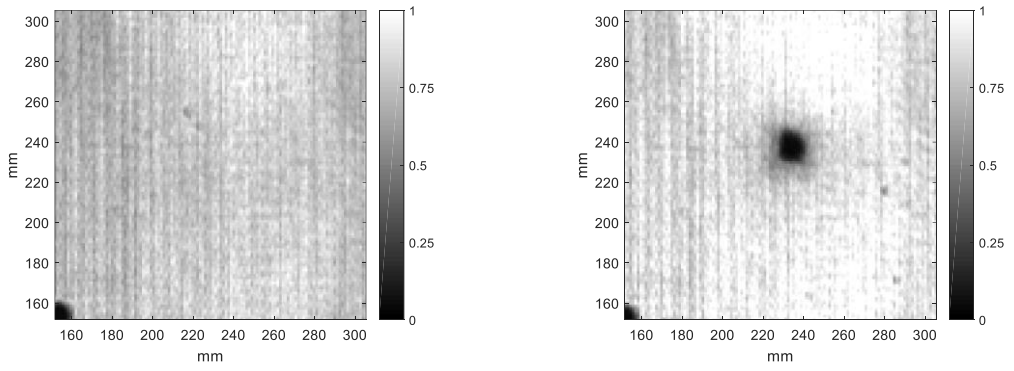

(a) (b)

Figure 48 – Panel C immersion double through-transmission peak amplitude C-scans of (a) baseline and (b) impact 1 damage.

5.3 Summary

A comprehensive examination of impact damage and panel quality was performed with conventional C-scans as commonly used in industry. Initial air-coupled through-transmission peak amplitude C-scans were performed on Panel B to directly estimate the 2-D shape and size of impact damage. Figure 44 shows the results from these scans, which revealed an approximately circular geometry of the impact damage with increasing radial size with each successive impact. The surrounding areas throughout the panel have non-uniform amplitudes which are visualized by the air C-scans. This is most likely attributed to the woven fibers of Panel B. Similar results are seen in Figure 45 after performing

immersion double through-transmission peak amplitude C-scans. For comparison, the immersion peak amplitude C-scans shown in Figure 46 from Panel C, which is made up of unidirectional fiber layers with alternating orientations to achieve an orthotropic layup, are much more consistent between each spatial point producing a higher quality image. The difference in the woven layers of Panel B and non-woven unidirectional layers of Panel C could be the cause of poor C-scan quality. Additionally, layer bonding could be affected by the type of fiber weave used causing additional scattering.

The differences between the panel made of woven fiber layers and unidirectional fiber layers is made even more clear when examining the pulse-echo data. Figure 45 and Figure 46 show a combination of A-scans, B-scans and C-scans for Panel B and Panel C, respectively. The measured pulse-echo data acquired perpendicular to the surface of Panel B and Panel C reveal the material layer bonding quality and the 3-D profile of the damage itself. The saturated signals acquired for Panel B were due to the highly attenuative material where equipment gain levels were set to resolve the back surface reflected waves within the A-scans. When making a direct comparison between scans of these two panels, the results from Panel B are of poor quality causing details such as the exact depth and shape of impact damage to be difficult to interpret. On the other hand, the data from Panel C is so well defined that individual panel layers can be resolved from the A-scans and B-scans as well as the more uniform peak amplitudes throughout the undamaged portions of the C-scan images.

6 SPARSE ARRAY IMAGING WITH ESTIMATED SCATTERING

Sparse array imaging is a valuable tool for assessing the existence and location of damage using attached sensors distributed on a structure. By applying baseline subtraction using data acquired before and after the introduction of damage, the scattered waves generated by Lamb waves interacting with the damage manifest themselves as echoes in the residual signals. Using known geometrical information about the sparse array configuration, arrival times of such echoes can be estimated for all assumed damage locations and, by applying imaging methods, images can be generated to help localize and characterize the damage. Some imaging methods use knowledge of expected scattering from damage for image improvement and considered here is the minimum variance imaging algorithm [83], [101]. Expected scattering can be directly incorporated into the imaging method using the 2-dimensional scattering matrices shown in sections 4.2.3.3 and 4.3.3.3.

6.1 Sparse Array Measurements

Sparse array measurements were performed on Panel B and Panel C by exciting each of the eight transducers individually and measuring waveform responses on all the other transducers. Considering reciprocity between source and receiver, this procedure results in 28 unique signal pairs for both panels. Data were taken using a NI PXIe-1082 chassis running custom LabVIEW software with a 14-bit arbitrary waveform generator (PXI-5412), a dual 8×1 multiplexer (PXI-2593), and a 14-bit digitizer (PXI-5122). A linear sine wave chirp from 40 to 150 kHz over 200 μs was produced by the waveform generator at 10 Vpp while the multiplexer configured the correct source and receiver based upon a predefined signal pair list. Each received signal was next amplified 41 dB and 25 dB for

Panel B and Panel C, respectively, by a Panametrics 5072PR pulser-receiver and digitized at a sampling rate of 20 MHz. Before any additional processing, signals were deconvolved to yield the equivalent response to a 3-cycle, 80 kHz tone burst [86].

In addition to acquiring sparse array data from Panel B and Panel C, data were acquired from another panel produced by Tencate and nominally identical to Panel C. This panel, which is referred to as Panel D, was instrumented with 6 transducers resulting in only 15 unique signal pairs. While the signal capturing process was the same between Panel D and the other panels, the parameters for the linear sine wave chirp were from 50 to 500 μs over the same time 200 μs window. The final received signals were amplified 28 dB and deconvolved to obtain the same 3-cycle, 80 kHz equivalent response used for Panel B and Panel C. Data were acquired before and after applying all three described artificial damage types and impact damage for Panel B and Panel C. Panel D was only evaluated using the aluminum disc artificial damage and two separate locations of impact damage. The aluminum disc and the method used to create impact damage were the same for all panels. The locations of damage were varied to evaluate the robustness of localization anywhere within the sparse array. To adhere the aluminum disc and copper pipe artificial damage, a strong shear wave couplant grease was used to effectively attach the damage without needing more permanent adhesion methods. Figure 49 shows all three panels with datasets acquired and damage locations summarized in Table 11.

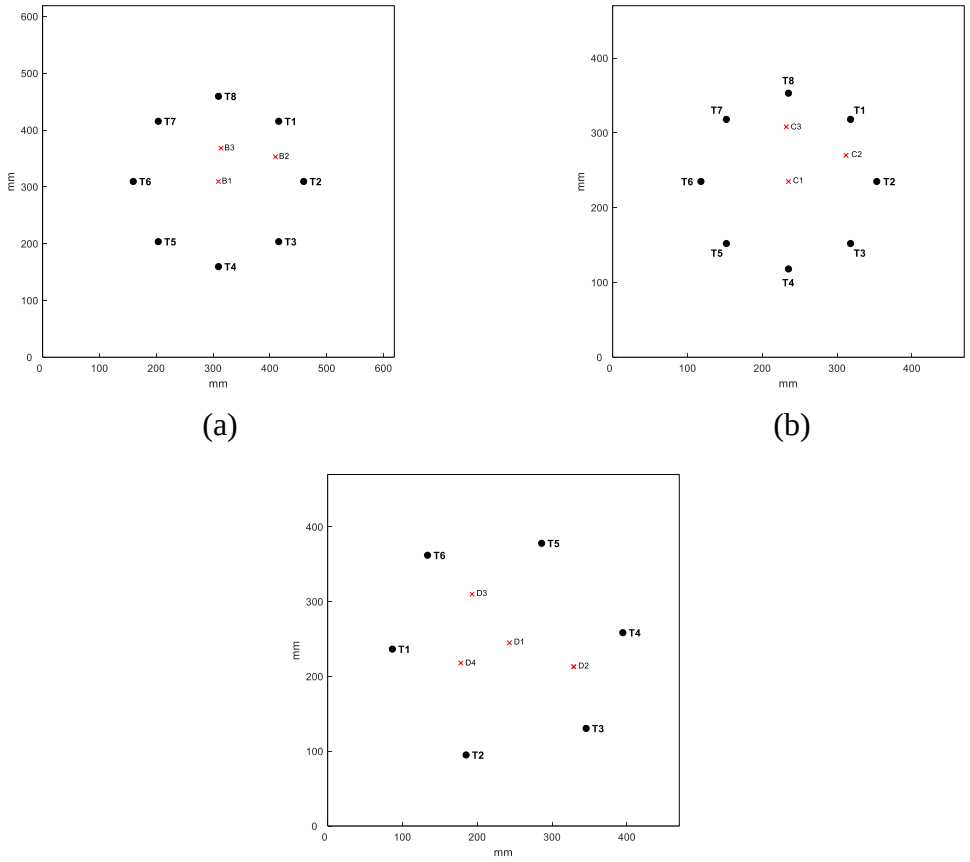

(a) (b)

(c)

Figure 49 – Layout of (a) Panel B, (b) Panel C, and (c) Panel D with attached transducers (black dots) and damage locations (red "x").

Table 11. Summary of sparse array datasets and damage locations

Datasets	Flaw	Damage Location
BA1 – BA3	Magnets	B1 – B3
BA4 – BA6	Al Disc	B1 – B3
BA7 – BA9	Cu Pipe	B1 – B3
CA1 – CA3	Magnets	C1 – C3
CA4 – CA6	Al Disc	C1 – C3
CA7 – CA9	Cu Pipe	C1 – C3
DA1 – DA3	Al Disc	D1 – D3
BI1 – BI4	Impact 1 – 4	B1
CI1	Impact 1	C1
DI1 –DI4	Impact 1 – 4	D1
DI5 –DI8	Impact 1 – 4	D4

6.2 Imaging Methods

Various methods have been developed to use sparse array data for guided wave imaging, but the most notable and well-known method was introduced by Wang *et al*. [82] in 2004. This technique, which performs synthetic time-reversal of the signals, is commonly referred to as delay-and-sum (DAS). While multiple variations of DAS exist [102], minimum variance (MV) imaging is applicable here because it utilizes *a priori* knowledge of damage scattering to improve damage detectability and image noise reduction. The MV algorithm was first applied to sparse array imaging by Hall and Michaels [83] where they detailed the approach and compared the performance of MV imaging to DAS.

6.2.1 Sparse Array Algorithms

Both DAS and MV imaging provide a value for each pixel in the image based on a weighted summation of the received signals at calculated points in time. The received signals are typically envelopes of the scattered residuals signals, which contain energy from the scatterer at a time τ, calculated as,

$$\tau_{ixy} = \frac{d_{ixy}}{c_g}, \tag{43}$$

for isotropic media. The transducer pair i and pixel coordinate (x,y), identified by subscripts xy, determine the total propagation distance from transmitter to pixel location to receiver, d_{ixy}. The group velocity, c_g, corresponds to the center frequency of the wave packet and is used to determine the arrival time. The pixel values for DAS imaging are defined as,

$$P_{xy} = \sum_{i=1}^{N} \left| \mathrm{w}_{ixy} r_i(\tau_{ixy}) \right|^2 , \tag{44}$$

where $r_i(t)$ is the residual signal for the *i*th transducer pair and w_{ixy} is a weighting coefficient that could be specific to the transducer pair and pixel location. For simplicity, the pixel value can be rewritten in vector notation as,

$$P_{xy} = \vec{\mathbf{w}}_{xy}^{\mathrm{H}} \mathbf{R}_{xy} \vec{\mathbf{w}}_{xy} , \tag{45}$$

where $\mathbf{R}_{xy} = \vec{\mathbf{r}}_{xy} \vec{\mathbf{r}}_{xy}^{\mathrm{H}}$ and $\vec{\mathbf{w}}_{xy}$ is a vector containing all weighting coefficients, w_{ixy}, for that pixel location. The measurement vector is,

$$\vec{\mathbf{r}}_{xy} = \left[r_1(\tau_{1xy}) \quad \dots \quad r_N(\tau_{Nxy}) \right]^{\mathrm{T}} . \tag{46}$$

For DAS imaging, all weights are typically set to unity.

For MV imaging, the weights are determined differently. Let $\vec{\mathbf{e}}_{xy}$ be a unit vector whose elements are proportional to the expected amplitudes for each receiver if damage is present at pixel location *xy*:

$$\vec{\mathbf{e}}_{xy} \sim \left[\frac{\psi_{1xy}}{\sqrt{d_{1xy}^{\times}}} \quad \frac{\psi_{2xy}}{\sqrt{d_{2xy}^{\times}}} \quad \dots \quad \frac{\psi_{Nxy}}{\sqrt{d_{Nxy}^{\times}}} \right]^{\mathrm{T}} . \tag{47}$$

In this equation, $d_{ixy}^{\times}$ is the product of the distances from transmitter to pixel location and pixel location to receiver and ψ_{ixy} is a scattering coefficient for a defect at *xy* for the *i*th transducer pair. The denominator accounts for cylindrical spreading loss whereas the numerator accounts for non-uniform scattering. The weight vector is calculated such that

the pixel value is minimized subject to a constraint that preserves the pixel value at damage locations,

$$\vec{\mathbf{w}}_{xy}^{\mathrm{MV}} = \arg\min_{\vec{\mathbf{w}}} \vec{\mathbf{w}}^{\mathrm{H}} \mathbf{R}_{xy} \vec{\mathbf{w}} \qquad \text{such that } \vec{\mathbf{w}}^{\mathrm{H}} \vec{\mathbf{e}}_{xy} = 1. \tag{48}$$

The weights that satisfy this constraint are,

$$\vec{\mathbf{w}}_{xy}^{\mathrm{MV}} = \frac{\mathbf{R}_{xy}^{-1} \vec{\mathbf{e}}_{xy}}{\vec{\mathbf{e}}_{xy}^{\mathrm{H}} \mathbf{R}_{xy}^{-1} \vec{\mathbf{e}}_{xy}} . \tag{49}$$

6.2.2 Minimum Variance for Anisotropic Media

Previous work has been reported for the application of MV imaging to artificial damage in a quasi-isotropic composite plate [84]. Simple characterization of scattering from a through-hole was used to evaluate performance and the results showed marked improvement compared to the DAS elliptical imaging method [82]. While the imaging improvement was notable, a single direction-independent group velocity estimated directly from the sparse array data was applied for all propagation directions. This velocity, c_g in Equation (43), is used to calculate time shifts for back-propagating all transducers pair signals and aligning scattered echo arrivals. However, composites have direction-dependent group velocities, even those with quasi-isotropic fiber layups. Variations in group velocity can impact accurately determining echo arrival times, especially when the velocity variations or propagation distances are significant. To account for these variations, the anisotropic group velocity profiles estimated in Sections 3.4 and 3.5 are incorporated into the minimum variance algorithm by replacing Equation (43) with,

$$\tau_{ixy} = \frac{d_{itxy}}{c_g(\theta_{inc})} + \frac{d_{irxy}}{c_g(\theta_{scat})}, \tag{50}$$

where the group velocity $c_g(\theta)$ is now angularly-dependent on the incident and scattered wave propagation angles, θ_{inc} and θ_{scat}, respectively. The propagation distances d_{itxy} and d_{irxy} refer to the distances from transmitter to scatterer edge and scatterer edge to receiver at location (x, y), respectively, for the corresponding propagation angles.

In addition to including anisotropic group velocity into the imaging algorithm, it is believed that the non-point-like scattering effect described in Section 4.1.3 could be used to better estimate arrival times of defect-scattered echoes. This is illustrated best by Figure 50 where three circular residual wavefields show scattering from an aluminum disc with a 10 mm radius in Panel B; waves are incident at 0° from transducer T6. They are overlaid with scattered wave time arrivals estimated using Equation (28), which incorporates the radial size of the damage via ray tracing. Three separate radial sizes, 5 mm, 10 mm, and 20 mm, were used to estimate the arrival times and are shown as solid green lines with the expected wave packet width bracketed by red dashed lines. Figure 50(a) and 50(c) clearly indicate poor estimation of the wave packet arrival for non-forward scattered waves where Figure 50(b) shows how using the known radius of the damage improves the direct estimation of scattered wave arrivals for all angular directions. This same principal is implemented into the imaging algorithm to adjust propagation distances based on an assumed defect geometry; i.e., circular. The radii for all damage types are chosen based on their actual outer diameter for artificial damage or measured approximate diameter for impact damage.

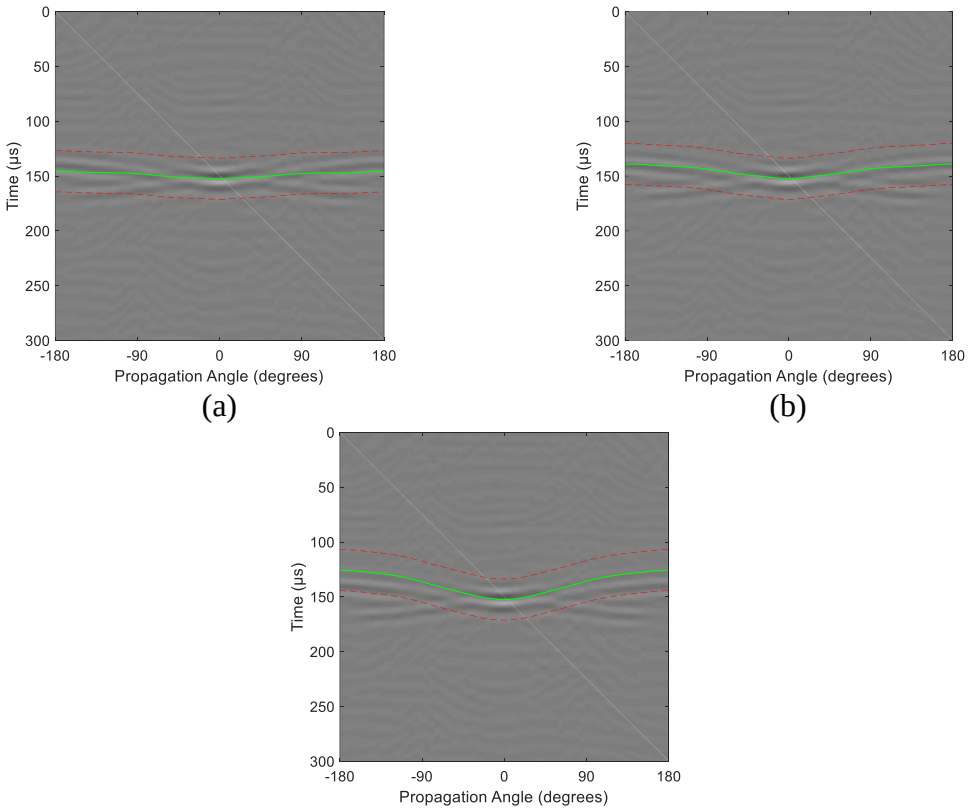

Figure 50 – Circular residual wavefields from Panel B showing scattered wave packet from a 10 mm radius aluminum disc. Estimated time arrivals of scattered wave packet using an assumed damage radius of (a) 5 mm, (b) 10 mm, and (c) 20 mm are shown as solid green lines with the packet width of 37.5 μs outlined by red dashed lines.

6.3 Imaging Results

Five separate cases as described in Table 12 were used to produce images for Panel B, Panel C, and Panel D; three separate damage locations were considered for each panel. The images are shown in Figure 51-Figure 61. They were all produced using minimum variance imaging and are displayed on a 20-dB log scale normalized to the maximum amplitude of each image. Each separate case can be evaluated and compared visually from the images produced.

Table 12. Cases used to produce sparse array images for each panel and damage type

Case	Scattering Matrix	Radial Geometry Compensation	Anisotropic Velocity Compensation
1	Uniform	-	-
2	Estimated Matrix	-	-
3	Estimated Matrix	✓	-
4	Estimated Matrix	-	✓
5	Estimated Matrix	✓	✓

Figure 51-Figure 54 show the results of imaging each damage type for each of the five cases. For the artificial damage, images are shown for three damage locations whereas for impact damage, they are shown for three impact levels. For all images, the estimated damage location (i.e., the location of the peak amplitude pixel) is indicated by a white star within the image while the known location of damage is indicated by a white triangle. Three criteria are used to assess imaging improvement: peak amplitude of the image, the accuracy of the peak amplitude location relative to the known damage location, and overall image noise reduction. The peak amplitude of each image, in addition to noise reduction, is used as a relative measure of certainty for damage detection. With a larger peak amplitude, a higher level of certainty can be attributed to the expected presence of damage. Additionally, the localization of damage is evaluated by comparing the peak amplitude location with the known coordinates of the damage. The overall image quality must also be considered as it can be more difficult to assign confidence to the peak amplitude and localization performance evaluation criteria with noisier images.

Several observations can be made from images produced with Panel B data for artificial damage (Figure 51-Figure 53). The overall noise is significantly reduced when

using the estimated scattering matrix. Application of the radial geometry compensation showed additional improvement as well, although it was slight for each artificial damage type. Another noticeable improvement that the peak amplitude levels increased by 5-15 dB after applying the estimated scattering matrix. With the significant noise reduction and increase of peak amplitude levels, a higher level of confidence can be obtained when using scattering estimates for the damage being evaluated. The localization performance is good for all five imaging cases although using the estimated scattering matrix offers a small but noted improvement. Anisotropy correction seemed unnecessary in most cases where almost no visible performance changes were observed.

For the images obtained with Panel B data for impact damage (Figure 54), using a uniform scattering assumption was completely ineffective with no clear detection of damage within the panel. After applying the estimated scattering matrix and additional compensation methods, the existence of damage becomes increasingly more visible as the size of the impact damage increases; however, the images themselves still contain considerable noise, which affects the overall visibility and quantification of the damage location. The overall peak amplitudes increase approximately 1-2 dB, but the locations of the peaks are not near the known damage location but instead are at a transducer location. These mis-located peaks indicate imperfect baseline subtraction of the direct arrivals that cause high amplitude artifacts near the transducer locations.

Similar results to Panel B in Figure 55-Figure 57 for artificial damage were observed from Panel C data when including the estimated scattering and additional compensation methods. The use of estimated scattering matrices had the most significant improvement while the radial geometry only made slight improvements in overall noise and anisotropic

compensation showed no measurable performance changes. The biggest improvement was seen in Figure 58 when applied to impact damage. The uniform scattering assumption was unable to locate or detect the existing of impact damage; however, application of the estimated scattering matrix accurately detected the existence of damage and reduced overall noise within the image. Panel D results (Figure 59-Figure 61) showed even better improvement in imaging performance when going from uniform to estimated scattering. For both artificial and impact damage, damage detection did not perform well under the uniform scattering assumption with only one instance where the peak amplitude location matched the known damage location at D3 for the aluminum disc damage type. However, applying the estimated scattering matrix made very significant improvements in noise level, peak amplitudes, and location accuracy.

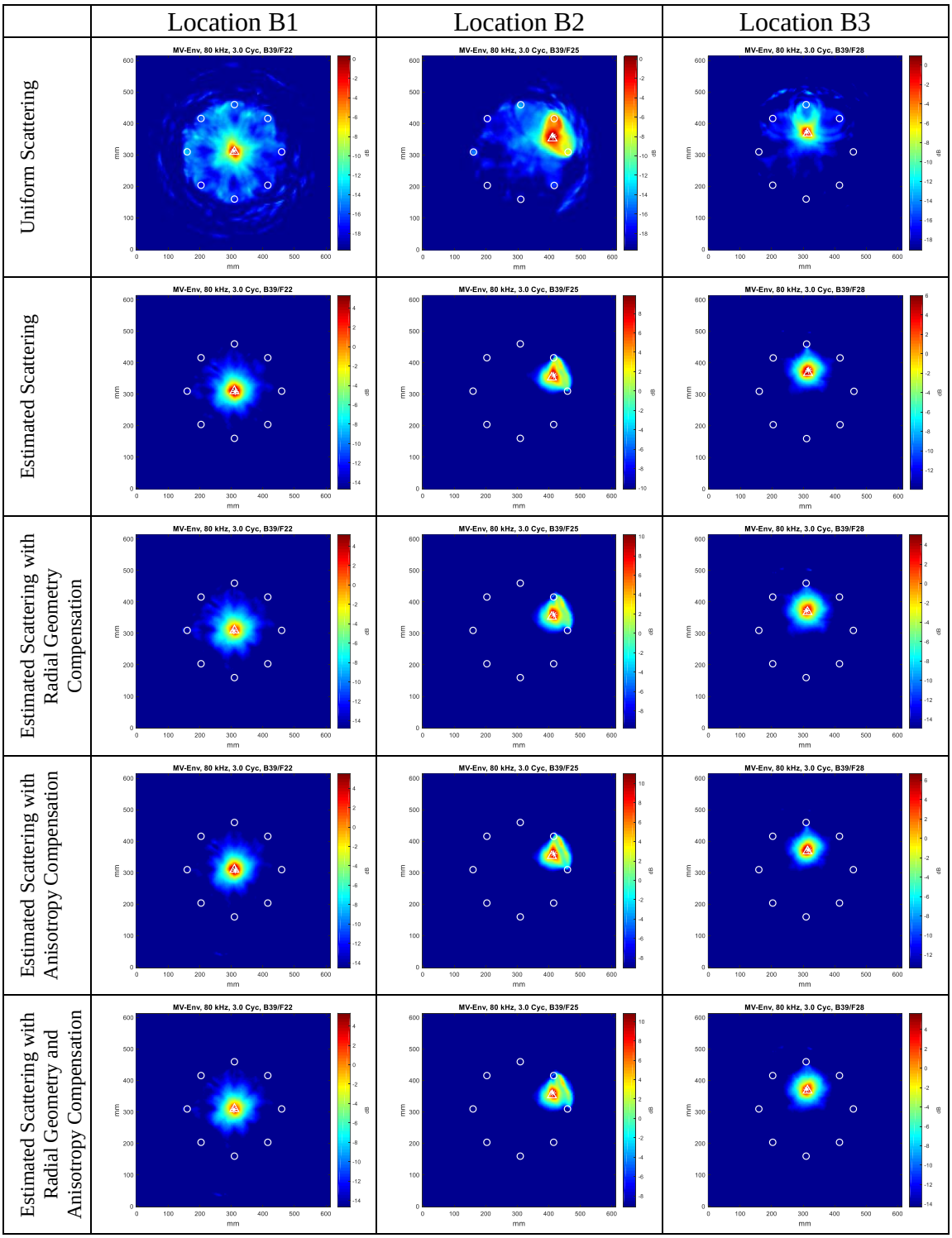

Figure 51 – Minimum Variance imaging of Panel B with magnet stacks as artificial damage.

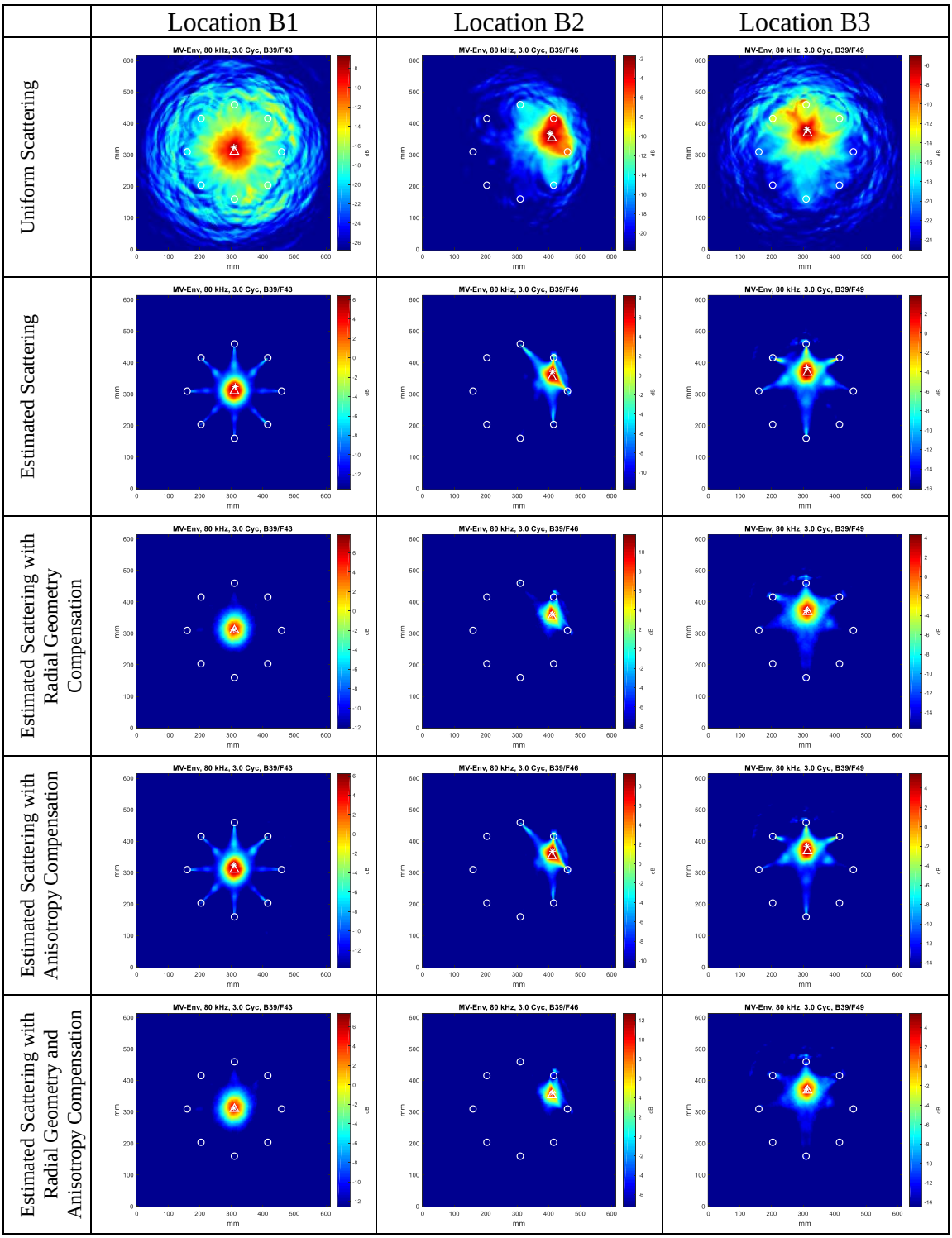

Figure 52 – Minimum Variance imaging of Panel B with aluminum disc as artificial damage.

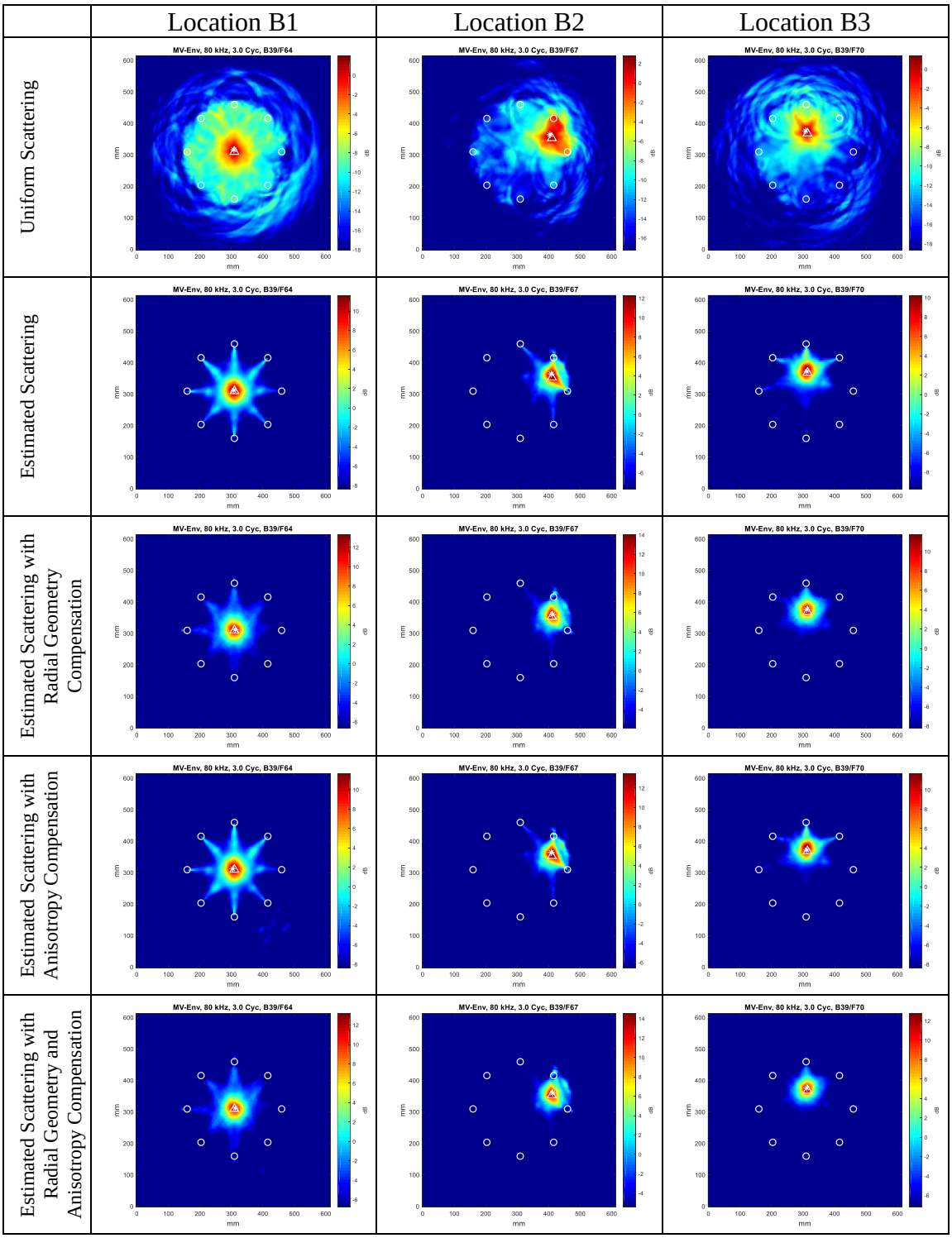

Figure 53 – Minimum Variance imaging of Panel B with copper pipe as artificial damage.

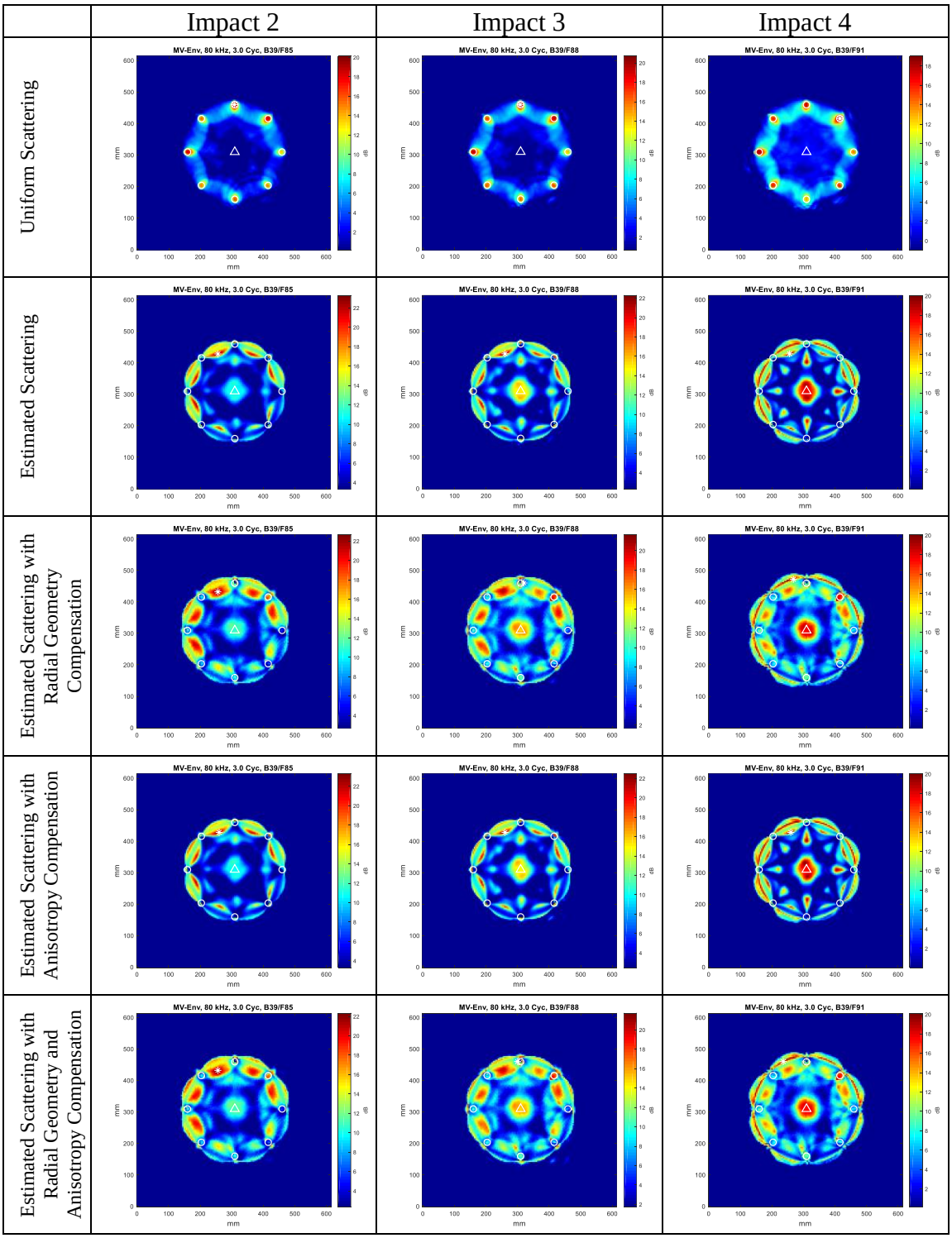

Figure 54 – Minimum Variance imaging of Panel B with all levels of impact damage.

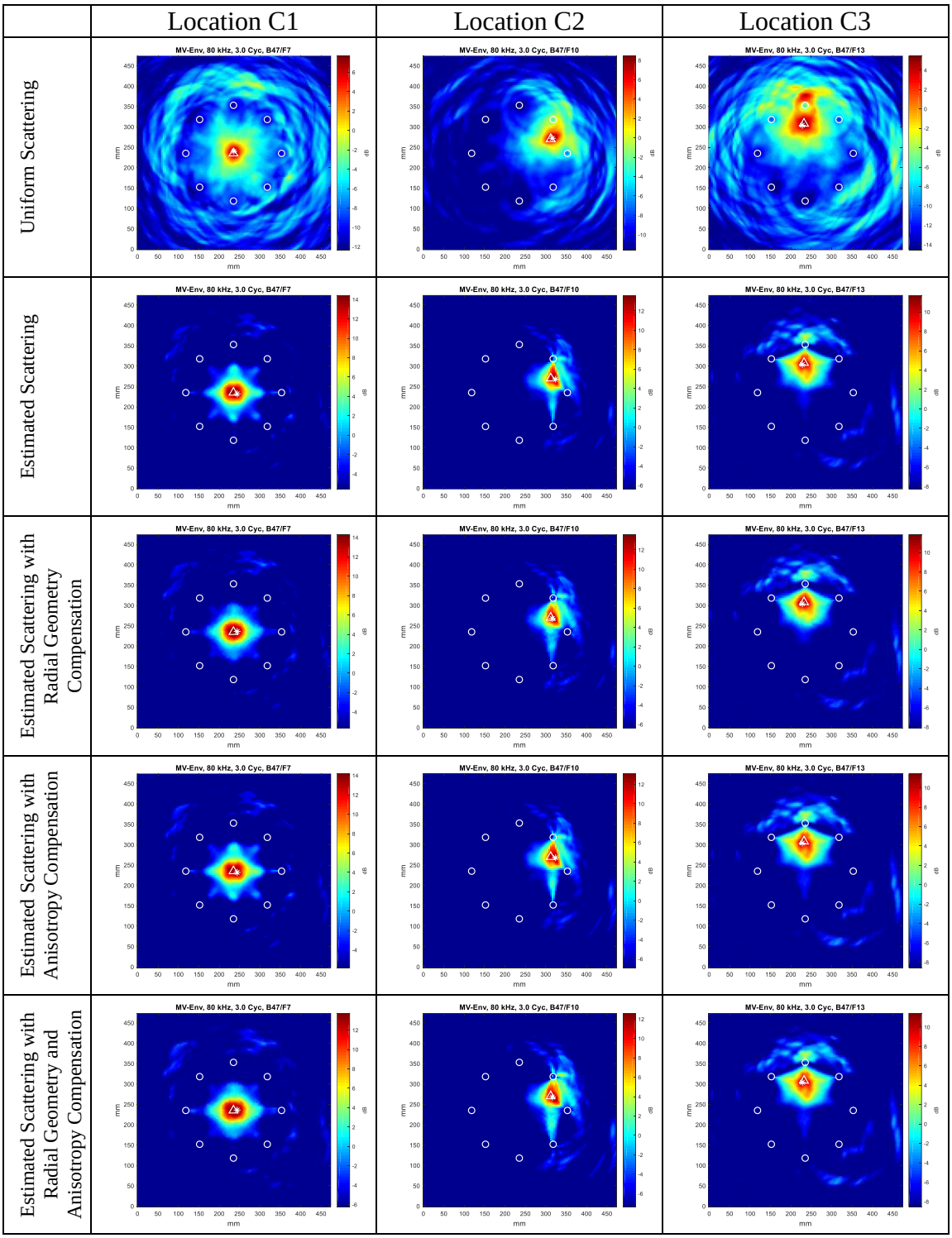

Figure 55 – Minimum Variance imaging of Panel C with magnet stacks as artificial damage.

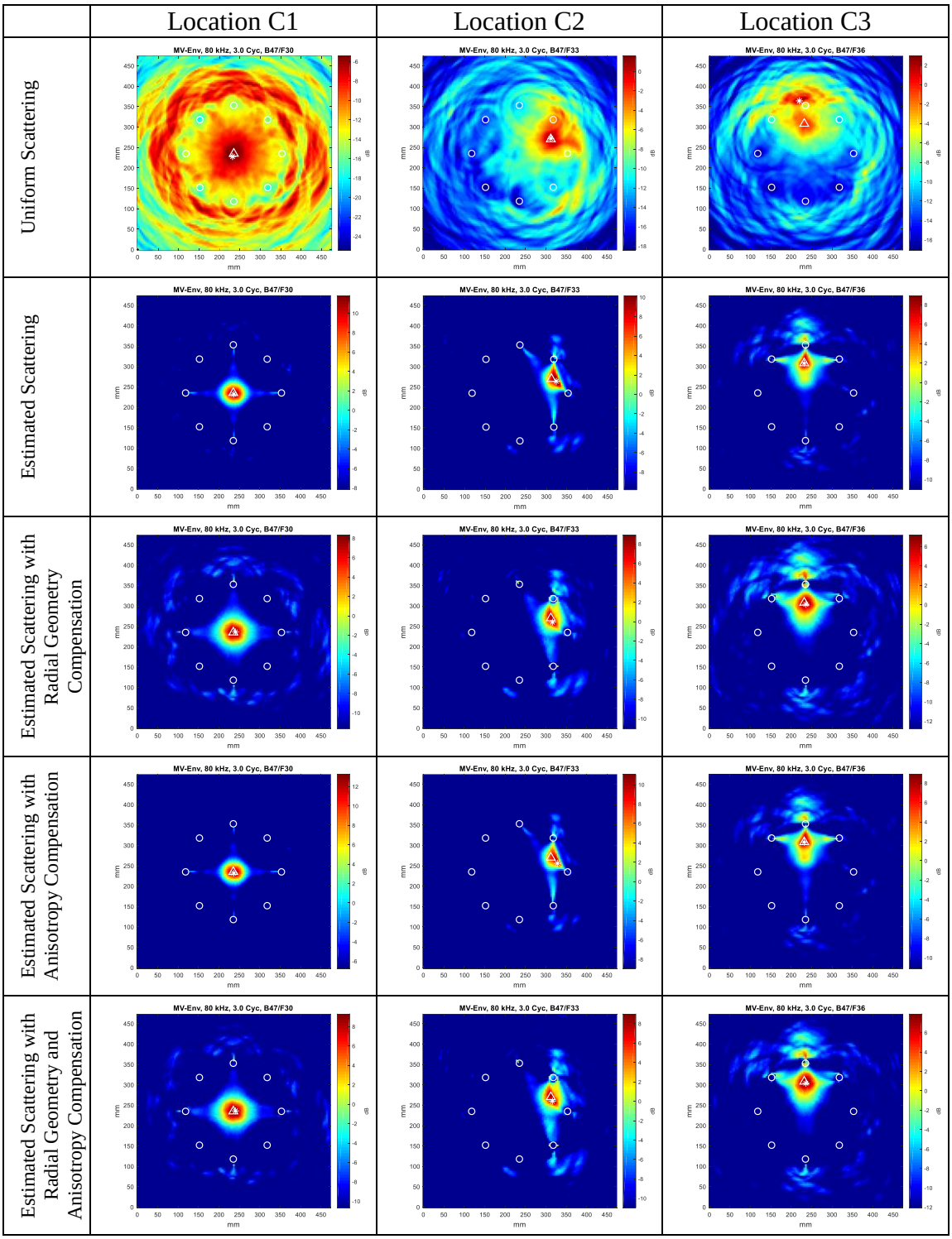

Figure 56 – Minimum Variance imaging of Panel C with aluminum disc as artificial damage.

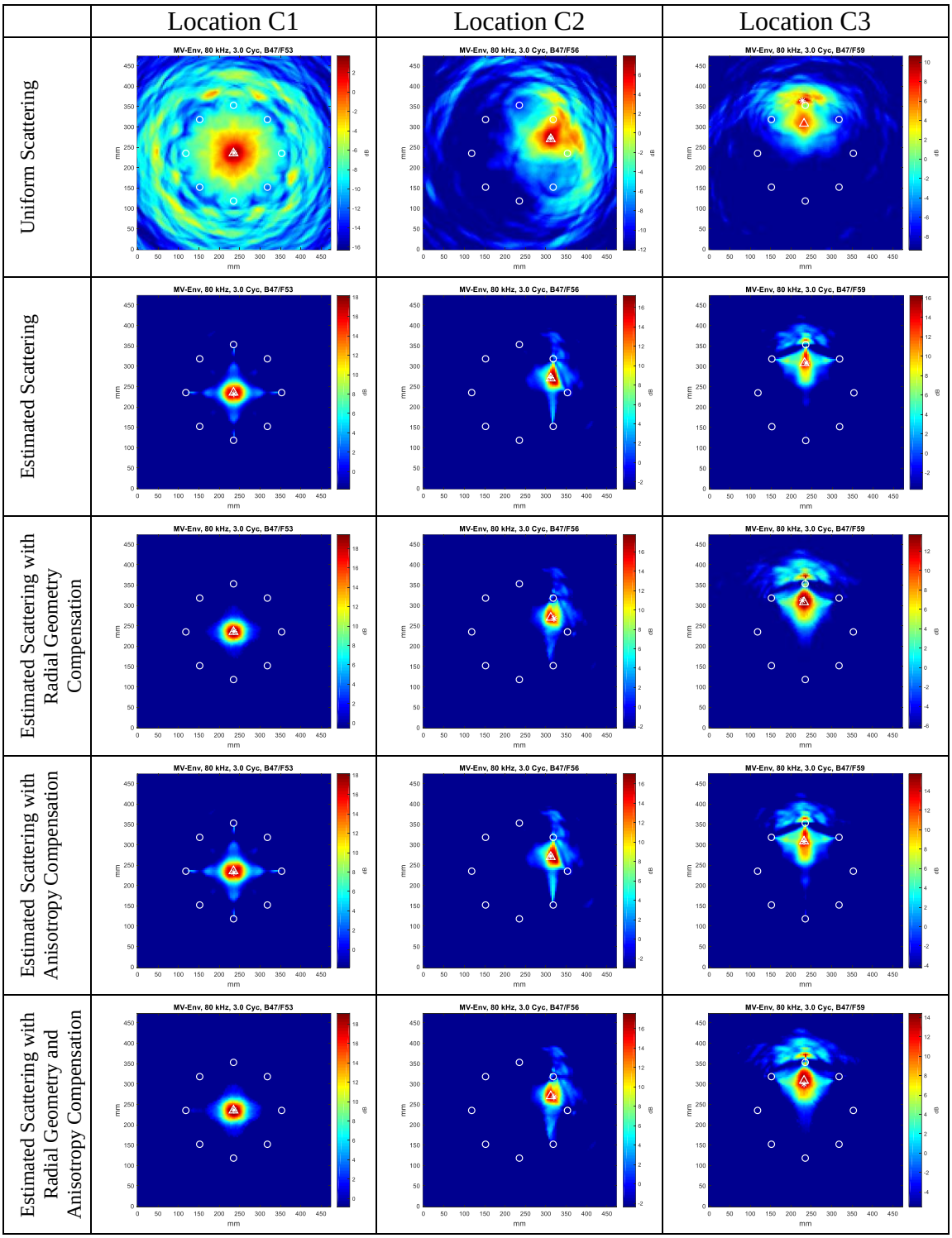

Figure 57 – Minimum Variance imaging of Panel C with copper pipe as artificial damage.

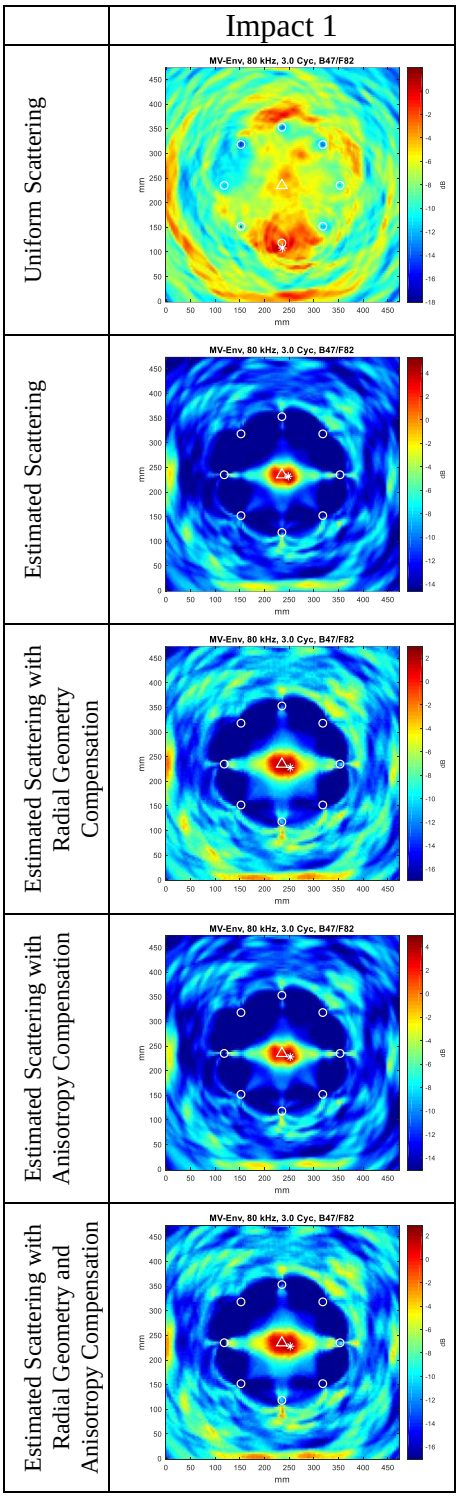

Figure 58 – Minimum Variance imaging of Panel C of impact damage.

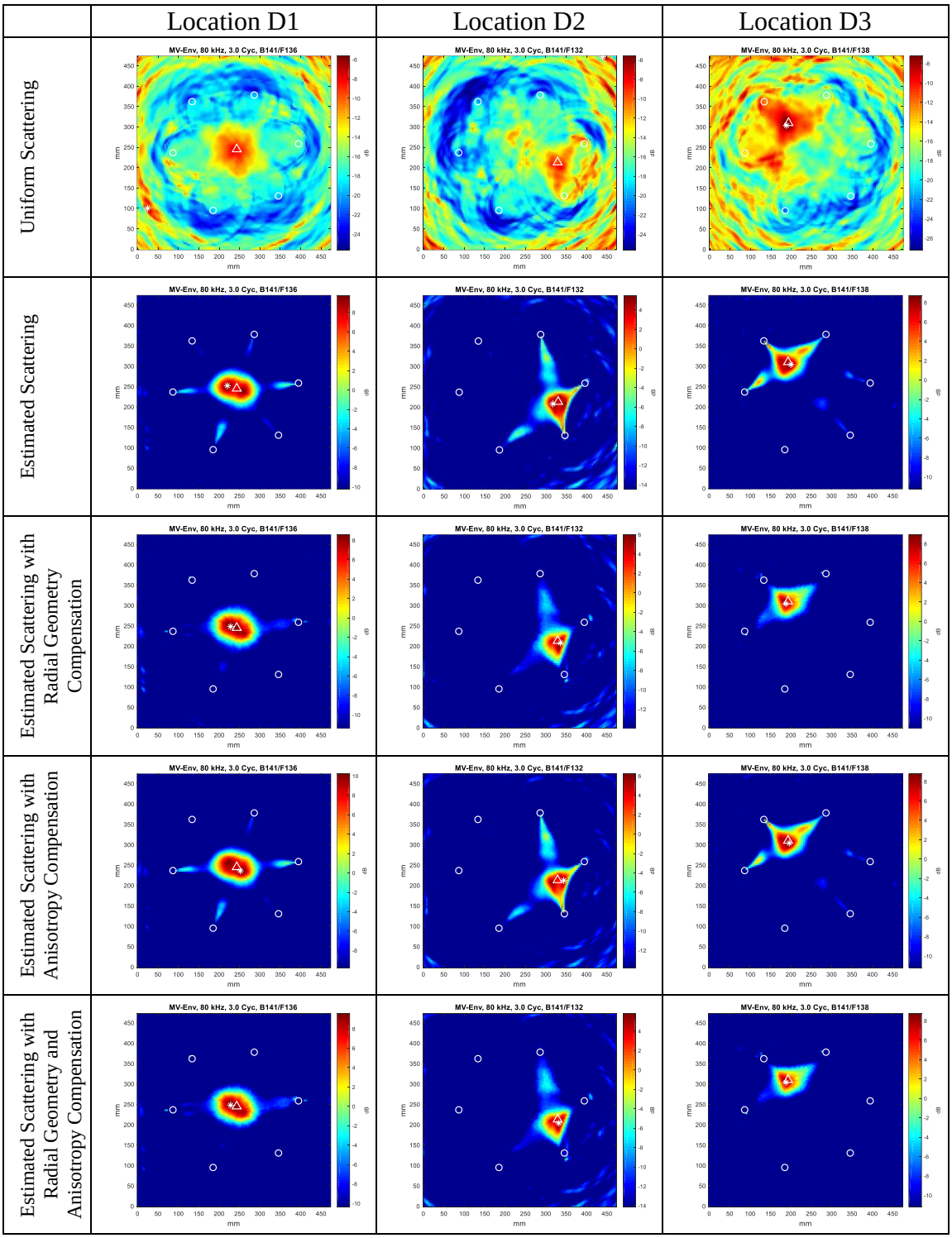

Figure 59 – Minimum Variance imaging of Panel D with aluminum disc as artificial damage.

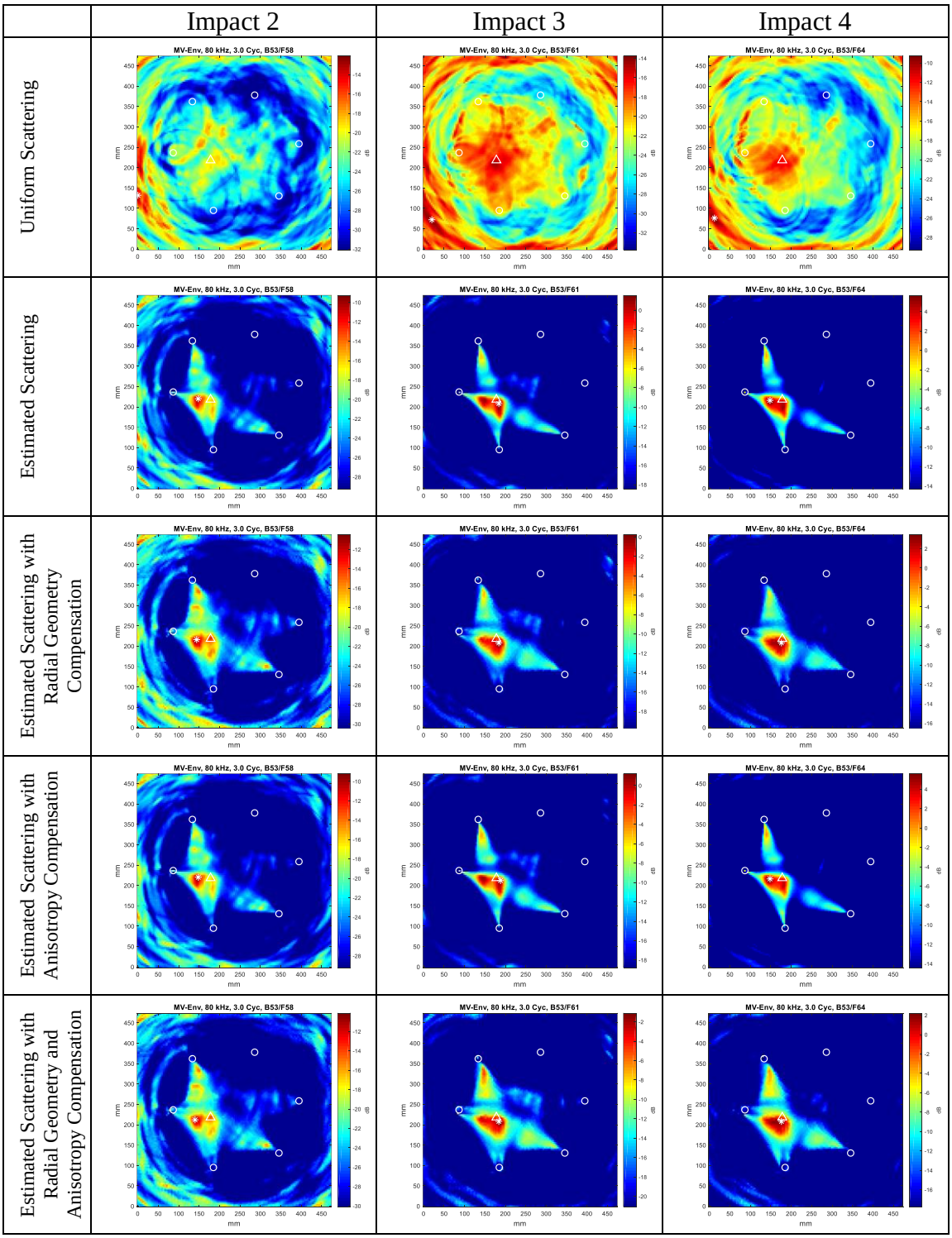

Figure 60 – Minimum Variance imaging of Panel D with all levels of impact damage for location DI1.

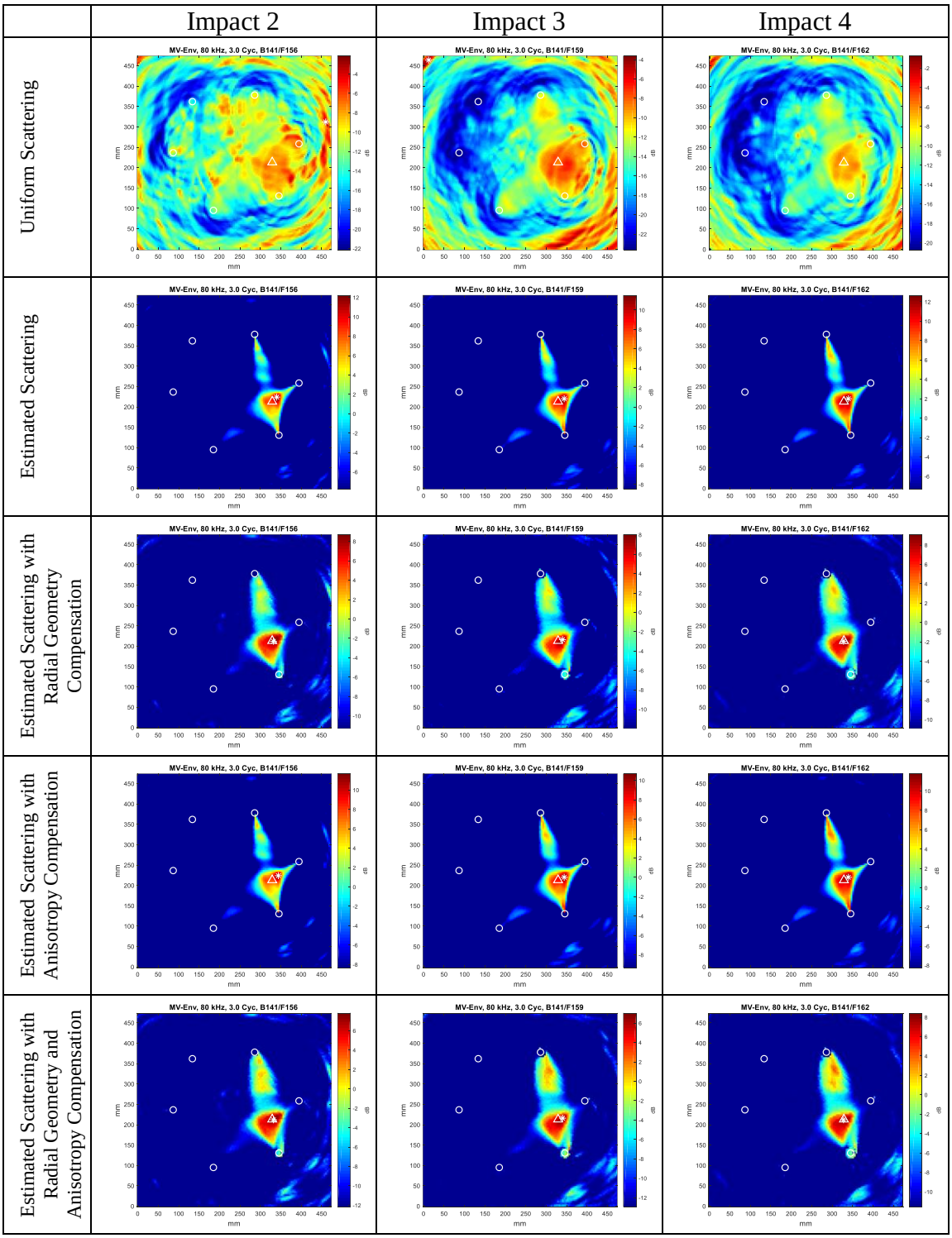

Figure 61 – Minimum Variance imaging of Panel D with all levels of impact damage for location DI2.

The influence of the damage radius estimate on MV imaging is examined by varying the assumed radius to see how imaging performance is affected. Figure 62 shows three sparse array images of the aluminum disc produced with the MV algorithm using three different damage radius assumptions of 5 mm, 10 mm, and 20 mm. No anisotropy corrections were made. Figure 62(a) and 62(c) are MV images made with the assumed radius below and above the known damage radius whereas Figure 62(b) is produced using the correct radius of 10 mm. Two improvements can be seen when incorporating an accurate radius of the damage size. One, the noise in the image is reduced for the correct 10 mm radius estimate while the 5 mm and 20 mm estimates have increased noise and slightly worse localization of the damage's center. Two, the peak amplitude level is improved when using the correct radial estimate.

Marked improvement of the peak amplitude levels are further illustrated in Figure 63 where an estimate of the damage radius was varied from 0 to 20 mm and the peak amplitude levels within the MV images were recorded. A maximum can be seen at the 10 mm radius estimate, which corresponds exactly with the known damage radial size. There is almost a 4 dB increase between the image produced without incorporating an estimate of the damage radius (i.e., point scatterer assumption) and the image produced with a 10 mm estimate of the damage radius.

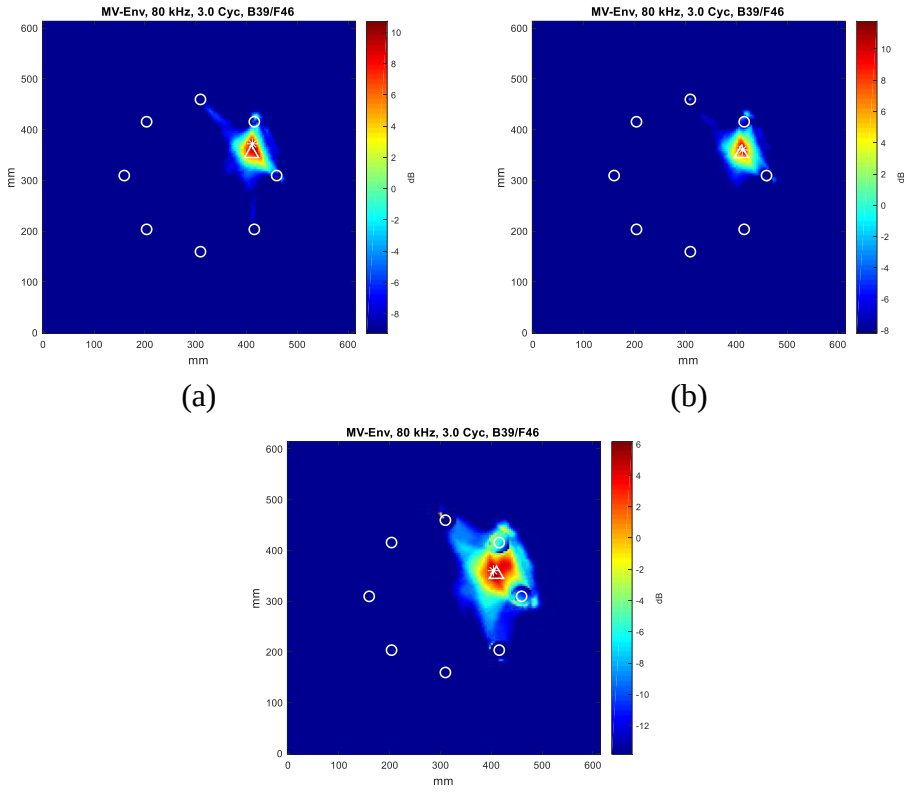

Figure 62 – Minimum Variance imaging of Panel B with aluminum disc as artificial damage at location B2 with a damage radius assumption of (a) 5 mm, (b) 10 mm and (c) 20 mm.

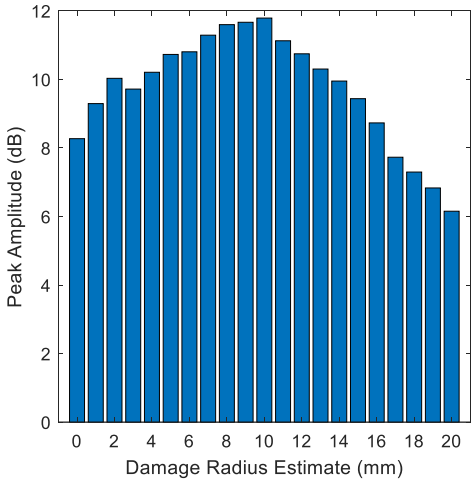

Figure 63 – Peak amplitude levels of Minimum Variance images produced from Panel B sparse array data with aluminum disc as artificial damage at location B2.

6.4 Summary

Sparse array imaging is performed on three separate panels with two different fiber layups using both artificial and real impact damage. The MV method is used because of its ability to incorporate *a priori* information from these specific damage types. This information is provided through a scattering matrix specific to the damage and is compared against a uniform scattering assumption. Additionally, enhancements are made to the MV algorithm to include angular-dependent group velocities and a ray tracing model that accounts for the size of expected damage. All these cases are evaluated by visually comparing images based on overall image noise reduction, damage detection, damage localization, and peak amplitudes within the image, all of which provide a level of confidence for detecting and localizing damage.

Images produced using the uniform scattering matrix showed reasonable detection of the artificial damage for all three examined panels. Localization of damage also performed well as the estimated damage locations are in good agreement with their known locations. However, noise is prevalent for these images, which can introduce uncertainty in localizing the damage when there is no prior knowledge of the damage location. A comparison between the images produced with the uniform scattering matrix and those produced with the damage specific estimated scattering matrix showed both a meaningful increase in the peak amplitude levels as well as a significant reduction to image noise. Both were achieved all while maintaining the same if not better detection and localization performance.

In the case of impact damage, MV imaging for both the orthotropic and quasi-isotropic panels was unable to detect damage assuming no prior knowledge of expected scattering. After including the estimated scattering information specific to each damage case, imaging performance improved by reducing overall image noise and providing a reasonable damage location estimate. However, imaging of damage located in the center of the array for both the quasi-isotropic and orthotropic layups saw the smallest improvements. While several factors were present such as imperfect baseline subtraction and relatively low scattering amplitudes, one of the largest contributing factors to the poor performance of imaging impact damage is the non-ideal symmetrical transducer array used. Since the impact damage only exhibited forward scattering, only the transducer pairs that detect forward incident wave scattering are useful. This decrease in effective transducer pairs reduces the efficacy of the imaging and demonstrates that array geometry is an important factor to consider for improving imaging performance.

Additional results were produced using direction-dependent group velocities. Minimal to no improvement was observed when incorporating the panel-specific direction-dependent group velocities. While this is contrary to what was expected, it is believed that the small variation in group velocity had little effect on wave arrival times due to the smaller propagation distances examined. It is still believed that MV imaging over much larger distances or imaging of composite materials that have stronger anisotropic wave propagation effects can be significantly improved with accurate group velocity characterization.

In most cases, the radial geometric scattering model showed slightly better localization of artificial damage except for the aluminum disc images from Panel C. This performance

is further validated from the results in Figure 62 and Figure 63 where using an accurate estimated radius in the MV imaging method reduced noise and increased the peak amplitude levels at the estimated damage location. The peak amplitude levels are directly correlated to how closely the damage radius estimate is to the actual damage. When applied to impact damage, the results were slightly worse from those produced using estimated scattering only. This most likely indicates that the geometric scattering model used did not accurately represent the scattering observed from the impact damage.

7 CONCLUSION AND RECOMMENDATIONS

7.1 Conclusions

This thesis describes experimental procedures and signal processing methodologies to acquire and analyze ultrasonic wavefield data to ultimately determine 2-D scattering from damage for anisotropic media. This type of damage characterization is useful for imaging techniques that can incorporate *a priori* scattering assumptions.

Initial characterization of anisotropic wave propagation was performed. It was demonstrated that directional-dependent guided wave propagation for anisotropic composite panels consisting of a quasi-isotropic and orthotropic fiber layup affect both wave velocities and attenuation caused by additional material dampening. Overall, the wave propagation from panels examined had relatively low anisotropy characteristics but the results gave insight into how wave energy can concentrate along axial fiber directions, affecting wave propagation velocities and wave attenuation.

A methodology for extracting scattered waves from full wavefield data in the presence of interfering waves and signal noise was presented. Through a combination of baseline subtraction, spatial windowing, and frequency-wavenumber filtering, scattered waves from both artificial and impact damage were shown to be adequately isolated for estimating scattering patterns. It was shown that the point-like scattering approximation commonly used for artificial damage of a non-zero radius was poor and that scattering could be visually seen reflecting from both the edges of disc-like damage. A simple ray

tracing method was developed to incorporate the actual geometry and was shown to improve estimating the times of scattered wave arrivals.

The 2-D scattering from the artificial and impact damage cases examined were shown to vary overall in shape and size but were predominately affected by the incident angle of the propagating wave with respect to the composite panel fiber layup. Regarding artificial damage, the quasi-isotropic panel had minimal variations with respect to incident angle where large amplitude forward scattering and reduced amplitude backward scattering was observed. In contrast, the orthotropic panel showed clear evidence that scattering was strongly dominated by the primary fiber directions of 0° and 90°, which resulted in larger variations in scattering patterns for different angles of incidence. Impact damage, however, showed almost no details in the scattering patterns and was exclusively forward scattering in-line with the incident wave direction. Additionally, a method for generating 2-D scattering matrices from sparse incident angle, high-resolution scattering data was developed. This method leverages signal reciprocity to improve matrix density before Fourier fitting data to fill all matrix rows and columns.

Ultrasonic characterization of impact damage for both quasi-isotropic and orthotropic panel layups was performed using several industry standard techniques including through-transmission and pulse-echo C-scans. The results revealed impact damage sizing and layer depth of the delamination, which can be correlated with impact energy for the composite panels examined. The impact damage examined seemed atypical for layer disbonding and was more indicative of fiber breakage and epoxy cracking. This ultimately could have influenced the scattering results observed and could explain why little or no measurable back scattering occurred from any impact damage case examined. A comparison was

made between the quasi-isotropic panel and the aerospace quality orthotropic panel where a clear difference in panel quality was observed.

The estimated 2-D scattering matrices were incorporated into the MV imaging algorithm and applied to sparse array data acquired from both the quasi-isotropic and the orthotropic panel. An additional orthotropic panel containing impact damage from a previous study was used to further verify the improvements made to damage localization and noise reduction by incorporating damage-specific scattering data. The results overall showed marked improvement over using a uniform scattering assumption. Anisotropic wave velocity and the ray tracing model developed for better estimating scattered wave arrival times were implemented into the MV imaging method where only small improvements to noise reduction and/or localization were evident. This is most likely due to the minimal anisotropic wave propagation effects in the panels coupled with the small propagation distances considered.

7.2 Recommendations for Future Work

The work outlined here has demonstrated the ability to systematically and robustly estimate scattering. The estimated scattering can be directly applied to *in situ* sparse array imaging methods that can incorporate *a priori* information. Additionally, further evaluations were performed to characterize specific wave propagation properties of an anisotropic material, which can be used to more accurately estimate scattering patterns. Although feasibility of estimating scattering in composites was demonstrated, it cannot yet be directly applied for practical SHM in-field usage without additional work.

First, wave propagation characterization of anisotropic composites has been a main focal point of this work and key to improving scattering estimation of real impact damage. The proposed methodology for estimating these properties should be applied to a larger variety of composites with more pronounced anisotropy for investigating the various layups affect overall scattering from damage.

Second, more experimental data should be gathered to better characterize impact damage scattering. As evident by the UT inspection performed in this thesis, the generated impact damage was not typical, and the quasi-isotropic panel was of poor quality. Alternative methods to producing between-layer delaminations or disbonds should be considered so that the impact damage examined more accurately represents damage that is seen in the field.

Third, the amplitude attenuation characterized here is not incorporated into estimating scattering or used to improve MV imaging performance. Currently, the estimated scattering presented contains the amplitude attenuation associated with the direction of scattering. To incorporate amplitude attenuation into MV imaging, amplitude attenuation must be removed from the estimated scattering patterns and added to the propagation model used for imaging.

Fourth, array geometry is suspected to have been a factor in imaging performance, especially with a uniformly distributed array with damage in the center. Studies regarding array geometry, size and number of elements have been investigated in isotropic aluminum plates [103] but further studies should be performed for composite materials to determine optimum array configurations for detecting and locating impact damage.

Finally, a more advanced ray tracing model for determining scattering direction could be developed to improve estimated scattered arrivals which can be applied to non-circular defect/damage types (i.e., elliptical and irregular edge geometries), which would additionally be used to improve sparse array imaging.

REFERENCES

[1] P. J. Shull, *Nondestructive Evaluation: Theory, Techniques, and Applications*. CRC Press, 2002.

[2] V. Giurgiutiu, *Structural Health Monitoring with Piezoelectric Wafer Active Sensors*. Burlington: Academic Press, 2008.

[3] C. S. Byington, P. W. Kalgren, B. K. Dunkin, and B. P. Donovan, "Advanced diagnostic/prognostic reasoning and evidence transformation techniques for improved avionics maintenance," *IEEE Aerospace Conference Proceedings*, vol. 5, pp. 3424-3434, 2004.

[4] V. Giurgiutiu, A. Zagrai, and J. J. Bao, "Piezoelectric wafer embedded active sensors for aging aircraft structural health monitoring," *Structural Health Monitoring*, vol. 1, pp. 41-61, 2002.

[5] J. L. Rose, *Ultrasonic Guided Waves in Solid Media*. New York: Cambridge University Press, 2014.

[6] A. H. Nayfeh and D. E. Chimenti, “Free wave propagation in plates of general anisotropic media,” *Journal of Applied Mechanics*, vol. 56, pp. 881-886, 1989.

[7] Y. Li and R. B. Thompson, “Influence of anisotropy on the dispersion characteristics of guided utrasonic plate modes,” *Journal of the Acoustical Society of America*, vol. 87, pp. 1911-1931, 1990.

[8] H. Lamb, "On waves in an elastic plate," *Proceedings of the Royal Society of London. Series A*, vol. 93, no. 648, pp. 114-128, 1917.

[9] J. W. Strutt, "On waves propagated along the plane surface of an elastic solid," *Proceedings of the London Mathematical Society*, vol. 1, no. 1, pp. 4-11, 1885.

[10] A. E. H. Love, *Some Problems of Geodynamics: Being an Essay to which the Adams Prize in the University of Cambridge was Adjudged in 1911*. CUP Archive, 1967.

[11] R. Stonley, "Elastic waves at the surface of separation of two solids," *Proceedings of the Royal Society of London. Series A, Containing Papers of a Mathematical and Physical Character*, vol. 106, no. 738, pp. 416-428, 1924.

[12] M. Wright, "Nondestructive Testing Methods," *Encyclodpedia of Maritime and Offshore Engineering*, John Wiley & Sons, 2009.

[13] C. J. Hellier, *Handbook of Nondestructive Evaluation*. McGraw-Hill Education, 2013.

[14] W. Staszewski, B. C. Lee, L. Mallet, and F. Scarpa, "Structural health monitoring using scanning laser vibrometry: I. Lamb wave sensing," *Smart Materials and Structures*, vol. 13, no. 2, pp. 251-260, 2004.

[15] P. Castellini, M. Martarelli, and E. Tomasini, "Laser Doppler vibrometry: development of advanced solutions answering to technology's needs," *Mechanical Systems and Signal Processing*, vol. 20, no. 6, pp. 1265-1285, 2006.

[16] T. E. Michaels, J. E. Michaels, B. Mi, and M. Ruzzene, "Damage detection in plate structures using sparse ultrasonic transducer arrays and acoustic wavefield imaging," *AIP Conference Proceedings*, vol. 760, pp. 938-945, 2005.

[17] M. S. Harb and F.-G. Yuan, "Damage imaging using non-contact air-coupled transducer/laser Doppler vibrometer system," *Strucutural Health Monitoring*, vol. 15, no. 2, pp. 193-203, 2016.

[18] J. E. Michaels, "Ultrasonic wavefield imaging: Research tool or emerging NDE method?," *AIP Conference Proceedings*, vol. 1806, p. 020001, 2017.

[19] T.-Y. Yu and R. Haupt, "Damage inspection of fiber reinforced polymer-concrete systems using a distant acoustic-laser NDE technique," *Proceedings of SPIE*, vol. 7649, p. 76491J, 2010.

[20] S.-C. Hong, A.-D. Abetew, J.-R. Lee, and J.-B. Ihn, "Three dimensional evaluation of aluminum plates with wall-thinning by full-field pulse-echo laser ultrasound," *Optics and Lasers in Engineering*, vol. 99, pp. 58-65, 2017.

[21] I. Mueller and C.-P. Fritzen, "Inspection of piezoceramic transuducers used for structural health monitoring," *Materials*, vol. 10, no. 71, pp. 1-17, 2017.

[22] J. L. Blackshire, "Enhanced damage characterization using wavefield imaging methods," *AIP Conference Proceedings*, vol. 1806, p. 090008, 2017.

[23] The Collaboration for NDT Education: Iowa State University, *NDT Education Resource Center*, Accessed: May 5, 2018. url: https://www.nde-ed.org/EducationResources/CommunityCollege/Ultrasonics/EquipmentTrans/DataPres.htm

[24] P. Fromme and C. Rouge, "Directivity of guided ultrasonic wave scattering at notches and cracks," in *Journal of Physics: Conference Series*, vol. 269, p. 012018, 2011.

[25] J. C. P. McKeon and M. K. Hinders, "Lamb wave scattering from a through hole," *Journal of Sound and Vibration*, vol. 225, pp. 843-862, 1999.

[26] X. Chen, J. E. Michaels, and T. E. Michaels, "A methodology for estimating guided wave scattering patterns from sparse transducer array measurements," *IEEE Transactions on Ultrasonics, Ferroelectrics, and Frequency Control,* vol. 62, pp. 208-219, 2015.

[27] R. Bratton, S. Datta, and A. Shah, "Scattering of Lamb waves in a composite plate," *Review of Progress in Quantitative Nondestructive Evaluation*, vol. 10B, pp. 1507-1514, 1991.

[28] N. Toyama, J. Noda, and T. Okabe, "Quantitative damage detection in cross-ply laminates using Lamb wave method," *Composites Science and Technology,* vol. 63, no. 10, pp. 1473-1479, 2003.

[29] N. Toyama and J. Takarsubo, "Lamb wave method for quick inspection of impact-induced delamination in composite laminates," *Composites Science and Technology,* vol. 64, no. 9, pp. 1293-1300, 2004.

[30] W. M. Karunasena, A. H. Shah, and S. K. Datta, "Plane-strain-wave scattering by cracks in laminated composite plates," *Journal of Engineering Mechanics*, vol. 117, no. 8, pp. 1738-1754, 1991.

[31] M. R. Karim and T. Kundu, "Transient surface response of layered isotropic and anisotropic half-spaces with interface cracks: SH case," *International Journal of Fracture*, vol. 37, no. 4, pp. 245-262, 1988.

[32] N. Guo and P. Cawley, "The interaction of Lamb waves with delaminations in composite laminates," *Journal of the Acoustical Society of America,* vol. 94, no. 4, pp. 2240-2246, 1993.

[33] P. Guy, Y. Jayet, and L. Goujon, "Guided wave interaction with complex delaminations. Application to damage detection in composite structures," *Proceedings of SPIE,* vol. 5047, pp. 25-33, 2003.

[34] C. H. Wang and L. R. F. Rose, "Wave reflection and transmission in beams containing delamination and inhomogeneity," *Journal of Sound and Vibration*, vol. 264, no. 4, pp. 851-872, 2003.

[35] N. Hu, J. Li, Y. Cai, C. Yan, Y. Zhang, J. Qiu, K. Sakai, Y. Liu, X. Peng, and B. Yan, "Locating delamination in composite laminated beams using the A0 Lamb mode," *Mechanics of Advanced Materials and Structures*, vol. 19, no. 6, pp. 431-440, 2012.

[36] S. I. Ishak, G. R. Liu, S. P. Lim, and H. M. Shang, "Characterization of delamination in beams using flexural wave scattering analysis," *Journal of Vibration and Acoustics*, vol. 123, pp. 421-427, 2001.

[37] K.-T. Kang, H.-J. Chun, J.-H. Son, J.-A. Lee, J.-H. Byun, M.-K. Um, S.-K. Lee, and J.-W. Jang, "Quantitative accessibility of delamination in composite

using Lamb wave by experiments and FEA," *Advanced Composite Materials*, vol. 20, pp. 361-373, 2011.

[38] B. I. S. Murat, P. Khalili, and P. Fromme, "Scattering of guided waves at delaminations in composites plates," *Journal of the Acoustical Society of America*, vol. 139, pp. 3044-3052, 2016.

[39] K. S. Nadella, K. I. Salas, and C. E. S. Cesnik, "Characterization of guided-wave propagation in composite plates," *Proceedings of SPIE*, vol. 7650, p. 76502H, 2010.

[40] W. T. Thomson, "Transmission of elastic waves through a stratified solid medium," *Journal of Applied Physics*, vol. 21, pp. 89-93, 1950.

[41] N. A. Haskell, "Dispersion of surface waves on multilayer media," *Seismological Society of America*, vol. 43, pp. 17-34, 1953.

[42] A. H. Nayfeh, "The general problem of elastic wave propagation in multilayered anistropic media," *Journal of the Acoustical Society of America*, vol. 89, pp. 1521-1531, 1991.

[43] A. H. Nayfeh, *Wave Propagation in Layered Anisotropic Media with Application to Composites*. Elsevier Science, 1995.

[44] L. Knopoff, "A matrix method for elastic waves problems," *Seismological Society of America*, vol. 54, pp. 431-438, 1964.

[45] E. Kausel, "Wave propagation in anistropic layered media," *International Journal of Numerical Methods in Engineering*, vol. 23, pp. 1567-1578, 1986.

[46] S. I. Rokhlin and L. Wang, "Stable recursive alogorithm for elastic wave propagation in layered anistropic media: stiffness matrix method," *Journal of the Acoustical Society of America*, vol. 112, pp. 822-834, 2002.

[47] L. P. Solie and B. A. Auld, "Elastic waves in free anisotropic plates," *Journal of the Acoustical Society of America*, vol. 54, pp. 50-65, 1973.

[48] B. Tang and E. G. Henneke II, "Long wavelength approximation for Lamb wave characterization of composite laminates," *Research in Nondestructive Evaluation*, vol. 1, pp. 51-64, 1989.

[49] S. K. Datta, A. H. Shah, and W. Karunasena, "Ultrasonic waves and material and defect characterization in composite plates," *Mechanics of Composite Materials and Structures*, vol. 6, pp. 285-300, 1999.

[50] J. Zhao, J. Qiu, H. Ji, and N. Hu, "Four vectors of Lamb waves in composites: semianalysis and numerical simulation," *Journal of Intelligent Material Systems and Structures*, vol. 24, pp. 1985-1994, 2013.

[51] J. Zhao, H. Ji, and J. Qiu, "Modeling of Lamb waves in composites using new third-order plate theories," *Smart Materials and Structures*, vol. 23, p. 045017, 2014.

[52] S. Kim, B. Uprety, V. J. Matthews, and D. O. Adams, "Numerical simulation and experimental validation of Lamb wave propagation behavior in composite plates." *AIP Conference Proceedings*, vol. 1650, pp. 1178-1185, 2015.

[53] M. Nurhaniza, M. K. A. Arifin, A. Ali, F. Mustapha, and A. W. Noraini, "Finite element analysis of composites materials for aerospace applications," *IOP Conference Series: Materials Science and Engineering*, vol. 11, pp. 1-7, 2010.

[54] E. Sabau, A. Popescu, and C. Vilau, "Mechanical behavior of composite materials using the finite element analysis," *MATEC Web of Conferences*, vol. 137, p. 08006, 2017.

[55] B. Pavlakovic, M. Lowe, D. Alleyne, and P. Cawley, "Disperse: a general purpose program for creating dispersion curvers," *Review of Progress in Quantitative Nondestructive Evaluation*, vol. 16, pp. 185-192, 1997.

[56] C. A. C. Leckey, K. R. Wheeler, V. N. Hafiychuk, H. Hafiychuk, and D. A. Timuçin, "Simulation of guided-wave ultrasound propagation in composite laminates: benchmark comparisons of numerical codes and experiment," *Ultrasonics*, vol. 84, pp. 187-200, 2017.

[57] R. M. Sanderson and S. D. Smith, "The application of finite element modelling to guided wave testing systems," *AIP Conference Proceedings*, vol. 657, pp. 256-263, 2003.

[58] Y. X. Zhang and C. H. Yang, "Recent developments in finite element analysis for laminated composite plates," *Composite Structures*, vol. 88, pp. 147-157, 2009.

[59] R. Weber, S. M. H. Hosseini, and U. Gabbert, "Numerical simulation of the guided Lamb wave propagation in particle reinforced composites," *Composite Structures*, vol. 94, pp. 3064-3071, 2012.

[60] Y. Shen and C. E. S. Cesnik, "Hybrid local FEM/global LISA modeling of damped guided wave propagation in complex composite structures," *Smart Materials and Structures*, vol. 25, p. 095021, 2016.

[61] D. Samaratunga, R. Jha, and S. Gopalakrishnan, "Wavelet spectral finite element for modeling guided wave propagation and damage detection in stiffened composite panels," *Structural Health Monitoring*, vol. 15, pp. 317-334, 2016.

[62] M. Kersemans, A. Martens, J. Degrieck, K. Van Den Abeele, S. Delrue, L. Pyl, F. Zastavnik, H. Sol, and W. V. Paepegem, "The ultrasonic polar scan for composite characterization and damage assessment: past, present and future," *Applied Science*, vol. 6, pp. 1-15, 2016.

[63] M. S. Harb and F. G. Yuan, "Lamb wave dispersion and anistropy profiling of composite plates via non-contact air-coupled and laser ultrasound," *AIP Conference Proceedings*, vol. 1650, pp. 1229-1238, 2015.

[64] A. Raghavan and C. E. S. Cesnik, "Review of guided-wave structural health monitoring," *The Shock and Vibration Digest*, vol. 39, no. 2, pp. 91-114, 2007.

[65] M. Mitra and S. Gopalakrishnan, "Guided wave based strucutural health monitoring: A review," *Smart Materials and Structures*, vol. 25, no. 5, p. 053001, 2016.

[66] K. Peters, "Fiber-optic sensor principles," *Encyclodpedia of Structural Health Monitoring*, John Wiley & Sons, 2009.

[67] K. Peters, "Intensity-, interferometric-, and scattering-based optical-fiber sensors," *Encyclodpedia of Structural Health Monitoring*, John Wiley & Sons, 2009.

[68] V. Giurgiutiu, "Structural health monitoring (SHM) of aerospace composites," *Polymer Composites in the Aerospace Industry*, P.E. Irving and C. Soutis, Woodhead Publishing, 2015, pp. 449-507.

[69] S. Gupta, A. Ray, and E. Keller, "Symbolic time series analysis of ultrasonic data for early detction of fatigue damage," *Mechanical Systems and Signal Processing*, vol. 21, pp. 866-884, 2007.

[70] B. Mi, J. E. Michaels, and T. E. Michaels, "An ultrasonic method for dynamic monitoring of fatigue crack initiation and growth," *Acoustical Society of America*, vol. 119, pp. 74-85, 2006.

[71] J. E. Michaels, T. E. Michaels, and B. Mi, "An ultrasonic angle beam method for in situ sizing of fastener hole cracks," *Journal of Nondestructive Evaluation*, vol. 25, pp. 2-15, 2006.

[72] S. Kenderian, T. P. Berndt, R. E. Green, and B. B. Djordjevic, "Ultrasonic monitoring of dislocations during fatique of pearlitic rail steel," *Material Science and Engineering*, vol. 348, pp. 90-99, 2003.

[73] J. E. Michaels and T. E. Michaels, "Detection of structural damage from the local temporal coherence of diffuse ultrasonic signals," *IEEE Transactions on Ultrasonics, Ferroelectrics, and Frequency Control,* vol. 52, pp. 1769-1782, 2005.

[74] Y. Lu and J. E. Michaels, "A methodology for structural health monitoring with diffuse ultrasonic waves in the presence of temperature variations," *Ultrasonics,* vol. 43, pp. 717-731, 2005.

[75] J. B. Harley and J. M. F. Moura, "Scale transform signal processing for optimal ultrasonic temperature compensation," *IEEE Transactions on Ultrasonics, Ferroelectrics, and Frequency Control,* vol. 59, pp. 2226-2236, 2012.

[76] Z. Lu, S. J. Lee, J. E. Michaels, and T. E. Michaels, "On the optimization of temperature compensation for guided wave structural health monitoring," *AIP Conference Proceedings,* vol. 1211, pp. 1860-1867, 2010.

[77] P. D. Wilcox, "Omni-directional guided wave transducer arrays for the rapid inspection of large areas of plate structures," *IEEE Transactions on Ultrasonics, Ferroelectrics, and Frequency Control,* vol. 50, pp. 699-709, 2003.

[78] P. Fromme, P. D. Wilcox, M. J. S. Lowe, and P. Cawley, "On the development and testing of a guided ultrasonic wave array for structural integrity monitoring," *IEEE Transactions on Ultrasonics, Ferroelectrics, and Frequency Control,* vol. 53, pp. 777-785, 2006.

[79] L. Yu and Z. Tian, "Guided wave phased array beamforming and imaging in composite plates," *Ultrasonics,* vol. 68, pp. 43-53, 2016.

[80] A. Leleux, P. Micheau, and M. Castaings, "Long range detection of defects in composite plates using Lamb waves generated and detected by ultrasonic phased array probes," *Journal of Nondestructive Evaluation,* vol. 32, pp. 200-214, 2013.

[81] F. Yan and J. L. Rose, "Guided wave phased array beam steering in composite plates," *Health Monitoring of Structural and Biological Systems,* vol. 6532, p. 65320G, 2007.

[82] C. H. Wang, J. T. Rose, and F.-K. Chang, "A synthetic time-reversal imaging method for structural health monitoring," *Smart Materials and Structures,* vol. 13, pp. 415-423, 2004.

[83] J. S. Hall and J. E. Michaels, "Minimum variance ultrasonic imaging applied to an in situ sparse guided wave array," *IEEE Transactions on Ultrasonics, Ferroelectrics, and Frequency Control,* vol. 57, pp. 2311-2323, 2010.

[84] J. S. Hall, P. McKeon, L. Satyanarayan, J. E. Michaels, N. F. Declercq, and Y. H. Berthelot, "Minimum variance guided wave imaging in a quasi-isotropic composite plate," *Smart Materials and Structures,* vol. 20, p. 025013, 2011.

[85] https://dragonplate.com, accessed September 30, 2017

[86] J. E. Michaels, S. J. Lee, A. J. Croxford, and P. D. Wilcox, "Chirp excitation of ultrasonic guided waves," *Ultrasonics,* vol. 53, pp. 265-270, 2013.

[87] http://a.co/d/94wqHmx, accessed September 27, 2018.

[88] T. N. H. T. Tran, K.C. T. Nguyen, M. D. Sacchi, and L. H. Le, "Imaging ultrasonic dispersive guided wave energy in long bones using linear Radon transform," *Ultrasound in Medicine & Biology,* vol. 40, pp. 2715-2727, 2014.

[89] C. H. Chapman, "Generalized Radon transforms and slant stacks," *Geophysical Journal of the Royal Astronomical Society,* vol. 66, pp. 445-453, 1981.

[90] H. H. Barrett, "III The Radon transform and its applications," *Progress in Optics,* vol. 21, pp. 217-286, 1984.

[91] J. Radon, "On the determination of functions from their integral values along certain manifolds," *IEEE Transactions on Medical Imaging,* vol. 5, pp. 170-176, 1986.

[92] P. Toft, *The Radon Transform: Theory and Implementation*, Ph.D. Thesis, Department of Mathematical Modeling, Technical University of Denmark, 1996.

[93] O. Putkis, R. P. Dalton, and A. J. Croxford, "The anisotropic propagation of ultrasonic guided waves in composite materials and implications for practical applications," *Ultrasonics,* vol. 65, pp. 390-399, 2016.

[94] https://www.tencatecomposites.com/, accessed October 17, 2017.

[95] A. J. Dawson, J. E. Michaels, and T. E. Michaels, "Isolation of ultrasonic scattering by wavefield baseline subtraction," *Mechanical Systems and Signal Processing*, vol. 70–71, pp. 891-903, 2016.

[96] Z. Tian and L. Yu, "Lamb wave frequency-wavenumber analysis and decomposition," *Journal of Intelligent Material Systems and Structures*, vol. 25, no. 9, pp. 1107-1123, 2014.

[97] E. B. Flynn, S. Y. Chong, G. J. Jarmer, and J.-R. Lee, "Structural imaging through local wavenumber estimation of guided waves," *NDT & E International*, vol. 59, pp. 1-10, 2013.

[98] M. Ruzzene, “Frequency-wavenumber domain filtering for improved damage visualization,” *Smart Materials and Structures*, vol. 16, no. 6, pp. 2116-2129, 2007.

[99] MatLab™, *solve*, Accessed: April 17, 2017. url: https://www.mathworks.com/help/symbolic/solve.html.

[100] W. B. Williams, J. E. Michaels, and T. E. Michaels, "Characterization of propagation and scattering via wavefield imaging for improved in situ imaging of damage in composites," *Proceedings of SPIE*, vol. 9805, p. 980502, 2016.

[101] J. S. Hall, P. Fromme, and J. E. Michaels, "Guided wave damage characterization via minimum variance imaging with a distributed array of ultrasonic sensors," *Journal of Nondestructive Evaluation*, vol. 33, pp. 299-308, 2014.

[102] J. E. Michaels, A. J. Croxford, and P. D. Wilcox, "Imaging algorithms for locating damage via in situ ultrasonic sensors," *Proceedings of the IEEE Sensors Applications Symposium*, pp. 63-67, 2008.

[103] J. S. Hall and J. E. Michaels, “Analysis of distributed sparse array configurations for guided wave imaging applications,” *AIP Conference Proceedings*, vol. 1335, pp. 859-866, 2011.